ANALYSIS OF STRAIN HETEROGENEITY IN ADDITIVE MANUFACTURED TI6AL4V CUBIC POROUS STRUCTURES BY EXPERIMENTAL TESTING AND FINITE ELEMENT METHOD

by

Mehrdad PAKNEZHAD

THESIS PRESENTED TO ÉCOLE DE TECHNOLOGIE SUPÉRIEURE
IN PARTIAL FULFILLMENT FOR THE DEGREE OF
DOCTOR OF PHILOSOPHY
Ph.D.

MONTRÉAL, 25 JANUARY 2024

ÉCOLE DE TECHNOLOGIE SUPÉRIEURE
UNIVERSITÉ DU QUÉBEC

BOARD OF EXAMINERS

THIS THESIS HAS BEEN EVALUATED

BY THE FOLLOWING BOARD OF EXAMINERS

Mr. Philippe Bocher, Thesis Supervisor
Department of Mechanical Engineering, École de technologie supérieure

Ms. Natalia Nuño, Thesis Co-supervisor
Department of Systems Engineering, École de technologie supérieure

Mr. Alejandro Yanez Santana, Thesis Co-supervisor
Department of Mechanical Engineering, University of Las Palmas de Gran Canaria

Ms. Claudiane Ouellet-Plamondon, President of the jury
Department of Civil Engineering, École de technologie supérieure

Mr. Henri Champliaud, Member of the jury
Department of Mechanical Engineering, École de technologie supérieure

Mr. Lyès Hacini and Mr. Samir Chentouf, External Jury Members

THIS THESIS WAS PRENSENTED AND DEFENDED

IN THE PRESENCE OF A BOARD OF EXAMINERS AND PUBLIC

ON 25 JANUARY 2024

AT ÉCOLE DE TECHNOLOGIE SUPÉRIEURE

ACKNOWLEDGMENT

Words can not express my gratitude to my supervisors, Prof. Philippe Bocher and Prof. Natalia Nuño, who provided me with considerate guidance and thoughtful feedbacks throughout this research. I also could not have undertaken this journey without my co-supervisor, prof. Alejandro Yanez Santana, who generously provided knowledge, expertise, and helped in applying for international scholarship program with ÉTS University. In addition, this endeavor would not have been possible without the generous support of prof. Henri Champliaud for providing advices regarding FEM simulations.

I would like to extend my sincere thanks to Nicolas Vanderesse, research assistant at ÉTS, for his invaluable guidance with experimental testings and image analysis procedure.

I am also grateful to all LOPFA group members, especially Mohsen Mokhtabad-Amrei and Ahad Shafiee, who impacted and inspired me. I would like to recognize all ÉTS librarians, especially Prasun Lala, for offering educational workshops and moral support.

Thanks should also go to LAMSI group Dr. Vladimir Brailovski for manufacturing titanium porous structures.

Lastly, I would be remiss in not mentioning my family, especially my parents, and my friends. Their belief in me has kept my motivation high during this process.

Analyse de l’hétérogénéité des déformations dans des structures poreux cubes Ti6Al4V fabriquées additifs par essais expérimentaux et simulation par éléments finis

Mehrdad PAKNEZHAD

RÉSUMÉ

Le comportement mécanique, en particulier l'hétérogénéité des contraintes, des biomatériaux poreux en titane (Ti-6Al-4V) a été étudié en utilisant la technique de corrélation d'images numériques 2D (2D DIC). Trois échantillons cubiques avec une porosité de 75 % ont été fabriqués à l'aide de la fusion laser sélective (SLM), qui est basée sur la technique de laser powder bed fusion (LPBF). Ils ont été testés dans des conditions de chargement en compression quasi-statique jusqu'à un déplacement de 1 mm de la traverse de la machine. Parallèlement à la méthode 2D DIC, un extensomètre de contact a été utilisé pour mesurer le déplacement avec plus de précision. Les graphiques contrainte-déformation apparents pour trois échantillons et trois méthodes ont été obtenus, et il a été constaté que l'échantillon 2 a le module d'élasticité apparent le plus bas tandis que la région linéaire la plus longue, contrairement à l'échantillon 1. Les cartes de déformation et les histogrammes obtenus par OpenDIC et ImageJ a démontré que la répartition des contraintes n'est pas la même non seulement entre les trois faces de chaque échantillon, mais également sur une face spécifique à travers trois échantillons. Ce fait a été analysé au microscope confocal à balayage laser pour trois faces de l'échantillon 3 (avant et après essai). Plus important encore, une analyse avancée des graphiques de déformation pour chaque étage englobant uniquement les entretoises verticales a permis de conclure que bien que chaque étage n'ait pas le même comportement de déformation et la même valeur de déformation maximale parmi trois échantillons, l'étage 2 a la déformation localisée la plus élevée. Enfin, la déformation tardive d'un étage peut être un signe potentiel d'accumulation de contraintes sévères dans quelques entretoises de cet étage, c'est-à-dire l'étage 2.

Mots-clés : fabrication additive, structure poreuse cubique, hétérogénéité des déformations, Ti6Al4V, méthode des éléments finis, essai de compression, corrélation d'images numériques en 2D, module d'élasticité

Analysis of strain heterogeneity in additive manufactured Ti6Al4V cubic porous structures by experimental testing and finite element method

Mehrdad PAKNEZHAD

ABSTRACT

The mechanical behavior, especially strain heterogeneity, of porous titanium biomaterials (Ti-6Al-4V) was studied by using 2D digital image correlation technique (2D DIC). Three cubic samples with 75% porosity were fabricated using selective laser melting (SLM), which is based on laser powder bed fusion (LPBF) technique. They were tested under quasi-static compressive loading condition up to 1 mm displacement of machine crosshead. Along with 2D DIC method, contact extensometer was used to measure displacement more accurately. The apparent stress-strain graphs for three samples and three methods were obtained, and it was found that sample 2 has the lowest apparent elastic modulus while the longest linear region, which is in contrast for sample 1. The strain maps and histograms obtained by OpenDIC and ImageJ software demonstrated that strain distribution is not the same not only among three faces of each sample, but also in one specific face through three samples. This fact was analyzed by laser scanning confocal microscope for three faces of sample 3 (before and after test). Most importantly, advanced analysis of strain graphs for each floor encompassing only vertical struts helped to conclude that although each floor does not have the same strain behavior and peak strain value among three samples, floor 2 has the highest localized strain. Lastly, late deformation of one floor can be a potential sign of severe strain accumulation in few struts of that floor i.e. floor 2.

Keywords: additive manufacturing, cubic porous structure, strain heterogeneity, Ti6Al4V, finite element method, compression test, 2D digital image correlation, apparent elastic modulus

TABLE OF CONTENTS

Page

LIST OF TABLES

LIST OF FIGURES

LIST OF ABREVIATIONS AND SYMBOLS

Symbols:

$E_{ap,comp}$	Apparent compressive elastic modulus
MPa	Mega pascal
GPa	Giga pascal
P	Porosity of the structure
$p_{material}$	Density of the bulk material
$p_{structure}$ (p_s)	Density of the lattice structure
σ_{pl}	Plastic collapse strength
E	Elastic modulus
$\emptyset_{rand}$	Random diameter
R	Radius
$\bar{\rho}$	Effective relative density
VER	Vertical build orientation
DIA	Diagonal build orientation

HOR	Horizontal build orientation
VER-45°	Unit cell rotation of 45°
VER-90°	Unit cell rotation of 90°
σ_y	Yield stress
σ_{max}	Maximum or ultimate stress
s	Second
KN	Kilo newton
mm/min	Millimeter per minute
Ti	Titanium
Al	Aluminum
V	Vanadium
$\sigma_{O2}/2$	Stress in inflection point of elastic region
σ_{O2}	Yield stress
σ_{failure}	Stress when the structure fails
HF	Hydrogen fluoride

HNO3	Hydrogen nitrate
H2O	Water
Y’	First derivative equation
Y’’	Second derivative equation
epsxx.tif	Strain field file in X direction
epsxy.tif	Strain field file in XY plane
epsyy.tif	Strain field file in Y direction
u.tif	Displacement field file in X direction
v.tif	Displacement field file in Y direction
zncc.tif	Quality measurement index
StdDev	Standard deviation

Acronymes:

AM	Additive Manufacturing
CAD	Computer Aided Design
SLM	Selective Laser Melting

SLS	Selective Laser Sintering
EBM	Electron Beam Melting
DMLS	Direct Metal Laser Sintering
2D	2 Dimension
3D	3 Dimension
FGPS	Functionally Graded Porous Structure
F2cc,z	Face-centered cubic structure reinforced in the Z direction
BCCZ	Body-centered cubic structure reinforced in the Z direction
2D-DIC	2 Dimension-Digital Image Correlation
SEM	Scanning Electron Microscope
LSCM	Laser Scanning Confocal Microscope
AISI	American Iron and Steel Institute
SS	Stainless Steel
CP	Commercially Pure
APDL	Ansys Parametric Design Language

CNC	Computer Numerical Control
BMP	Bitmap Image File
LOPFA	Laboratoire d'Optimisation des Procédés de Fabrication Avancés
ÉTS	École de Technologie Supérieure
ISO	International Organization for Standardization

INTRODUCTION

The mechanical properties of titanium porous structures, especially elastic properties, have become a controversial issue in recent years. These structures are used as hard tissue replacements in the body (bones), and as a bone, enduring the body weight without having plastic deformation is really important. On the other hand, the uniform deformation of the struts through these structures is of utmost importance. In a way that the more uniform the whole struts deform, the longer they can tolerate the load condition without failing. This is the reason why this study is focused on analyzing the elastic behavior and strain heterogeneity of these structures through experimental tests and numerical models.

In order to investigate the elastic behavior and the strain heterogeneity of these porous structures, a comprehensive study on the previous studies is performed. The chapter one reviews the literature existing on this subject. Then, the chapter two explains the context of this research.

The aforementioned purpose is achieved by manufacturing three cubic porous structures, performing experimental testing on them, and modeling them by APDL, which are described in chapter three. Three cubic samples with 75% porosity were fabricated using selective laser melting (SLM), which is based on laser powder bed fusion (LPBF) technique. They were tested under quasi-static compressive loading condition up to 1 mm displacement of machine crosshead. Along with 2D DIC method, contact extensometer was used to measure displacement more accurately.

In chapter four, after obtaining the apparent stress-strain graphs for three samples and three methods, it is found that sample 2 has the lowest apparent elastic modulus while the longest linear region, which is in contrast for sample 1. The strain maps and histograms obtained by OpenDIC and ImageJ software demonstrated that strain distribution is not the same not only among three faces of each.

To shed the light on the experimental results, a complementary study was performed by APDL in chapter five to simulate the mechanical properties of these structures and compare the results with those of experiments.

This manuscript ends with a conclusion followed by recommendations and appendixes

CHAPTER 1

LITERATURE REVIEW

1.1. Introduction

In this chapter, a brief review of designing and manufacturing process of porous structures is presented. Different methods of additive manufacturing (3D printing), parameters affecting the design of porous structures and the special mechanical tests are introduced. Additionally, a short review of the modeling methods and types of mesostructures (the structure in mesoscale, $10^{-1} - 10^{0} mm$) are presented to understand what characteristics each cellular structure has.

The mechanical property of porous structure is a controversial issue. For using this kind of structure in the biomedical as a joint replacement for example, it is essential to satisfy specific demands. To do that, different porous materials with various topologies (Figure 1-1), materials, fabrication methods and other characteristics are used (Vanderesse, Richter, Nuno, et al. 2018). Optimization of each parameter according to the specific condition under which this structure is going to be utilized is of utmost importance.

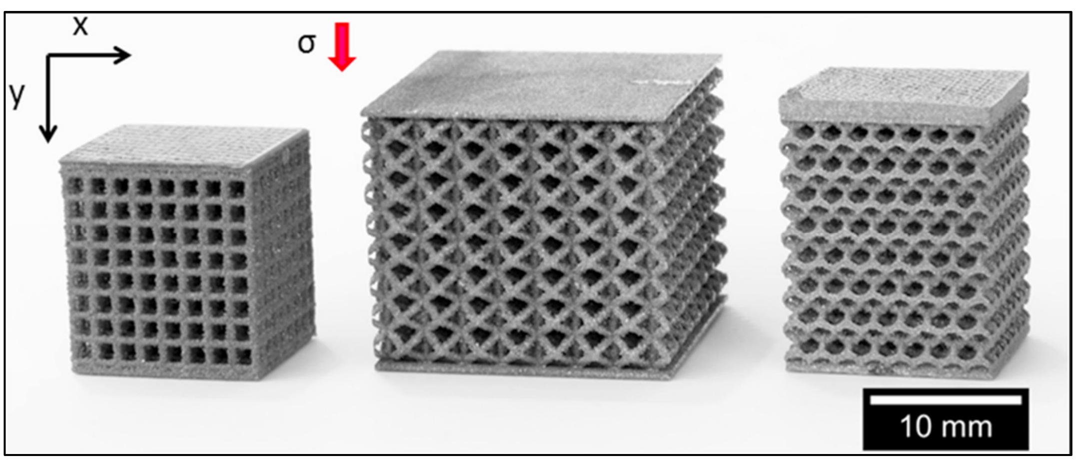

Figure 1-1 Specimens with cubic, BCCZ, and diamond unit cells, from left to right
Taken from Vanderesse et al. (2018)

Clinical applications of porous structures

Porous structures are used as different organs (Mertens, Löwenheim, and Hoffmann 2013; Jardini et al. 2014). The world's first additively manufactured lower jaw was implanted in a 83-year-old patient by Dr. Jules Poukens in 2012 (Wang et al. 2016) (Figure 1-2). The lattice implant was slightly heavier than a natural jaw and could provid strong attachment of muscles and sufficient space for nerves. Mertens et al. successfully reconstructed a defect using AM manufactured titanium implants which provided both mid-facial support and a graft fixture (midface defect in Figure 1-2). Jardini et al. in Brazil designed and AM fabricated a customized implant for the surgical reconstruction of a large cranial defect.

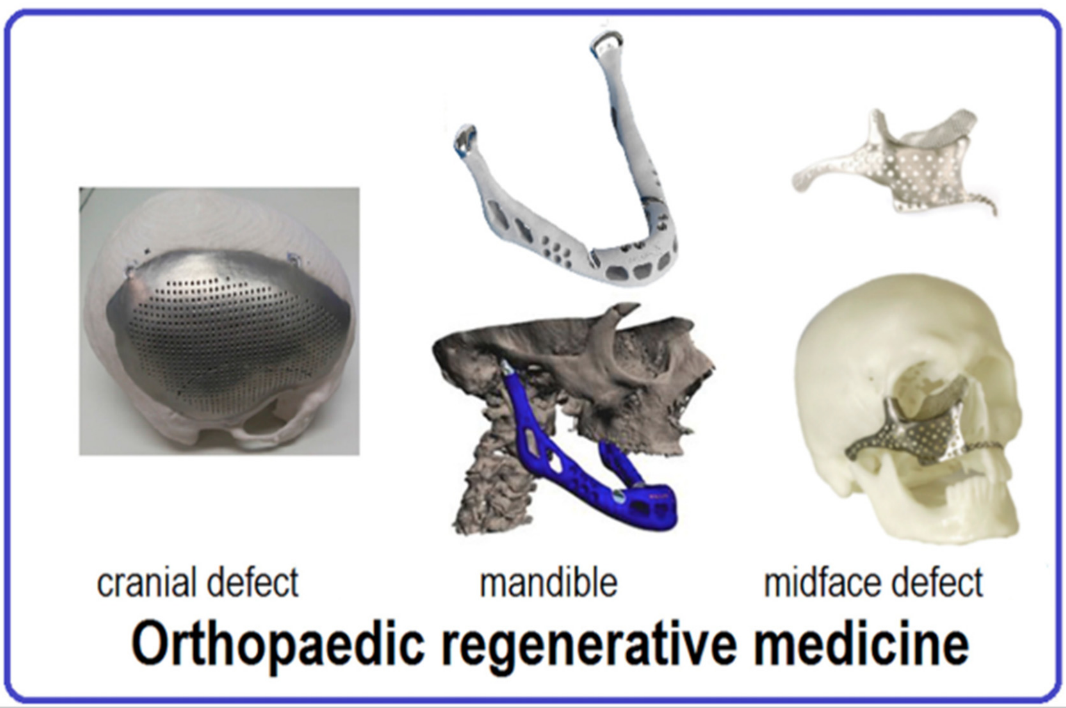

Figure 1-2 Latest orthopedic regenerative medicine examples
Taken from Wang et al. (2016)

Advantages of porous structure

Nowadays, the use of porous scaffolds has become very important in a wide range of sectors, including the electronics, motor vehicles, industrial business and especially, medicine (Wohlers 2014). This is because of having some attractive characteristics that the uniform bulk materials do not possess such as high stiffness (a measure of the material resistance offering by an elastic body to deformation) to weight ratio, high thermal conductivity and high energy absorption (Köhnen et al. 2018; Xiao and Song 2018). When it comes to biomedical, they are used as bone-mimicking biomaterials (Figure 1-3). Joint replacement surgery and bone grafting are two vital examples of their usage. These structures have mechanical properties close to those of bones and their shapes enable better bone ingrowth and implant fixation. One astonishing aspect of these scaffolds is that their stiffness and porosity can be tailored according to the shape and size of the unit cells (Cuadrado et al. 2017).

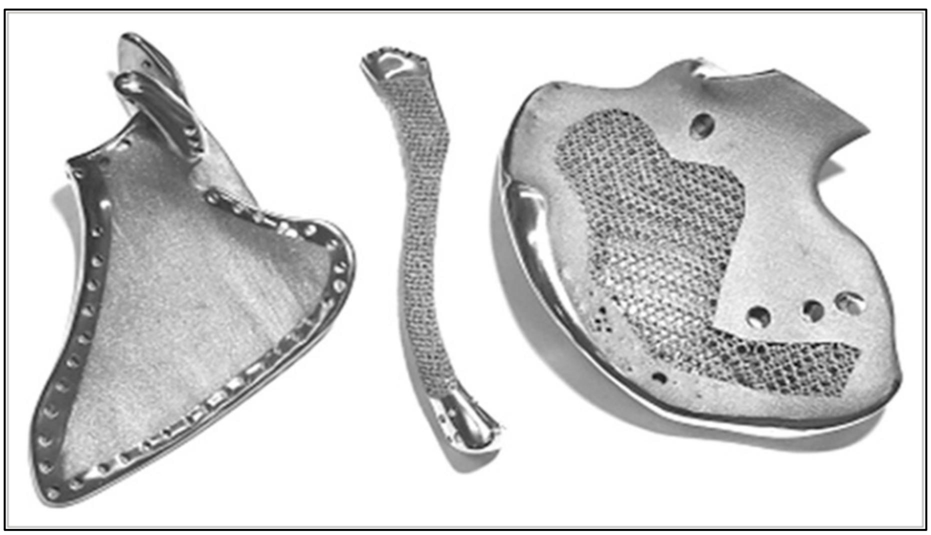

Figure 1-3 Examples of Ti–6Al–4V implant made in Shenyang National Laboratory for Materials Science, Institute of Metal Research (IMR, China)
Taken from Zhang et al. (2018)

Definition of additive manufacturing

Additive manufacturing (AM), rapid prototyping or solid freeform fabrication is a layer-by-layer process, which is based on melting a powder or wire feedstock with a high-energy source (Figure 1-4). According to the computer aided design (CAD) file, a heating beam sweeps a layer of metallic powder and after making it melt or sinter at selected positions, a new layer of powder is added and this process continues until the part is completed (Vanderesse et al. 2016; Juarez 2017; Alexander et al. 2021).

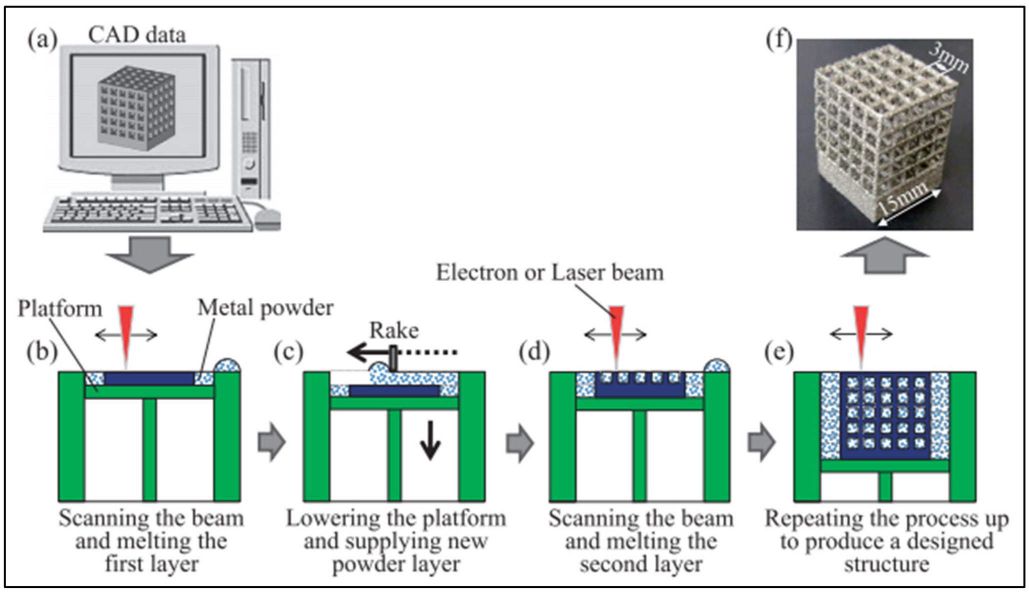

Figure 1-4 Schematic diagram illustrating the powder bed fusion method used in fabricating a metallic product with a lattice structure
Taken from Nakano et al. (2015)

Additive manufacturing techniques are increasingly developed because they provide us with many advantages like having full control over material, internal architecture and consequently mechanical and biological responses of scaffolds (Kadkhodapour et al. 2015; Wauthle, Vrancken, et al. 2015; Bayley and Kopac 2018; Buj-Corral, Tejo-Otero, and Fenollosa-Artés 2020). For instance, the fabrication of lightweight porous structures with locally defined mechanical properties is possible with high repeatability thanks to this method (Bourell 2016; Klahn, Leutenecker, and Meboldt 2015). More importantly, this method is able to fabricate complex geometries like gyroid and rhombic dodecahedron lattice structures (Figure 1-5). This is not the case as far as conventional production methods are concerned in which the final part is produced from a stock material after applying some additional processing (Parthasarathy, Starly, and Raman 2011). The main disadvantage of AM technique is its high cost compared with other production methods such as space holder technique. However, the cost is expected to be reduced by future developments (Zargarian et al. 2016).

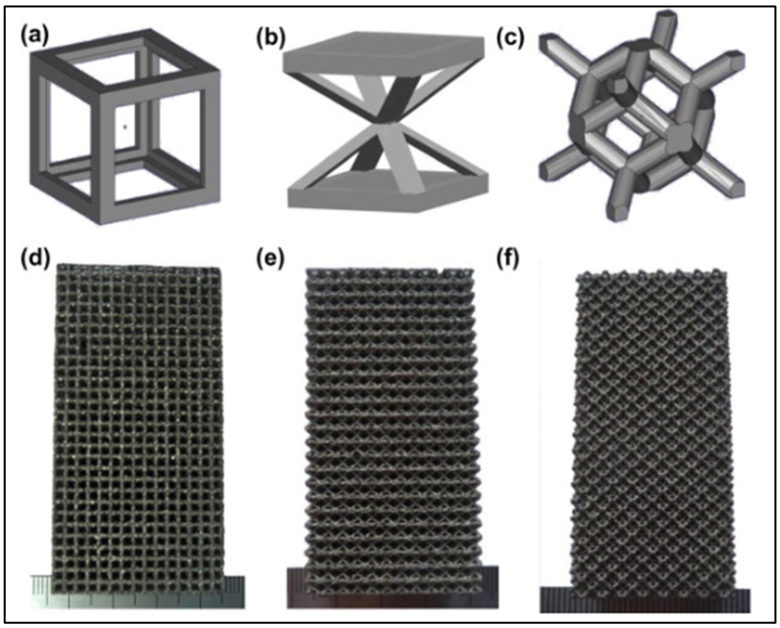

Figure 1-5 (a–c) Cubic, G7 and rhombic dodecahedron element in the Materialise software and (d–f) the corresponding Ti–6Al–4V prototype blocks fabricated by the EBM method
Taken from Li et al. (2014)

The design of lattice structures includes mainly the choice of the AM technology, the material, the lattice geometry, the relative density of the structure according to the bulk material and the maximal defect density of every strut and node of this structure (Köhnen et al. 2018).

1.2. Methods for fabrication of porous structures

Different methods are available to manufacture open cellular structures but among all, additive manufacturing technique is the one enabling the fabrication of porous structures with predictable unit cells. It means that the expected shape of the unit cell can be fulfilled with the sample manufacturing with this method (Campoli et al. 2013).

Additive manufacturing technique is divided into some methods such as selective laser melting (SLM), selective laser sintering (SLS), electron beam melting (EBM) and direct metal laser sintering (DMLS).

Lattice structures are mostly fabricated by SLM or EBM method (Nguyen et al. 2022). The base of both techniques is the same, melting a metal powder to build a structure layer by layer, but the key difference between these two is the heat source. The heat source of the SLM is a laser beam but that of the latter is an electron beam (Campoli et al. 2013; Tan et al. 2017; Zhao et al. 2016). Overall, there is both pros and cons for each technique. SLM makes specimens with higher precision because of smaller laser spot size resulting in having lower fabrication speed and taking more time for the specimen to be finished. On the other hand, the cooling rates in EBM are much lower than those in SLM (the powder bed in EBM is maintained at an elevated temperature, around 675 °C, throughout part fabrication). This slow cooling rate results in having structures with higher ductility and lower yield strength and fatigue limit (Tan et al. 2017; Gong et al. 2015; Murr et al. 2012; Feng et al. 2018; Balachandramurthi et al. 2018). Additionally, there is less residual stress (the internal stress locked into a material) in the part produced by EBM as the powder is preheated to 600-700°C which is not the case for SLM and as a consequence, stress relief process such as thermal treatment must be done after the process (Campoli et al. 2013; Zargarian et al. 2016). According to Figure 1-6, an electron beam is scanned based on 2D slice data created from 3D CAD data of the final form, and by repeating the process of selectively melting and solidifying one layer of metal powder at a time, multiple layers are stacked up to produce a three-dimensional structure. Moreover, to compare the two techniques in detail, SLM and EBM, Table 1-1 is presented.

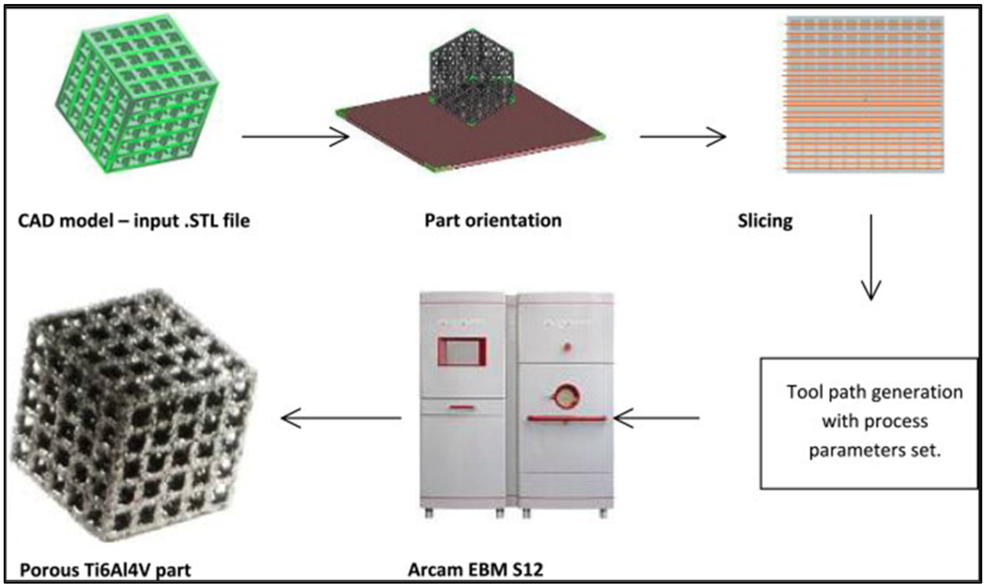

Figure 1-6 Steps taken in producing EBM part
Taken from Parthasarathy et al. (2011)

Table 1-1 Features of SLM and EBM in comparison
Taken from Bhavar et al. (2014)

	SLM	EBM
Powder sources	One or more fiber lasers of 200–1000W	High power Electron beam of 3000W
Build chamber environment	Argon or Nitrogen	Vacuum/He bleed
Method of powder preheating	Platform heating	Preheat scanning
Powder preheating temperature (°C)	100–200	700–900
Maximum available build volume (mm)	500×350×300	350×380 (diameter×length)
Maximum build rate (cm^3/h)	20–35	80
Layer Thickness (mm)	0.020–0.100	0.050–0.200
Melt pool size (mm)	0.1–0.5	0.2–1.2
Surface finish (Ra)	4–11	25–35
Geometric tolerance (mm)	±0.05–0.1	±0.2
Minimum feature size	40–200	100

Irregularities

It is interesting to know that some defects of specimens or irregularities are caused by not choosing the manufacturing parameters properly. Wrong selections of two factors of SLM technique, laser power and laser travel speed, can affect the fusing of materials and consequently the mechanical properties (Campoli et al. 2013). Additionally, the surface roughness of struts is usually more in porous structures produced by EBM. That is why some authors suggest using SLM technique as the struts have smoother surface ending with slightly better mechanical properties (Cuadrado et al. 2017). The influence of surface roughness on mechanical properties of structures is due to the fact when the surface is rough, there is many sharp-angled particles on the surface and as a result, the stress concentrates on these spots and raises the potential of crack initiation (Zhao et al. 2018b).

1.3. Porous structure modeling

The first step for fabricating a specimen is designing a CAD model. Then, the specimen is fabricated and tested under specific load condition. After observing the deformation behavior of the specimen and collecting data, it is possible to recognize if this behavior is normal or there is a problem. By understanding the problem, there is an opportunity to improve it thanks to mimicking the situation with simulating the test. By knowing the material properties of the part and boundary conditions when testing, it is possible to simulate the behavior of the specimen by commercial software (ANSYS or ABAQUS). This helps to analyze the part’s deformation behavior precisely and comprehensively. Therefore, it is of utmost importance to create a valid model since it can be cost-effective.

1.3.1. Modeling methods

There are numerical and analytical models by which open cellular structures can be created.

1.3.1.1. Numerical model

For creating a model through numerical method, three steps must be taken.

1) Preprocessor

Through this step the dimension of the whole structure, element type of the lines, material properties, section of the struts, creating every element of the structure like key points, lines and areas, meshing the elements and even the boundary condition such as applying constraints and loads on nodes or areas are chosen.

2) Solution

The type of analysis is determined (e.g. static, modal, harmonic…)

3) Post-processor

The function of this step is to show the mechanical behavior of the structure subjected to loads or displacements and plot stress, strain and deformation of the structure.

Some researchers did modeling and simulation of lattice structures with numerical models (Parthasarathy, Starly, and Raman 2011; Gonzalez and Nuno 2016). In these studies, the numerical simulation was performed through ANSYS software with a finite element analysis model to simulate the deformation behavior of the SLM fabricated titanium lattice samples.

The modeling of scaffolds in other studies was performed by using ABAQUS. Based on (Campoli et al. 2013; Kadkhodapour et al. 2015; Cao et al. 2018), the model is created with ABAQUS software to predict the mechanical properties of structures and compare with those of experimental tests.

1.3.1.2. Analytical model

There is another method for analyzing porous structures, analytical approach, which can be created by resolving a set of equations using Matlab or Python software. This approach is used in various studies. Based on (Campoli et al. 2013), the limitations of analytical models in prediction of the mechanical properties of porous metallic biomaterials was explored. Considering these limitations, some studies showed that mechanical properties of the porous biomaterials manufactured by additive manufacturing techniques cannot be predicted by analytical models or they often can only predict the mechanical properties of scaffolds with slender struts (Parthasarathy et al. 2010).

In another study, analytical models are used to determine the initial stiffness and plastic collapse of the BCC unit cells under compressive loads (Smith, Guan, and Cantwell 2013; Ushijima et al. 2011). Additionally, Van Hooreweder and Kruth in 2017 calculated the local normal stress of struts in diamond unit cells by using this method. There are usually some differences between the results of numerical models and analytical ones such as deviations in the value of stiffness. This difference in the value of young modulus is increased with increase in the strut radius (Campoli et al. 2013).

1.3.2. Modeling parameters

The important factors considered through modeling and simulation are pore size, porosity, distribution uniformity and some properties of struts as their thickness, length, inclination, irregularity along their length and cross-section, material properties, layer thickness, type of element definition and the size of the model.

1.3.2.1. Number of unit cells

According to the previous studies, it is proven that the number of unit cells in each direction (*X, Y and Z)* plays a vital role in estimation of the mechanical properties of lattice structures. According to (Ahmadi et al. 2014a), when this factor is enhanced from 5 to 20 in each direction, the stiffness is increased and it results in gaining approximately the same amounts of elastic modulus and poisson's ratio in numerical and analytical methods. It is mentioned also that having 14 unit-cells in each direction is enough for mechanical properties prediction. In (Quevedo González and Nuño 2016), the effect of this factor on the apparent elastic modulus ($E_{ap,comp}$) was analyzed. According to this study, if the number of unit cells is more than 8 in each direction, there will be no significant change in $E_{ap,comp}$. In contrast, based on (Kadkhodapour et al. 2015), it is possible to predict the key mechanical properties of scaffolds accurately just by modeling the constitutive unit cells (small number of unit cells) instead of making a model with large number of unit cells. Also, the change in the geometry of the porous structure can make a change in the dominant deformation pattern of the structure and mechanical properties.

1.3.2.2. Pore size

The size of the pore means the diameter of the inscribed circle of the pores (Figure 1-7). It should be considered carefully because it greatly influences the cell ingrowth (to allow cells grow into pore space) and mechanical properties (Zhao et al. 2018b). Two pore sizes (500 and 1000 µm) are presented in this study. As a result, a larger pore size made a better-spread shape of cells on the surface to have a more robust adhesion and a greater bone ingrowth. This means that the smaller the pore size is, the harder it is for cells to seed. This is an idea agreeing with other studies too (Fukuda et al. 2011; Impens et al. 2010; Karageorgiou and Kaplan 2005). On the other hand, there is a point of view which states that increasing pore size decreases the cell adhesion density (Li et al. 2010; Torres-Sanchez et al. 2017).

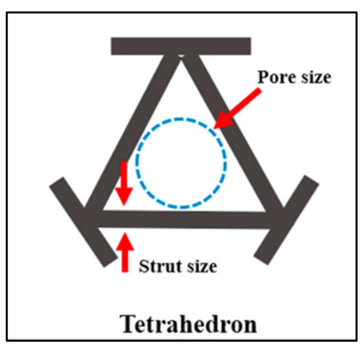

Figure 1-7 The pore and strut size measurements in 2-D
Taken from Zhao et al. (2018b)

When it comes to the effect of pore size on mechanical properties of scaffolds, smaller pore size structure, 500 µm, can tolerate higher stress through fatigue test (Figure 1-8). To sum up, it is important to know what property of porous structure is required, better cell ingrowth or better mechanical properties.

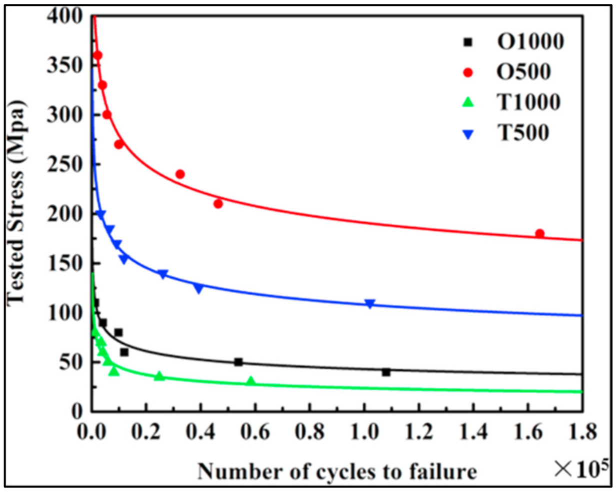

Figure 1-8 Dynamic mechanical properties of SLM-processed titanium scaffolds: S-N curves obtained by compression-compression fatigue testing
Taken from Zhao et al. (2018b)

1.3.2.3. Porosity

Porosity is the volume percentage of the empty pores divided by the volume of the whole structure which can be calculated by the gravimetric method through which $p_{material}$ is the density of the bulk material and $p_{structure}$ is the density of the lattice structure. Also, density can be defined as the division of the mass of material by its volume (Yuan, Ding, and Wen 2019).

$$P = (1 - {}^{\rho_{structure}}/_{\rho_{material}}).100 \quad (1.1)$$

The porosity is the most vital parameter of a lattice structure which affects the mechanical properties (Gibson and Ashby 1999). Two equations are introduced in this study which show that the increase of porosity makes the value of elastic modulus (E) and plastic collapse strength (σ_{pl}) lower (Attar et al. 2015; Esfahani et al. 2016; Yuan, Ding, and Wen 2019). For example, the study by Attar et al. shows that young's modulus is decreased from 145 GPa for fully-dense Ti-TiB material to 84, 73, and 25 GPa for 10%, 17%, and 37% porosity. On the other hand, it mentions that higher porosity may cause higher stress concentration and acceleration of initiation and propagation of cracks.

$$\sigma_{pl} = 0.3\left({}^{\rho}/_{\rho_s}\right)^{3/2}\sigma_{ys} \tag{1.2}$$

$$E = \left({}^{\rho}/_{\rho_s}\right)^2 E_s \tag{1.3}$$

Increasing the porosity of a structure helps to create a proper situation for cell ingrowth and nutrient transformation while it decreases the strength of these structures (Parthasarathy et al. 2010; Ali and Sen 2017). Additionally, enhancing porosity has a negative effect on ultimate compressive strength and compressive stiffness of the structure (Gibson and Ashby 1999). However, there is a more significant drop in compressive strength as compared to compressive stiffness.

According to (Kadkhodapour et al. 2015), the porosity can be modified by changing the diameter of struts in lattice structure. Through this study, the mechanical response of cubic lattice structures with four volume fractions of 10%, 22%, 28%, and 35% was analyzed. Based on the compressive stress-strain diagrams, the level of yield stress and maximum stress under pressure is enhanced by 74% and 84% respectively when the density is increased by 25%. Additionally, the study by (Li et al. 2014) shows that there is an approximate linear relationship between the Young's modulus and density or compressive strength and density. This means when density is enhanced, the strength and young's modulus (the relationship between stress and strain in a material in the linear elasticity regime of a uniaxial deformation) are eager to be increased.

Porosity makes an effect on the Young's modulus, compressive strength, super-elastic property and fatigue properties of porous structures (Liu et al. 2017). By increasing the porosity, Young's modulus, compressive strength and fatigue life decrease while super-elastic property increases (Al-Ketan, Rowshan, and Al-Rub 2018).

- The influence of porosity on corrosion resistance of scaffolds

Moreover, porosity affects the corrosion rate in a way that by reducing the porosity of the material, the corrosion resistance will be increased (Yuan, Ding, and Wen 2019).

- Functionally graded lattice structures

For having both high porosity and high strength and energy absorption, functionally graded porous structures (FGPSs) are presented (Kumar et al. 2016). In contrast to FGPS structures, lattice structures are created generally with a uniform size of unit cells (Ahmadi et al. 2014b; Gonzalez and Nuno 2016; Zhao et al. 2018a). As can be seen in Figure 1-9, the volume fraction of the structure is decreased from bottom to top of the picture (Han et al. 2018).

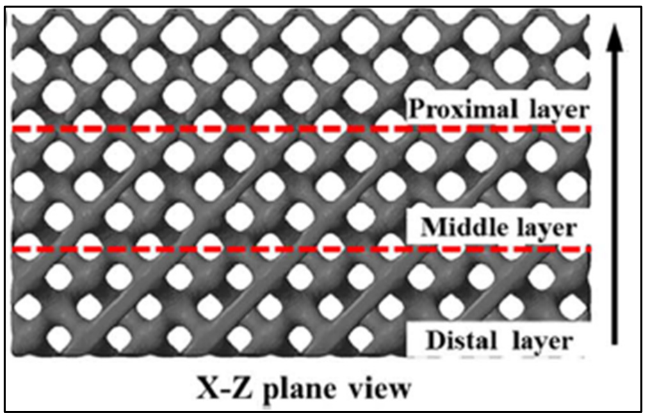

Figure 1-9 The model of Schwarts diamond FGPS
Taken from Han et al. (2018)

When it comes to the distribution uniformity (the consistency of the structure density), it can differ according to the type of porous structure. Some structures like FGPSs are those scaffolds in which the composition and/or the structure change gradually over the volume, resulting in corresponding changes in the mechanical properties of the material. Classification of FGPSs is generally based on the nature of the gradient in material or design. For instance, transition may occur via dispersed to interconnected second phase structure, layered graded or continuously graded structure (Miyamoto et al. 2013), or gradients by volume fraction, shape, orientation or size (Khan 2015).

Xia et al. investigated two types of FGPSs, step-wise gradient and continuous gradient (Xiao and Song 2018). As shown in Figure 1-10, the left-side structure is divided into 3 sections by 2 steps through which the density is changed while the right-side configuration is based on small steps resulting in the change of porosity more gradual along the length. This type of density distribution, one with continuous gradient, is also used in other studies (Han et al. 2018; Yang et al. 2019).

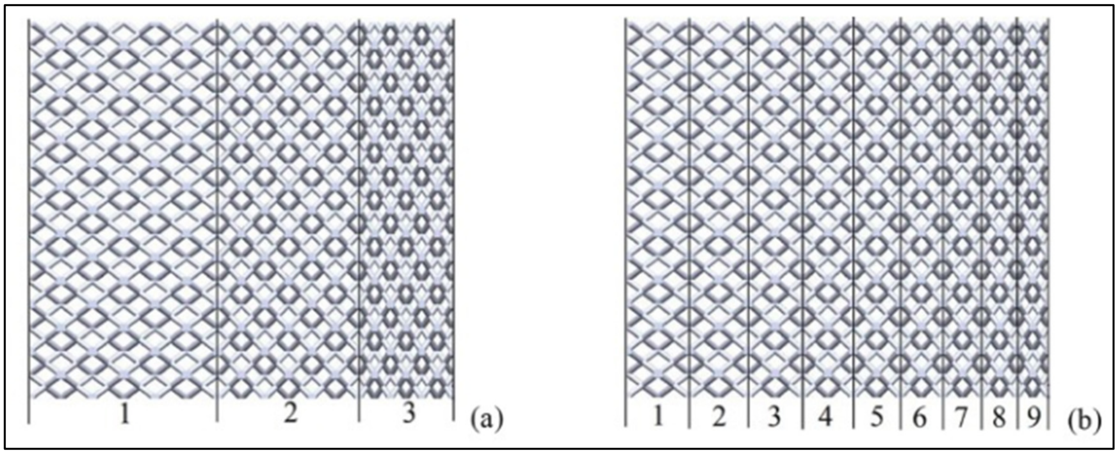

Figure 1-10 Schematic of lattice structure with different density gradient: a) model with a step-wise gradient; b) model with continuous gradient
Taken from Xiao et al. (2018)

In another study, density graded FGPSs fabricated by SLM and using Ti-6Al-4V powder material with design of cubic and honeycomb lattice structures were investigated (Figure 1-11). The FGPS samples were designed with the diameter of lattice struts changing linearly and continuously across cell layers to achieve a smooth density change (Choy et al. 2017).

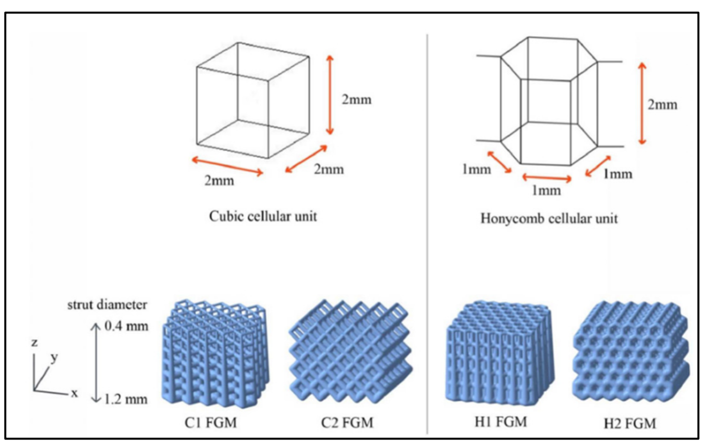

Figure 1-11 Designs of lattice unit and density graded lattice structures with build direction in z-axis
Taken from Choy et al. (2017)

1.3.2.4. Geometric properties of struts

Every porous structure has many horizontal, vertical or inclined struts. The properties of these struts can play an important role in the mechanical properties of the whole structure. These properties include the irregular shape of the surface of the strut, the rotation angle of the strut from the horizontal surface, the segment of the strut and its thickness.

1.3.2.4.1. Inherent irregularity with AM (strut diameter variation)

The irregularity of struts are the constructional variations on the surface of struts, which are caused by manufacturing process. This character is one of the most important factors that ignoring it in modeling makes large differences between the results of numerical models and those of experimental samples. It means if this structural difference is not applied in the numerical model, there is an overestimation in mechanical properties of porous structure in comparison with the strength of experiments (Campoli et al. 2013; Quevedo González and Nuño 2016; Vanderesse et al. 2022).

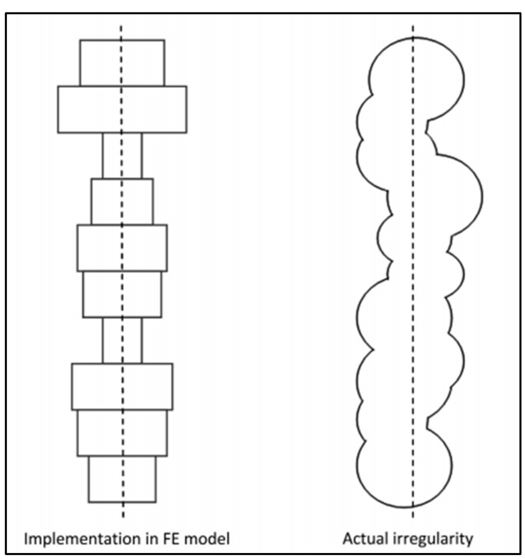

Figure 1-12 Actual manufacturing irregularities and the way they are implemented in the FE models
Taken from Campoli et al. (2013)

As can be seen in Figure 1-12, this irregularity implemented in the numerical model of Campoli et al. as cylinders with different diameters through the cross-section of strut. According to the results, it is found when the standard deviation of the variations in the diameter of the strut cross section increases, the Young modulus of the lattice structure decreases while there is no significant influence on the Poisson's ratio. It is mentioned when the standard deviation of this variation in radius of cylinders increases, there will be intensive irregularity on the surface of strut and less edge length of strut, which ends with being highly deformed under pressure because of not enough connection between circles. As a result, this variation in edge lengths influences the mechanical properties, especially fatigue properties, of lattice structure remarkably and should be applied on struts while modeling (Dallago et al. 2018).

According to another study, this diameter variation in strut is modeled like having a constant diameter of strut that the diameter of powder particle, 100 μm, is added to or substracted from. This means that the minimum strut diameter happens when two particle diameters are subtracted from the main diameter and vice versa (Figure 1-13) (Gonzalez and Nuno 2016). In this study, nine circular beam cross-sections were created in ANSYS. Each cross-section accounted for diameters within $\pm 25\ \mu m$ around its diameter value. A random diameter is defined for each strut ($\emptyset_{rand}$) which is derived from a normal distribution with a standard deviation $\sigma = 75\ \mu m$.

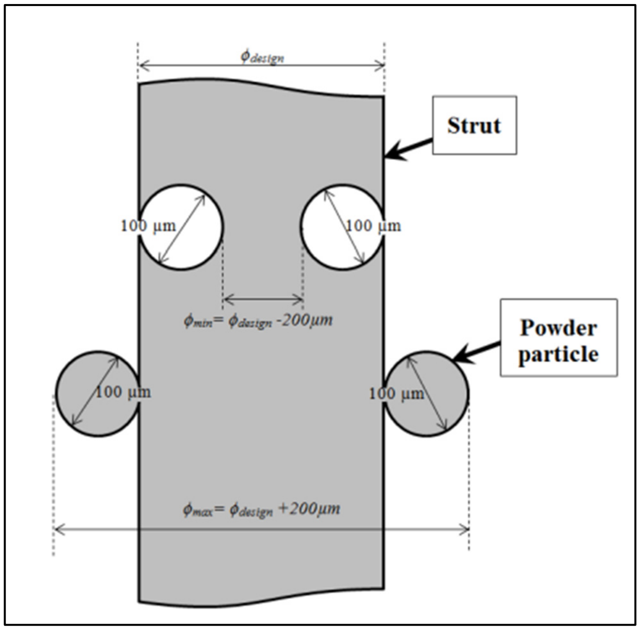

Figure 1-13 Strut diameter variation
Taken from Gonzalez et al. (2016)

According to this paper, this kind of irregularity is one of the reasons why simulation and experimental results vary. More importantly, the main factor influencing the apparent elastic modulus of the lattice structure was found to be the inclination of struts.

This geometrical irregularity is considered in another study, (Zargarian et al. 2016). To implement this factor in the model, it needs to define a random cross section to each strut element along the strut length (Figure 1-14). Therefore, the section of each element is varied inconstantly by the standard deviation of 0.1R where R is the element radius. This study concluded that there was a good agreement between numerical and experimental results. In addition, for simulating cyclic load condition on porous structure, this study is valuable since the prediction of fatigue properties of scaffolds can be well explained.

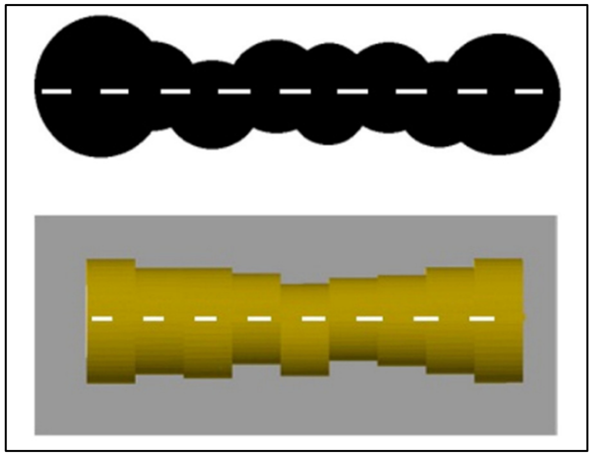

Figure 1-14 Schematic view of the manufactured strut and
its model in the finite element
Taken from Zargarian et al. (2016)

According to (Hedayati et al. 2016), Once irregularities are created in the cross-section of the struts during additive manufacturing process, they decrease the structural stiffness, compressive strength, and durability of the porous structures because not only do they create cross-sections with very small areas, but also they cause stress concentration. Therefore, the elastic modulus is decreased by 10-20% and the fatigue life by 30-70%.

Effect of inherent irregularities on fatigue crack

This inherent irregularity is so important that may cause fatigue crack (Dallago et al. 2018). It is stated that the fatigue crack through the strut is generally initiated from diameter variations of cross-section of strut (Figure 1-15).

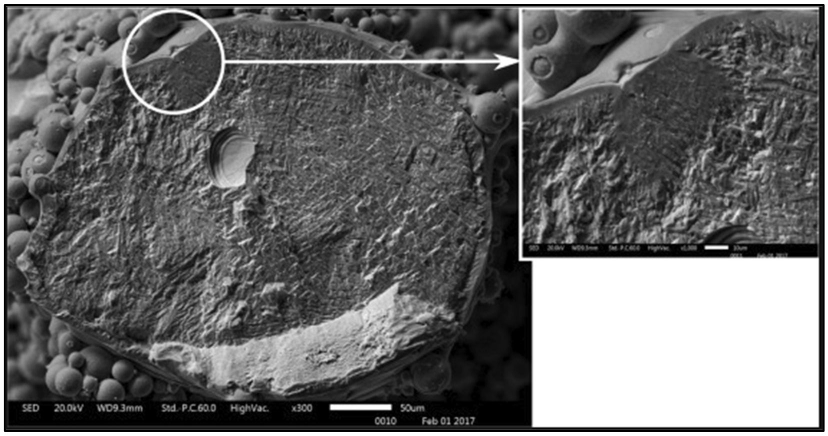

Figure 1-15 Fractured section of a strut after termination of the fatigue test. Note that the fatigue crack nucleated on the surface (detail) and not at the pore
Taken from Dallago et al. (2018)

This study is conversely of the opinion that the elastic modulus parameter is not dependent on the surface variations because this value fits well in both experiments and simulations as a result when the structure is modeled in ideal geometry.

1.3.2.4.2. Geometry of cross-section

This parameter is considered as circular in most of the studies since circular cross-section in comparison to square one does not have sharp notches in its circumference (Figure 1-16)(Smith, Guan, and Cantwell 2013; Dallago et al. 2018; Pérez-Sánchez et al. 2018). Mechanically speaking, it is better to avoid sharp angles while designing a segment because they will be responsible for crack initiation in the section part as load is applied on the structure.

Figure 1-16 Circular cross-section
Taken from Smith et al. (2013)

The cross-section of struts in one lattice structure can be modeled uniformly or with various diameters in different sections (Cao et al. 2018). According to Figure 1-17, the strut of one structure has uniform circular shape with the diameter of 2R while the strut of another one has hourglass-like shape with maximal and minimal section radiuses, R_1 and R_2. It is concluded that the modified unit cell with changing the shape of the strut has better mechanical properties than the original one. Two output parameters, initial yield strength and compressive modulus of the second structure is enhanced by approximately 55% and 79% respectively with considering $\bar{\rho}$ = 0.0621 as the effective relative density.

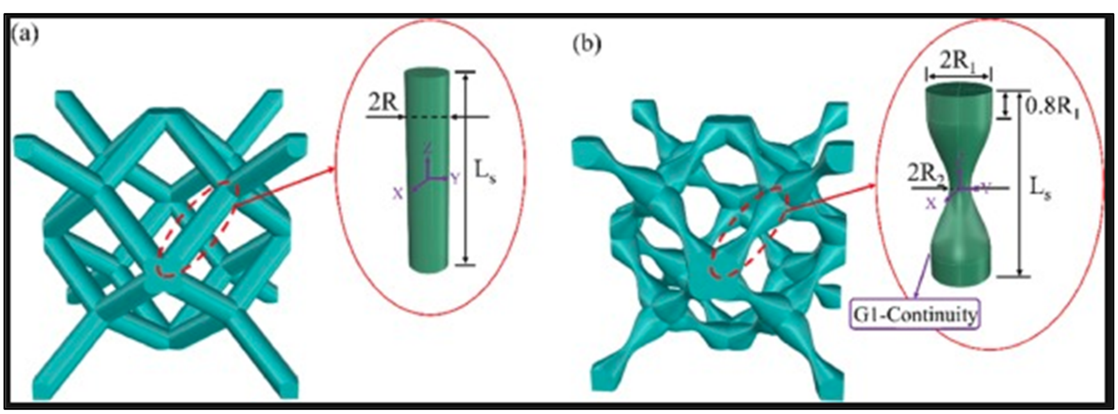

Figure 1-17 The original (a) and modified Rhombic dodecahedron unit cell (b)
Taken from Cao et al. (2018)

1.3.2.4.3. Building direction

The manufacturing parameter affecting the cross-section of a strut is building direction. The building direction is the direction through which the porous structure is constructed. Choosing the angle of the building process depends on the mechanical properties expecting from the lattice structure. It means according to the building direction (0, 90 and 45° to the horizontal plane), powder particles will be melted differently on or beside of each other. When a horizontal strut is fabricated, its cross-section will be elliptical instead of circular just because of the gravity. This phenomenon is neglected when the strut is fabricated vertically (Arabnejad et al. 2016).

In one study, the build direction in all samples with diamond unit cells fabricated by SLM is the same but the build orientation is considered as a variable. Five combinations of unit cells/build orientations during manufacturing are considered (Figure 1-18). Three build orientations (the vertical (VER), diagonal (DIA) and horizontal (HOR)) within the cylindrical sample with fixed unit cell orientation and three unit cell orientations within the cylindrical sample (a vertical or non-rotated unit cell (VER), a unit cell rotation of 45° (VER-45°) and a unit cell rotation of 90° (VER-90°)) with a fixed vertical sample orientation (Wauthle, Vrancken, et al. 2015).

As a conclusion, the unit cell orientation does not seem to affect any of the mechanical properties, although VER-45° and VER-90° do have a slightly lower strength and VER-90° has a slightly lower stiffness. The build orientation has a vital influence on the mechanical properties. The diagonal oriented sample is inferior to both the horizontal and vertical oriented samples that have near identical properties. Both the compressive strength (σ_y and σ_{max}) and the stiffness of the diagonal oriented sample are on average 35% lower compared to the vertical oriented sample (regardless of the heat treatment condition).

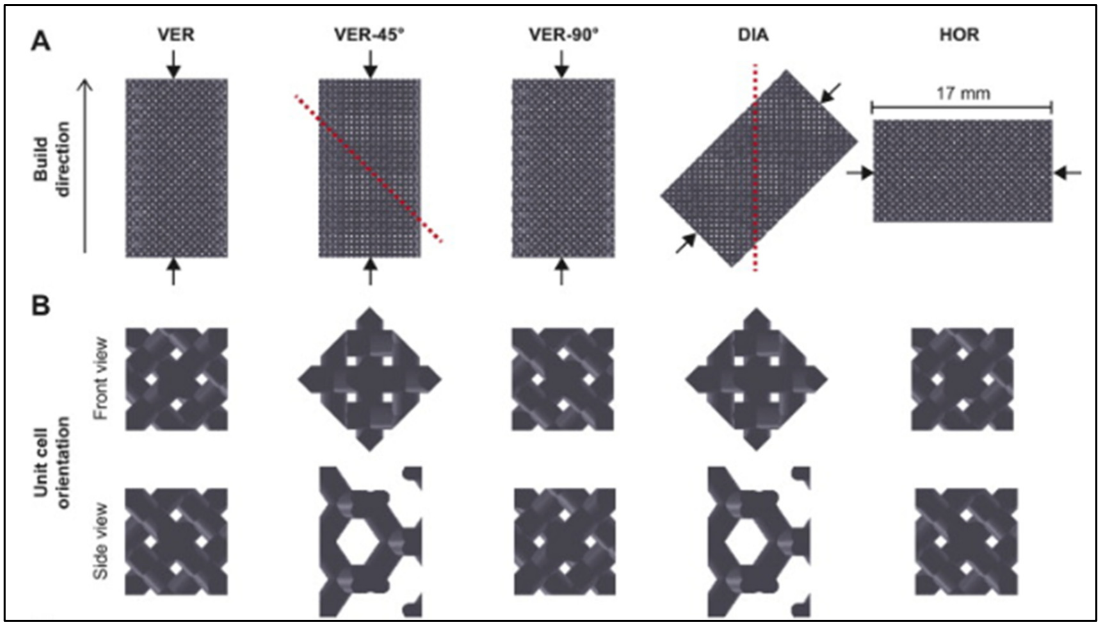

Figure 1-18 Overview of the five series of SLM processed lattice structures (all images are oriented such that the build direction or z direction is in the vertical direction): the cylindrical test samples according to the orientation during SLM manufacturing and indication of the axis of compression testing after manufacturing (A); the front and side view of the corresponding diamond unit cells (B) and the cross-sectional microstructural images of all five series in the three different conditions
Taken from Wauthle et al. (2015)

1.3.2.4.4. Connection between struts

The thickness of strut and that of nodal regions where struts are connected to each other are two parameters influencing the mechanical properties of the whole structure (Figure 1-19). According to the type of unit cell and the expected mechanical properties, the strut diameter is changed. It means that in FGPS structure which is used in (Han et al. 2018), the strut size is changed through the range of 483-905 μm since the porosity is not uniform through the structure. It seems by changing this factor in FGPSs, the elastic modulus and yield strength can be affected because the volume fraction will be changed consequently. According to another study, (Parthasarathy, Starly, and Raman 2011), in which the strut thickness varies (450 and 800 μm), it is said that it affects the stiffness of the porous structure. Based on Table 1-2, it can be seen that by reducing the strut thickness with approximately the same porosity values, 49.75 and 50.75%, the compressive stiffness is decreased by 80.5% and the compressive yield strength by 93.54%. This means that reduction of strut size affects the strength significantly, apart from the overall porosity.

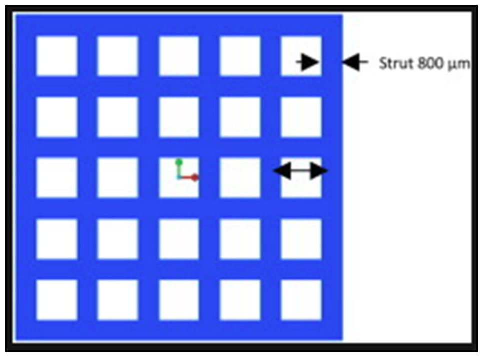

Figure 1-19 Design of cube with porosity 75.83%
Taken from Parthasarathy et al. (2011)

Table 1-2 Compressive stiffness and strength of porous titanium parts
Taken from Parthasarathy et al. (2011)

Set	Porosity (%)	Compressive stiffness (GPa)	Compressive yield strength (MPa)
1	50.75 (±0.69)	2.92(±0.17)	163.02 (±11.98)
2	60.41 (±0.81)	2.68 (±0.12)	117.05 (±5.54)
3	70.32 (+0.63)	2.13 (±0.21)	83.13 (±10.25)
4	49.75 (±1.00)	0.57(±0.05)	7.28 (±0.93)

As far as nodal regions of cellular solids are concerned, the strut thickness is not the same at these areas in some studies. It means that the diameter of strut is enhanced like 0.23 mm at the end of each strut over a length of 0.2 mm (Figure 1-20). This increase is for compensating the contact insufficiency at the intersection of struts (Smith, Guan, and Cantwell 2013). There are other two studies which consent this point of view. The first one by (Labeas and Sunaric 2010), considers the strut thickness increase of 40% in the nodal region with the cause of having higher material concentration in these regions. Also, the second research by (Luxner, Stampfl, and Pettermann 2005), just by increasing the elastic modulus, 1000 times, can increase the stiffness of this region.

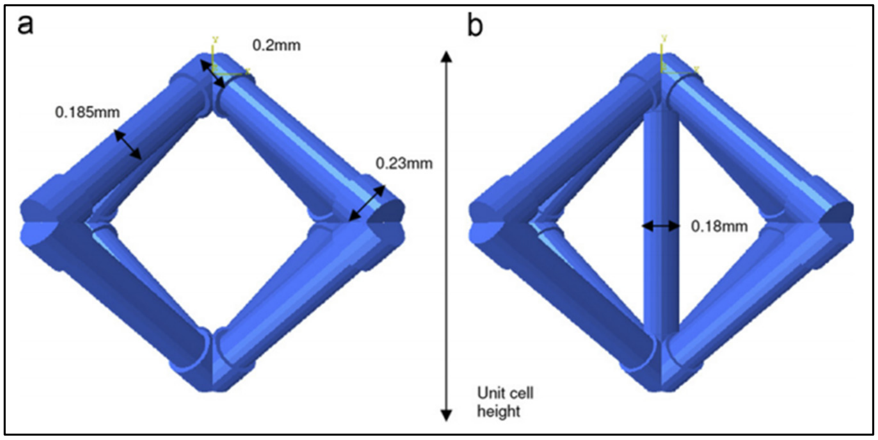

Figure 1-20 Dimensions of the beam element model for (a) the BCC unit cell
and (b) the BCC-Z unit cell
Taken from Smith et al. (2013)

1.3.3. Unit-cell topology

Disparate unique architectures of porous structures exist which make them having different mechanical properties. For instance, there are cubic, face-centered cubic reinforced in the *Z* direction (*F*2cc,*z*), body-centered cubic, hollow spherical, rhombic dodecahedron, diamond and gyroid unit cells. There are two kinds of topologies, stretch-dominated like cubic structure and bending-dominated like diamond scaffold.

Cubic and diamond lattice structures are modeled and studied to see their deformation behavior under load condition (Kadkhodapour et al. 2015) (Figure 1-21).

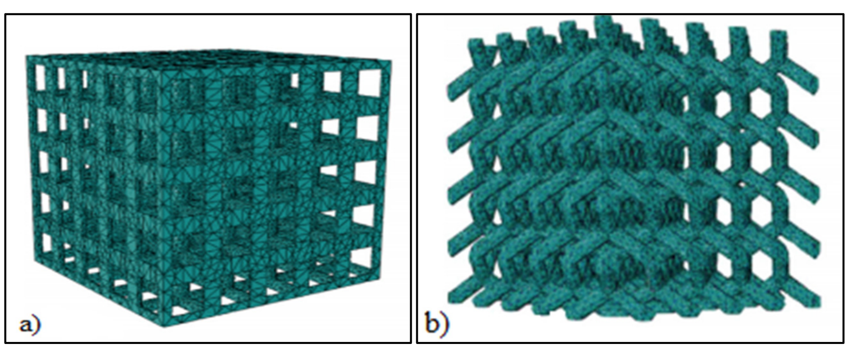

Figure 1-21 Meshed cellular structures : Cubic (a) and Diamond (b)
Taken from Kadkhodapour et al. (2015)

When the cubic structure has parallel struts to the load direction, it is expected to have buckling through struts, which results in having stretch dominated deformation behavior in the structure. This is not the case for diamond structure because of having inclined struts ending with bending of structure.

In case of deformation mode of these two lattice structures, cubic structure has a layer-by-layer deformation mechanism while the second one has a continuous shearing band of 45° (Figure 1-22, 1-23).

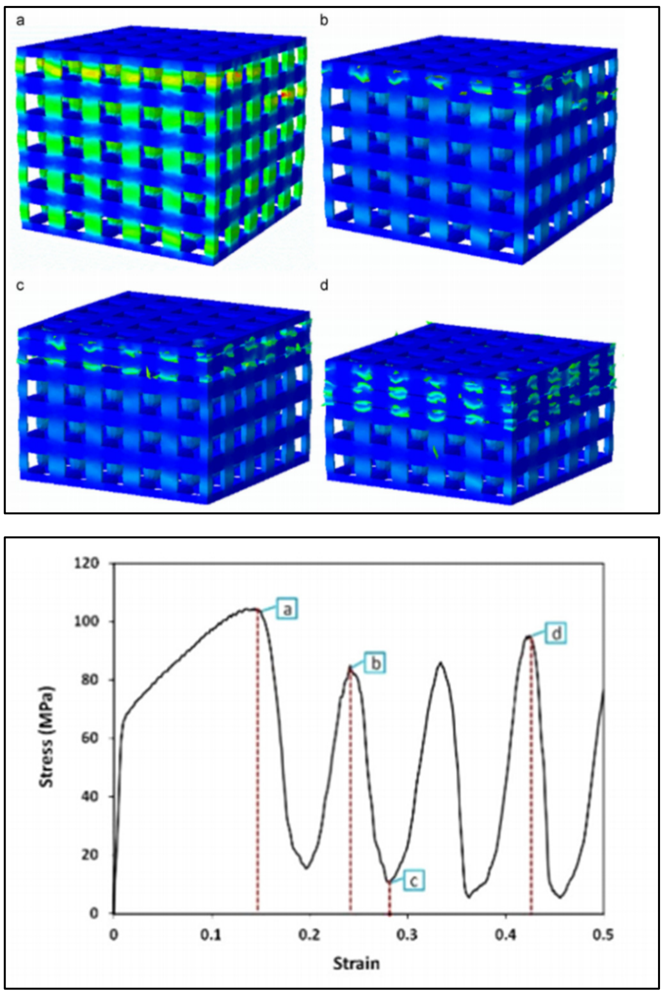

Figure 1-22 Failure mechanism of cubic structure
Taken from Kadkhodapour et al. (2015)

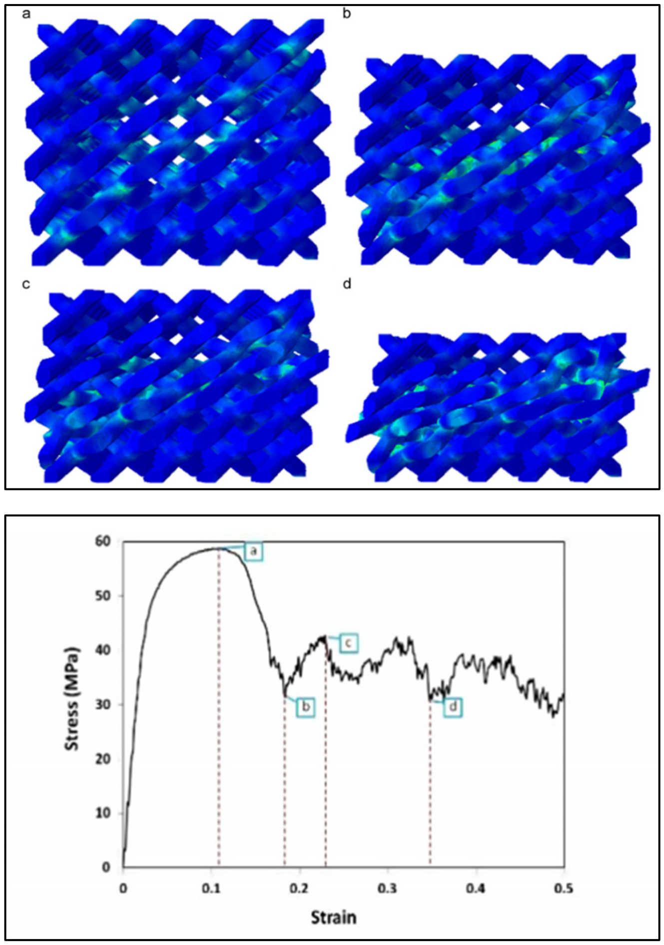

Figure 1-23 Deformation behavior of Diamond scaffold at 22% volume fraction
Taken from Kadkhodapour et al. (2015)

According to this study and other ones, stretch dominated structures, cubic, provide more stiffness and strength as can be seen in the stress-strain curve while structures with bending dominated deformation are beneficial where energy absorption is in need (Abueidda et al. 2019; Ma et al. 2019).

In another study, the excellent value of cubic lattice structures in comparison with body-centered cubic structure (cubic lattice structure with 45° rotation of unit cells) and cross structure is consented due to the fact that they show values of strength and stiffness higher than the other structures under compression load condition (Cuadrado et al. 2017). Figure 1-24 shows the topologies of these structures and figures 1-25 and 1-26 depict how cubic structure stands out when it comes to having high strength and elastic modulus.

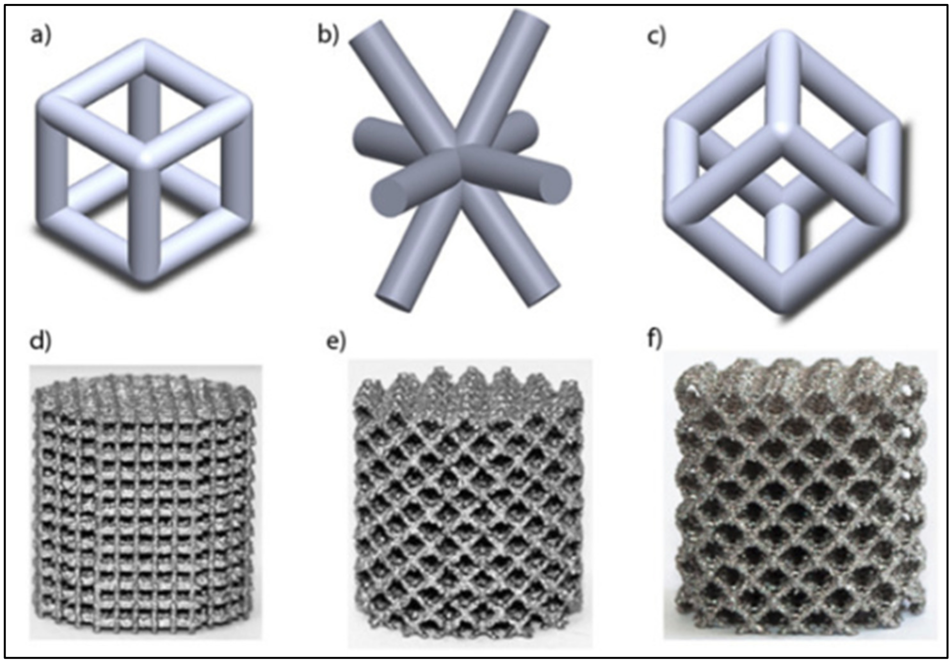

Figure 1-24 (a–c) Schematic drawing of the unit cells used in porous structures and (d–f) the corresponding Ti6Al4V specimens fabricated by EBM with a CAD porosity of 80%. (a and d) cubic structures, (b and e) body-centred cubic structures (BCC), and (c and f) cross structures
Taken from Cuadrado et al. (2017)

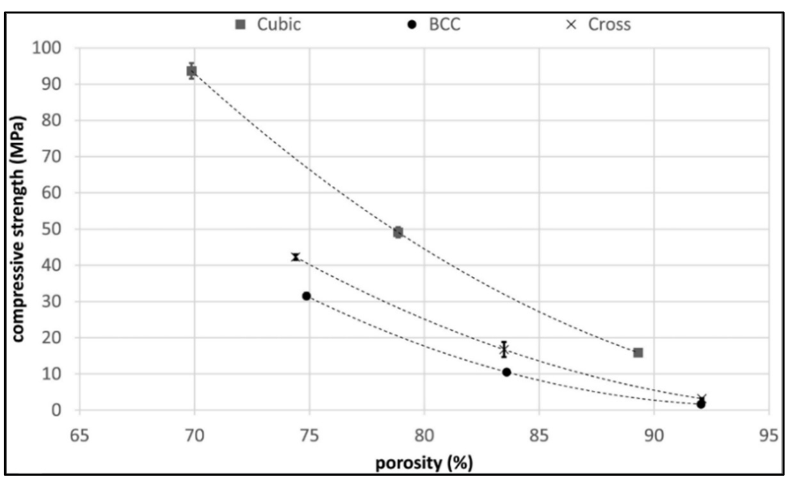

Figure 1-25 Compressive strength as a function of dry weighing porosity (mean, standard deviation and trend curve) obtained from the compression tests for the porous Ti6Al4V structures
Taken from Cuadrado et al. (2017)

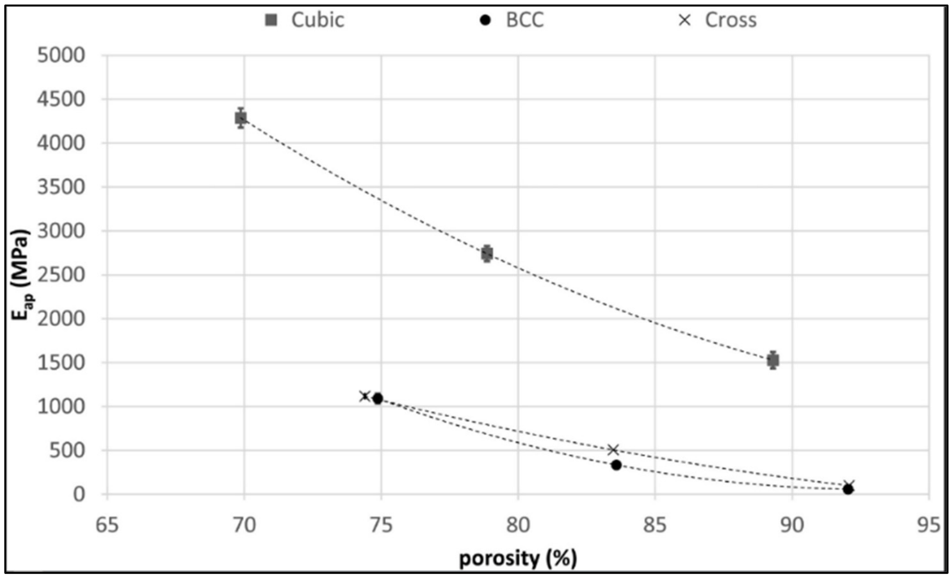

Figure 1-26 Apparent Young moduli as a function of dry weighing porosity (mean, standard deviation and trend curve) obtained from the compression tests for the porous Ti6Al4V structures
Taken from Cuadrado et al. (2017)

Two other porous structures, face centered cubic reinforced in *Z* direction and hollow spherical, are presented in another study to investigate their plastic deformation behavior and mechanical properties (Köhnen et al. 2018). These two topologies with their design parameters such as the number of unit cells and unit cell dimension are shown in Figure 1-27.

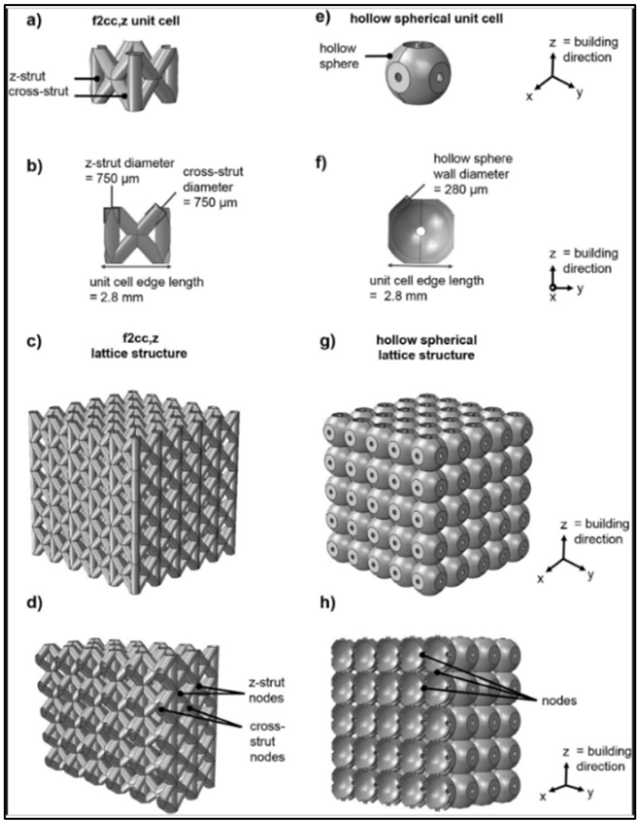

Figure 1-27 CAD illustrations of (a, b) the face-centered cubic f2cc,z unit cell and (e, f) the hollow spherical unit cell with a relative density of 33% referred to fully dense bulk specimens. Dimensions of the unit cell edge length, z-strut, cross-strut and hollow sphere wall diameter are defined in illustrations b) and f). By merging five unit cells in x-, y- and z-directions, a c) f2cc,z lattice structure and g) a hollow spherical lattice structure for compression testing were created. Different types of nodes are highlighted in the cross-section of the d) f2cc,z and h) hollow spherical lattice structures
Taken from Kohnen et al. (2018)

Since the shape of these two structures differs significantly, different deformation behavior is expected consequently. According to this study, the vertical struts in *f2cc,z* structure are responsible for its stretch-dominated deformation mode which results in having higher strength, higher elastic modulus and specific energy absorption in comparison with hollow spherical structure which has bending-dominated deformation behavior.

The rhombic dodecahedron mesostructure is presented in another study to examine the effect of its cell shape on the mechanical properties (Li et al. 2014).

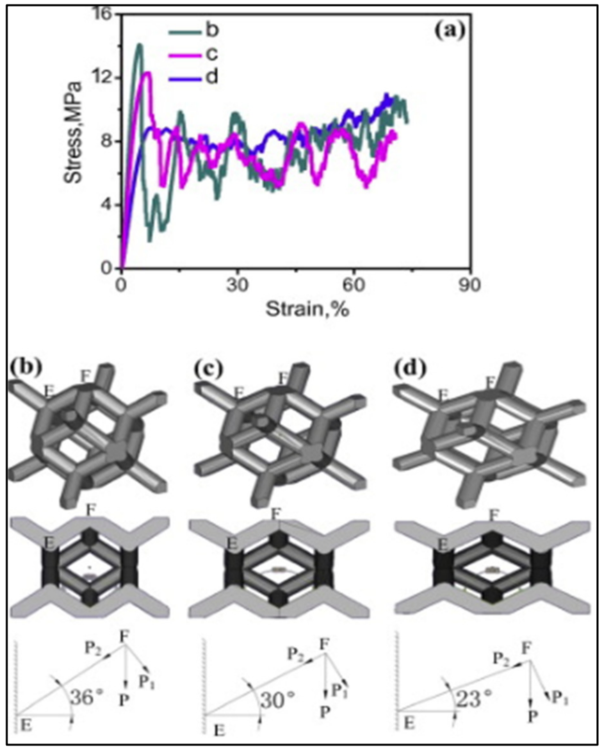

Figure 1-28 (a) Stress–strain curves of the reticulated meshes with different rhombic dodecahedron unit cells; (b) unit cell designed by the Materialise software; (c) and (d) unit cells designed to increase the bending component of the load applied on the struts
Taken from Li et al. (2014)

The angle of inclined strut as a design factor in this topology has a crucial effect on mechanical properties. It means that the structure with the angle value 36° tolerates higher strength level, while the one with 23° has better ductility.

When it comes to the mechanical properties of different lattice structures, five cylindrical scaffolds (diamond (S1), gyroid (S2), orthogonal (S3), truss (S4) and cubic (S5)) are tested under compression load condition (Zhao et al. 2019). This study shed the light on why cubic structure has the highest strength level according to Figure 1-29. The diamond structure experienced the lowest compressive strength, 38.2 MPa, and the gyroid one tolerated at most 57.0 MPa, whereas the structure with cube unit cells endures the highest strength level, 142.8 MPa. The reason of this phenomenon is that scaffolds like diamond and gyroid have complex porosities resulting in leakage of solid bearing surface in the vertical direction while the cubic structure just by having much more simple porosities and more vertical struts is able to tolerate more stress before failure.

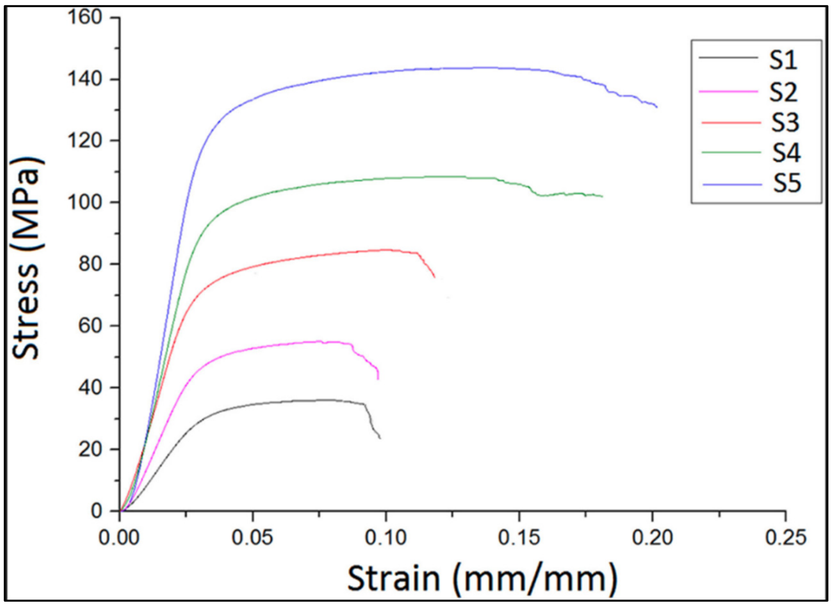

Figure 1-29 Experimental mechanical properties data of different scaffolds
Taken from Zhao et al. (2019)

1.4. Methods of testing for assessing mechanical properties

Conducting different tests such as tensile, compression and fatigue tests to analyze the deformation mode and mechanical properties of porous structures are necessary.

There are two types of tests, quasi-static and dynamic. The strain rate is the main factor making these two tests different. If it is considered as 600 $1/s$ or 1800 $1/s$, the test is called dynamic while the low value of strain rate (0.001 $1/s$) is used for quasi-static test (Xiao and Song 2018).

1.4.1. Quasi-static testing

1.4.1.1. Quasi-static compression test

This kind of mechanical test is performed just by compressing the specimen between two rigid plates with a special load rate to analyze how the structure is deformed and failed. When one porous structure is deformed, a stress-strain curve can be obtained which is unique to this structure with special properties (Ozdemir et al. 2016; Han et al. 2018; Zhao et al. 2018b; Cao et al. 2018; Vanderesse, Richter, Nuño, et al. 2018; Dong and Zhao 2018; Köhnen et al. 2018). The deformation behavior of different unit cells is investigated under quasi-static compression tests. In order to examine the deformation mode of Schwartz diamond functionally graded porous structure, uniaxial compression test is conducted at a loading rate of 0.5 mm/min with using an AG-IC100 KN Electronic Universal Testing Machine with a maximum load capacity of 100 KN at room temperature (Figure 1-30)(Han et al. 2018). Additionally, a digital camera is used usually to keep a track of observation on the entire deformation mode. In another study, the static compression test is performed exactly under the same condition as that in previous study to compare the stress-strain curve of each porous structure (Tetrahedron and Octahedron) (Zhao et al. 2018b). The crosshead of the Instron testing machine moves with the speed of 0.9 mm/min to conduct semi-static compression test on rhombic dodecahedron porous structure (Cao et al. 2018). Figure 1-31 shows how porous structure between two rigid plates is compressed in simulation.

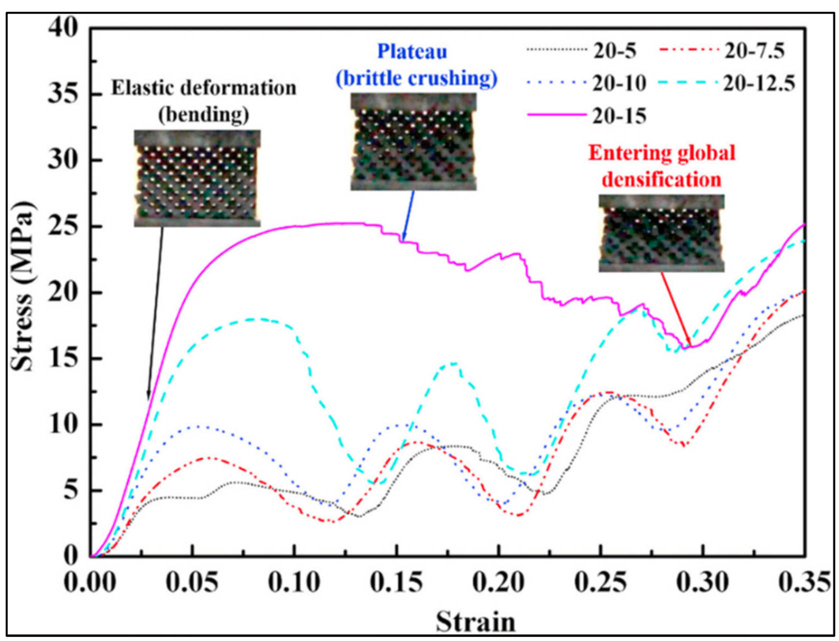

Figure 1-30 Stress-strain curves of the compression tests on the FGPSs with different graded volume fraction from 20% to 5%, 7.5%, 10%, 12.5% and 15%
Taken from Han et al. (2018)

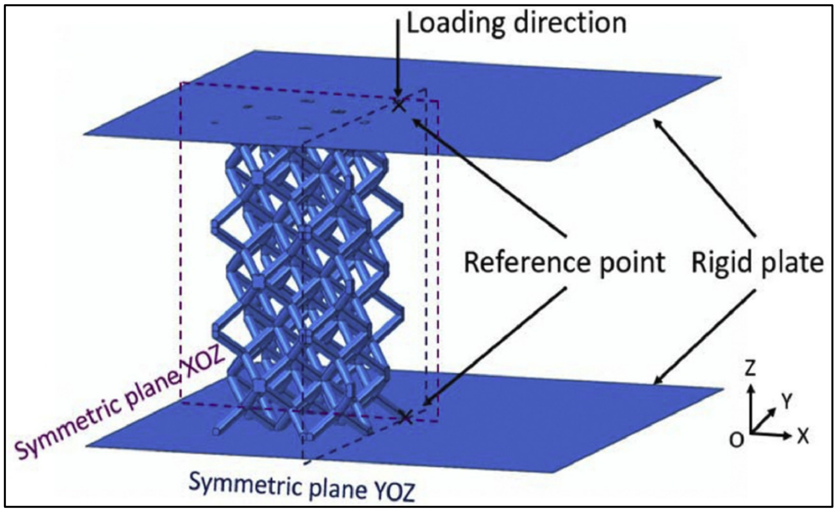

Figure 1-31 Finite element model of the RD lattice structure
Taken from Cao et al. (2018)

To achieve the stress-strain curves of three common lattice structures, cubic, BCCZ and diamond, compression test is conducted (Vanderesse, Richter, Nuño, et al. 2018). According to the Figure 1-32, these structures depict different deformation behaviors. For the cubic structure, a sudden significant decrease of stress happens after tolerating a high amount of stress, more than 60 MPa. The BCCZ structure endures 40 MPa as maximal stress and shows a short plateau of stress at 40 MPa with some fluctuations. The diamond scaffold stands the least amount of stress, around 28 MPa, but it is capable to get deformed extensively before failure point.

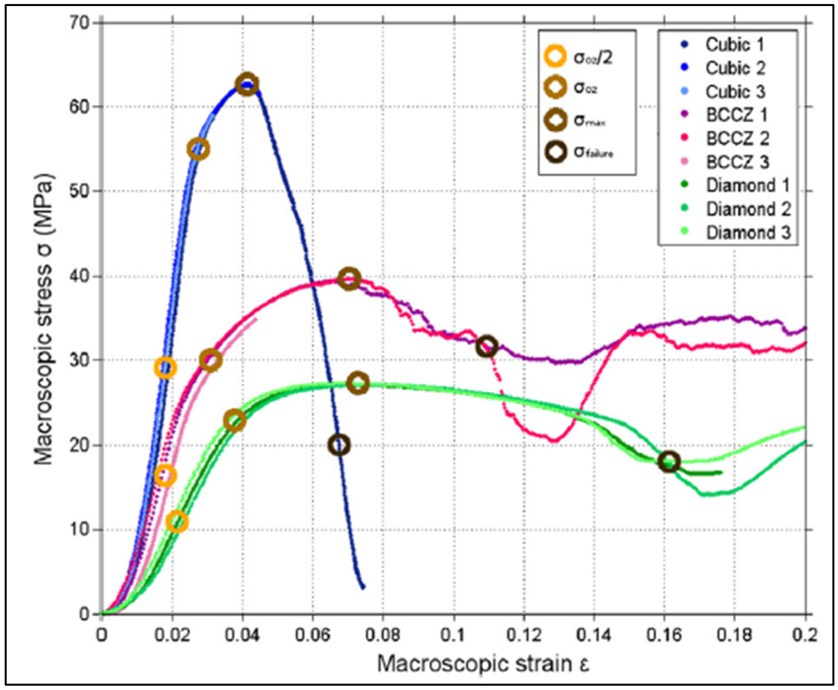

Figure 1-32 Raw compressive stress-strain curves for the cubic, BCCZ and diamond specimens. The circles correspond to approximate σ02/2, σ02, σmax, and σfailure values for all specimens
Taken from Vanderesse et al. (2018)

1.4.2. 2D-DIC for analyzing the strain heterogeneities in lattice structures

Two-dimensional digital image correlation technique is based on the comparison of images of the same object taking before and after applying deformation in two dimensions. The images are differentiated piece-wisely with small subsets in the initial image which are searched in the deformed image. These subsets can be regarded as small squares centered on measurement points where the strain values are going to be evaluated (Vanderesse, Richter, Nuño, et al. 2018).

This technique is used in few studies to study which regions of porous structures sustain the most strain to better understand the deformation behavior of them (Pan et al. 2009a; Campoli et al. 2013; Köhnen et al. 2018; Xiao and Song 2018; Vanderesse, Richter, Nuño, et al. 2018; Radlof et al. 2022).

2D-DIC can be used with other imaging techniques, such as scanning electron microscope (SEM) to measure in-plane strain distribution (Liu et al. 2019; Gong et al. 2022; Wu et al. 2022), or laser scanning confocal microscope (LSCM) to measure out-plane deformation as well (Liu et al. 2019). In (Chen et al. 2016), Ti cubic lattice structures manufactured using SLM were compressed until failure. Digital magnified images were collected at 30 frames per second by a video camera attached to a stereomicroscope to analyze the local vertical strain field in struts through the deformation process. Moreover, digital images taken by 2D-DIC at interrupted steps were used by (Radlof et al. 2022) to characterize local strains on struts and damage behavior of EBM Ti-6Al-4V cubic porous structures under bending and torsional fatigue loading. In another study, (Wu et al. 2022), shear bands and fractures of SLM Ti-6Al-4V cellular solids under uniaxial compression and fatigue loading modes were clearly identified. It is important to mention that digital images were not recorded continuously through entire tests, but at various compressive strains and fatigue cycles. Unlike aforementioned studies, (Vanderesse, Richter, Nuno, et al. 2018) investigated the temporal strain heterogeneities evolution quantitatively by using the whole set of recorded images (250-1500 images per test), instead of few images taken only at selected steps of each test. Through this study, along with recognizing the uncertainties of this technique by means of calibration procedures, the local strain distribution at the surface of three porous structures under uniaxial quasi-static compression loading condition was analyzed. The surface of cubic, body-centered cubic reinforced, and diamond specimens were recorded by a Manta G504-B monochrome video camera equipped with a telecentric lens and a blue LED ring light (Figure 1-33).

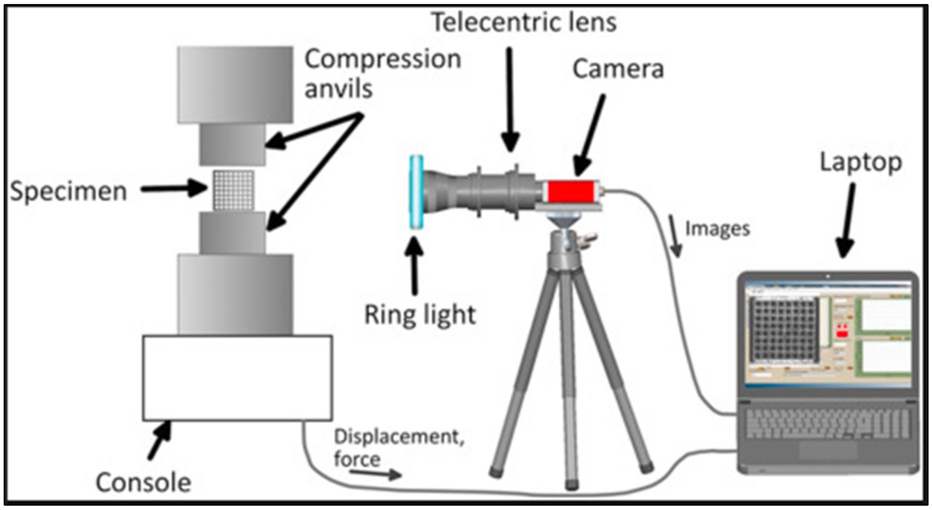

Figure 1-33 Fixture setup for the DIC measurement of lattice specimens
Taken from Vanderesse et al. (2018)

As the images are recorded, they are processed by OpenDIC. This software calculates the planar displacement fields between the image taken before deformation and each image gained within enhancing compression steps.

The deformation behavior of these scaffolds, and especially each strut through typical images at different compression steps ($^{\sigma_{02}}/_{2}, \sigma_{02}, \sigma_{max}$ and $\sigma_{failure}$) are recorded (Figure 1-34). According to these images, it can be detected which regions or struts undergo the highest strain. This phenomenon is called strain localization that can be studied accurately thanks to the significant insights providing with this method.

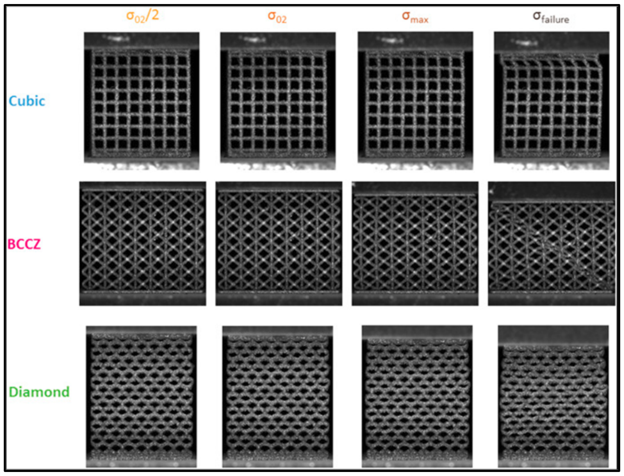

Figure 1-34 Optical images obtained for a sample of each mesostructure at increasing compression steps $\sigma_{02}/2$, σ_{02}, $\sigma_{max,}$ and $\sigma_{failure}$
Taken from Vanderesse et al. (2018)

In another study, the local strain concentrations through SLM stainless steel AISI 316L f2cc,z and hollow spherical porous structures in tension and compression tests was quantified by this technique. To do that, an Aramis camera system manufactured by GOM International AG in combination with Aramis professional software for data processing (Köhnen et al. 2018) was used. As a result, it was recognized that the highest stresses occur at the nodes. For the f2cc,z scaffold, the z struts and nodes of z struts are places where axial strain is localized significantly and even more intense axial strain localization occurs at one specific plane of z-strut nodes. When it comes to strain concentration in hollow spherical structure, it was shown that it happens at the nodes perpendicular to tensile loading direction approximately with the same amount of local axial strain (Figure 1-35).

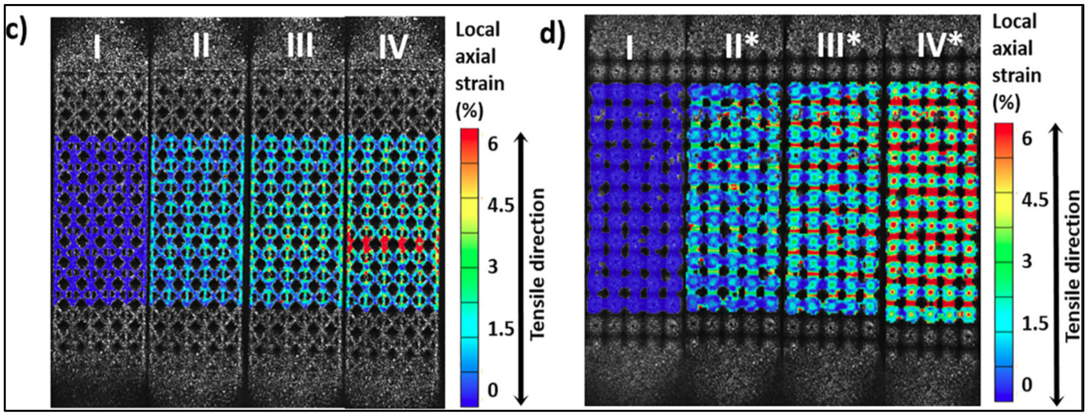

Figure 1-35 Results of DIC analysis for tensile testing of the c) f2cc,z and d) hollow spherical lattice structures revealing strain localization at the nodes perpendicular to the tensile direction. Therefore the cross-sectional area of these nodes was used for the calculation of engineering stress
Taken from Kohnen et al. (2018)

In compression test (Figure 1-36), the strain localization happens mostly at nodes parallel to the load direction for hollow spherical porous structure and at z struts for the f2cc,z.

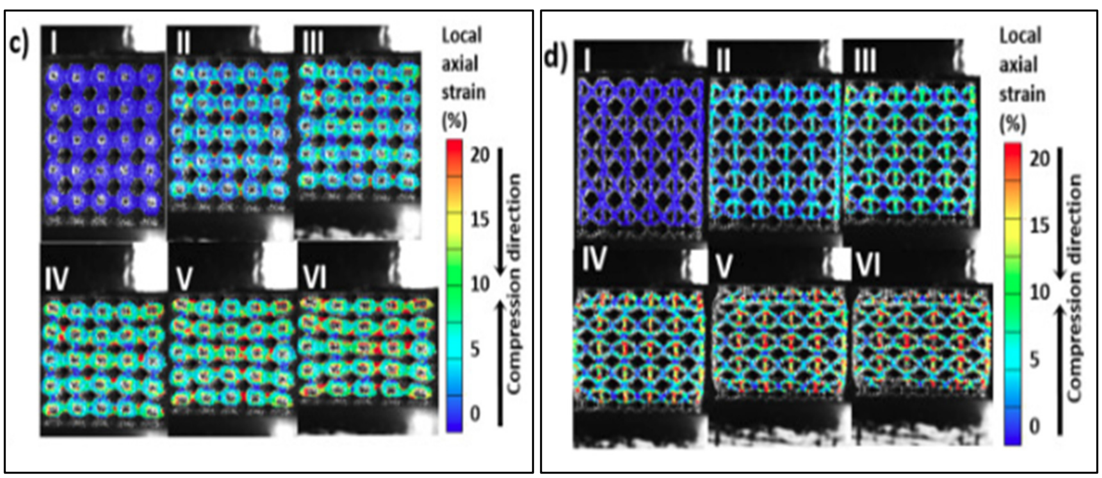

Figure 1-36 c) and d) show the local axial strain of the c) hollow spherical and d) SLM-produced f2cc,z lattice structures with increasing nominal compression strains from 0% to 28%
Taken from Kohnen et al. (2018)

1.5. Material properties of porous structures for clinical application

Among all biocompatible materials such as tantalum, chromium, cobalt and 316 L SS stainless steel, commercially pure titanium and Ti6Al4V are believed to be one of the most suitable biomaterials for medical applications (Parthasarathy et al. 2010). This is because of its high biocompatibility, high strength-to-weight ratio, and excellent mechanical properties such as relatively suitable elastic modulus, fracture toughness and fatigue strength (Lautenschlager and Monaghan 1993; Geetha et al. 2009; Kadkhodapour et al. 2015).

For instance, the compressive properties of EBM-processed Ti-6Al-4V lattice structures was investigated. It was found that the Ti-6Al-4V lattice structure exhibited superior load-bearing and energy absorption capacities than aluminum foams and stainless steel scaffolds with the same porosity (Xiao et al. 2015). The use of titanium has some significant advantages over alloyed titanium (Wauthle, Ahmadi, et al. 2015). Firstly, it is biologically inert. It means that there is no potential hazardous or toxic alloying components such as V and Al, which could cause allergic reactions. Secondly, titanium possesses superior corrosion resistance in comparison with other metallic biomaterials like stainless steel and Co-based alloys (Chen and Thouas 2015). Thirdly, titanium has similar ductile mechanical behavior to pure tantalum with a lower material cost and easier fabrication process (Wauthle, Ahmadi, et al. 2015). Also, the high ductility of titanium can lower the crack initiation and propagation by softening the material as loaded (Jamshidinia et al. 2014; Wieding et al. 2013; Zhao et al. 2018b).

1.5.1. Material chemical composition

Ti-6Al-4V-ELI titanium alloy powder is used to manufacture porous structures. The chemical composition (in percentage) of this material is shown in Table 1-3.

Table 1-3 Chemical composition of Titanium Ti6Al4V-ELI based on ASTM F136

Al	V	Fe max.	O max.	C max.	Ni max.	H max.	Ti
5.5-6.5	3.5-4.5	0.25	0.13	0.08	0.05	0.012	Balance

1.5.2. Stress shielding in orthopaedic implant

Implants with an appropriate elastic modulus can prevent stress-shielding. A significant mismatch between the elastic moduli of an orthopedic implant and its surrounding bone can trigger the so-called stress shielding, which occurs when the physical stresses are taken up by the implant rather than by the bone. Stress shielding may lead to implants loosening and eventually premature failure of the implant (Ryan, Pandit, and Apatsidis 2006). The elastic modulus of cancellous bone is in the range of 22.4–132.32 MPa, whereas that of cortical bone is much higher, ranging from 7.7 to 21.8 GPa (Ataee et al. 2018; Poumarat and Squire 1993). Metal implants should exhibit an elastic modulus mimicking that of natural human bone. However, the elastic modulus of metallic implants normally exceeds that of bone; for instance, the elastic modulus of commercially pure (CP) Ti and Ti6Al4V is around 112 GPa and 115 GPa, respectively, much higher than that of cortical bone. Thus, reducing the elastic modulus to an appropriate value is important for the implant design (Yuan, Ding, and Wen 2019). This issue is mentioned by other authors to reduce the stress shielding and improve the implant longevity (Yan et al. 2012; Gong et al. 2012; Zhao et al. 2018b).

1.5.3. Mechanical properties of titanium porous structures

Wauthle et al. investigated the difference between the compressive and fatigue properties of pure titanium and Ti6Al4V alloy porous structures. The results showed that pure titanium is suitable for cyclically loaded porous implants. Moreover, microstructure also affects the fatigue behavior of porous structures. For porous Ti6Al4V fabricated by SLM, the α' martensite has a detrimental effect on the fatigue life as a low ductility phase (Li et al. 2017). The microstructure of titanium is α phase and the grain size is lower than 10 μm, which could provide higher fatigue resistance (Wang et al. 2017). Additionally, it is concluded that Ti6Al4V is mechanically stronger for low cycle fatigue ($< 10^4$ cycles) applications, whereas titanium is superior for high cycle fatigue ($> 10^5$cycles)(Wauthle, Ahmadi, et al. 2015). Although Ti6Al4V is widely used in the load-bearing implant, tantalum showed excellent in attachment, proliferation, and differentiation of human osteoblasts. The ductile mechanical behavior and the higher fatigue strength are one of the key factors for the use of porous tantalum implants

(Wauthle, van der Stok, et al. 2015). Owing to high material cost, the use of tantalum in orthopedic implants is expected to remain relatively limited. The comparison can bring titanium back in the medical industry since it has a lower cost compared to tantalum and has no toxic alloying components like other titanium alloys (Zhao et al. 2018b).

1.6. Summary

The literature review has presented the existing research on fabricating and modeling of porous structures by additive manufacturing. Various methods were introduced to model, fabricate and even characterize the mechanical behavior of these structures (Figure 1-37). Additionally, the main design parameters (pore size, porosity, distribution uniformity and some properties of struts as their thickness, length, inclination, irregularity along length and cross-section) affecting the mechanical properties of scaffolds were explained and discussed to understand better what issues are available today that researchers have not been able to overcome. In the next chapter, the proposed research problem is explained.

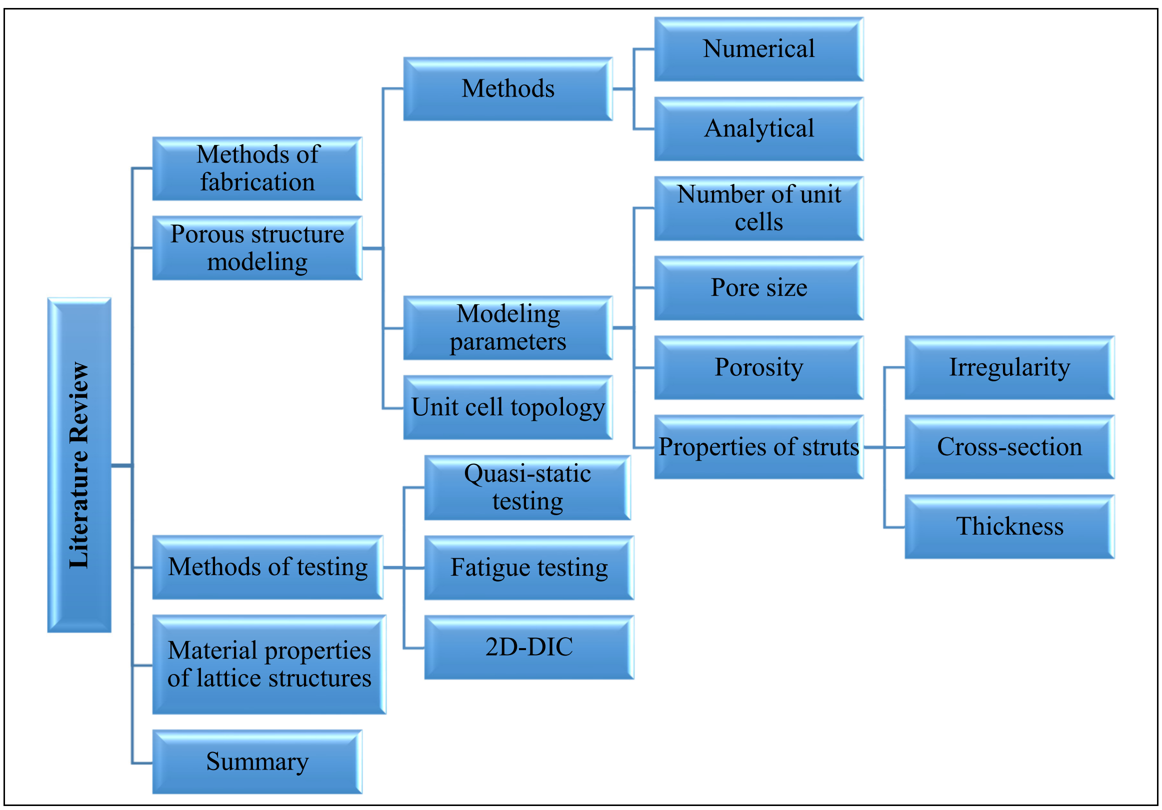

Figure 1-37 Diagram of literature review

CHAPTER 2

CONTEXT OF RESEARCH

2.1. Introduction

In previous chapter, a comprehensive literature review introduced titanium porous structures and their problems. In this chapter, the research problem and the objectives of this study are described.

2.2. Research problem

Nowadays, researchers usually create a numerical model of lattice structures by using a commercial software (ANSYS or ABAQUS) firstly and then, to make sure the results of simulations are the same as the real condition, some samples are fabricated which are called prototypes. After analyzing the appearance and mechanical properties of experimental samples, it is possible to understand that there are some differences. One of the main differences is that AM device makes the surface of each single strut with lots of irregularities, which are not modeled through software. If this characteristic is not modeled appropriately in numerical model, it consequently results in not being able to predict the mechanical properties of lattice structure exactly (Campoli et al. 2013).

Additionally, there are some other fabrication parameters, which affect how well powder particles are placed close to each other. If the laser power and its travel speed are not selected properly, like those in welding, the particles while sintering will be over-melted or unmelted. Therefore, mechanical properties of the final part will be dependent on these two factors (which is not the study case here).

Therefore, the concern of this research is to know:

- How the 3D-printed structure does not have the same mechanical properties as the ideal numerical model?
- How do manufacturing irregularies affect the deformation behavior of these structures?
- How to predict the behavior of porous structure under compressive load condition with a numerical model considering the manufacturing errors (manufacturing irregularities).
- ✓ Apparent elastic modulus (Eap)

2.3. Research objectives

The main objective of this research is analyzing the strain heterogeneity over each face of porous structures, and developing a numerical model for orthopedic application with mechanical properties close to those of experiments (quasi-static compression).

1) ***Main goal*:** Assessing how heterogeneous the deformation behavior is over struts of each face in these samples.
2) ***Secondary goal***: Predicting the behavior of the structure with a valid numerical model having manufacturing irregularities to be able to reproduce the experimental results.

CHAPTER 3

METHODOLOGY

3.1. Introduction

In this chapter, the procedure through which these samples are manufactured and analyzed is described. Firstly, Ti6Al4V cubic porous structures are manufactured by laser powder bed fusion technique and SLM method. Secondly, preparation procedure is done (i.e. initial height measurement, surface polishing, and image taking by LEXT laser confocal microscope). Next, quasi-static compression tests are performed with the presence of 2D-DIC and extensometer. Then, LEXT images are taken from three faces of sample 3, polished-lateral-faces again after the test. Finally, the out-put data (stress-strain curves, strain histograms, and strain maps) is processed, compared, and analyzed.

3.2. Manufacturing of cubic samples

Three cubic porous structures were fabricated using selective laser melting on a base. An EOS M280 machine with input parameters of laser power 280W, scanning speed 1200 mm/s, wave length 1064 nm, laser beam diameter 80 µm, hatch spacing 140 µm, and layer thickness 30 µm was used. The powder used in this method was Ti6Al4V-ELI with average particle size of 40 µm. The samples were designed to have a porosity of 75% with strut thickness 600 µm. These samples were printed along a direction inclined by 45° with respect to longitudinal direction in order to have beams with diameters as close as possible to their respective 3D model (600 µm), and to avoid having different cross-sections in vertical and horizontal beams (Lafarga et al. 2017). After cutting them from the solid stainless steel base using a fixed axis circular saw (Figure 3-1), they were cut from the bottom susbstrate using Electron Discharge Machining. The samples were formed by the repetition of eight unit-cells in three directions, ensuring convergence of the mechanical properties towards those of an infinite medium (Quevedo Gonzalez and Nuno 2016). This ended with macroscopic dimensions $14.71 \times 14.74 \times$

14.73 mm^3 with standard deviation 0.04 for each dimension. Finally, samples were heat treated in argon at 800 °C for 4 hours to relieve the internal stress.

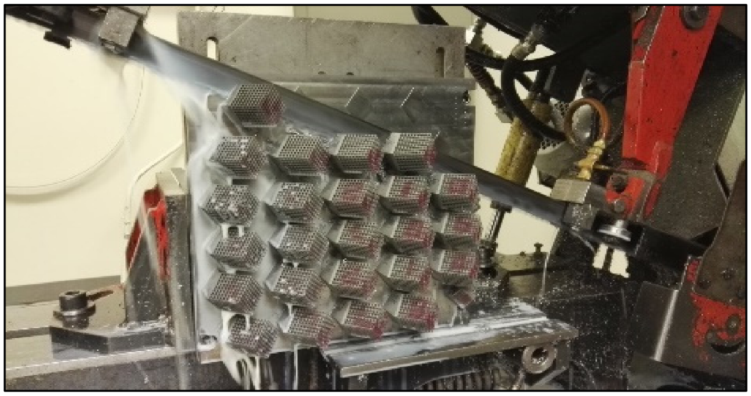

Figure 3-1 Cutting the samples from the solid stainless steel substrate

3.3. Sample preparation procedure

To prepare these three structures for mechanical tests, different procedures were performed on each one (i.e. polishing, paint-spraying lateral faces, taking images from lateral faces, and measuring initial and final heights). The preparation steps for each sample is as following:

#1 (normal specimen):

1. Measure initial height
2. Paint lateral faces with boron nitride
3. Record images of the 3 lateral faces before the compression test
4. Install contact extensometer
5. Compression test displacement 1 mm displacement
6. Record images of the 3 lateral faces after the compression test
7. Measure final height

#2 (specimen with polished compression faces):

1. Polish compression faces to make them parallel
2. Measure initial height
3. Paint lateral faces with boron nitride
4. Record images of the 3 lateral faces before the compression test

5. Install contact extensometer
6. Compression test 1 mm
7. Record images of the 3 lateral faces after the compression test
8. Measure final height

#3 (specimen with polished lateral faces):

1. Measure initial height
2. Polish vertical (lateral) faces
3. Paint with black/white speckle
4. Scan lateral faces with LEXT confocal microscope
5. Record images of the 3 lateral faces before the compression test
6. Install extensometer
7. Compression test 1 mm
8. Record images of the 3 lateral faces after the compression test
9. Measure final height

3.3.1. Polishing of samples and chemical etching

To prepare these three samples for quasi-static compression test, three conditions were considered: First sample was considered as-printed (no polishing); two compressive faces were polished on the second sample; three lateral vertical faces were polished on the third sample (Figure 3-2). The polishing on these faces was done using coarse to ultra-fine sandpapers (320-400-600-800-1200). This step was followed by submerging each sample in the beaker with half-full water and putting it in the ultrasonic device for two minutes. After washing and drying it, the related surface was analyzed under the microscope frequently to check the roughness level and polishing depth, in order not to pass half of the strut's diameter and have finished surface; Meaning if polishing with coarse sandpapers removed half of the strut's diameter, to just fine the surface with 800 or 1200 sandpapers. On third sample, in addition to polishing three lateral vertical faces, chemical etching with Kroll solution (HF $(2ml) + HNO3\ (5ml) + H2O\ (100ml)$ was performed to be able to scan these faces before and after the test by laser scanning confocal microscope (LEXT).

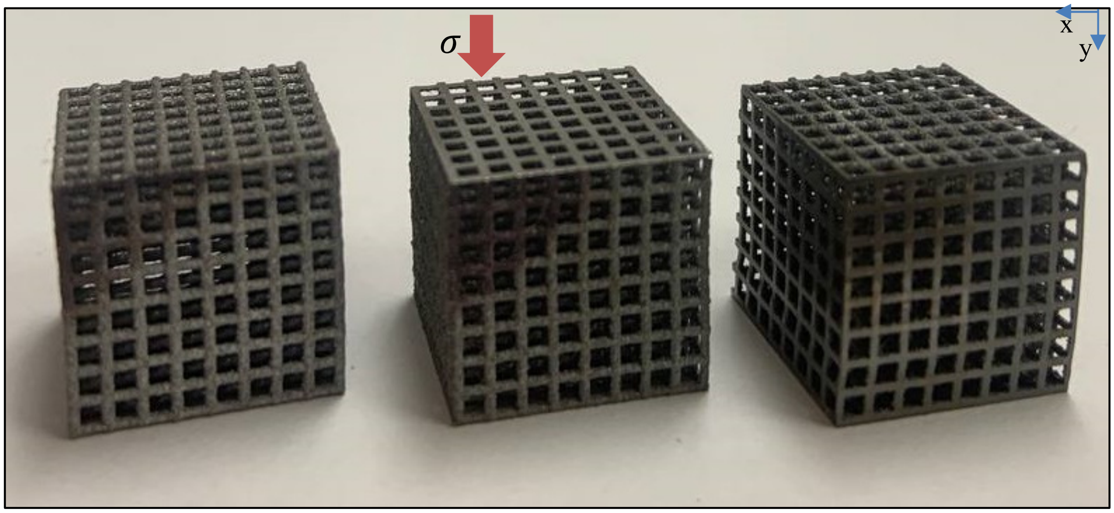

Figure 3-2 Samples 1, 2, and 3, from left to right

Apart from this, images were taken from all three lateral vertical faces of three samples before and after the test. Recording three lateral faces of each sample instead of only one face, and their local deformations were the novel points in my work.

3.3.2. Checking parallelism of compression faces

Initial and final heights for each sample was measured by using digital height gauge, dial test indicator (Mitutoyo, 513-206), and 15 mm rectangular gauge block (Figure 3-3). In addition, to check if fabricated cubic structures have parallel compression faces (top and bottom faces), 5 height points (4 corner points and 1 central) were measured manually. This measuring system was repeated after reversing the samples to make sure the height value of each point (Figure 3-4). To do that, firstly, the number on digital height gauge was reset when the dial indicator probe was on the gauge surface. After placing the sample under the gauge (based on flasher on lateral face, which shows upper face), the probe of dial indicator is placed on 5 points as shown before. Then, the number identifying the height of sample is read when the indicator is on 0.02 mm (assumption). This procedure is performed for measuring all points. As the result, all measures for before and after test are presented below.

Figure 3-3 Showing digital height gauge, dial indicator, and rectangular gauge block from left to right

Table 3-1 Measuring initial and final height of three samples before and after the test

Samples	Initial height (mm)	Final height (mm)	Height reduction (%)
Sample 1	14.80±0.05	14.44±0.05	2.4
Sample 2	14.27±0.12	13.94±0.06	2.3
Sample 3	15.01±0.09	14.33±0.03	4.5

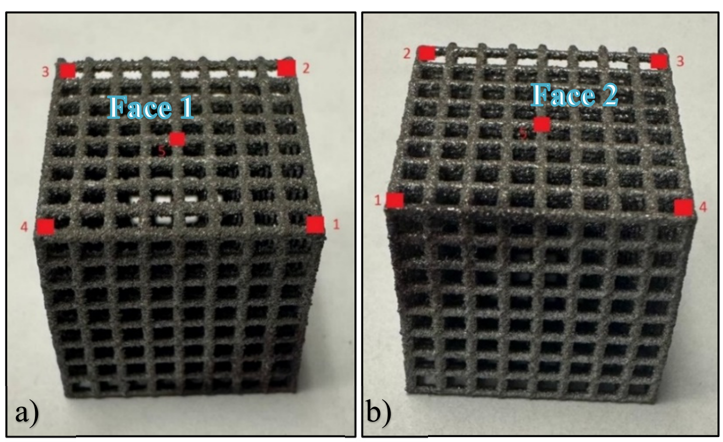

Figure 3-4 Showing 5 height points measured on face 1 and face 2

Table 3-2 Checking parallelism of compression faces

	Face 1			**Face 2**		
	Sample			Sample		
Height (mm)	1	2	3	1	2	3
point 1	14.74±0.03	14.25±0.03	14.77±0.03	14.84±0.03	14.35±0.03	14.79±0.03
point 2	14.75±0.03	14.15±0.03	14.77±0.03	14.86±0.03	14.27±0.03	14.77±0.03
point 3	14.73±0.03	14.29±0.03	14.76±0.03	14.79±0.03	14.42±0.03	14.78±0.03
point 4	14.77±0.03	14.36±0.03	14.7±0.03	14.84±0.03	14.51±0.03	14.72±0.03
point 5	14.78±0.03	14.26±0.03	14.78±0.03	14.84±0.03	14.42±0.03	14.78±0.03
Average	**14.75**±0.03	**14.26**±0.03	**14.76**±0.03	**14.83**±0.03	**14.39**±0.03	**14.77**±0.03

3.3.3. Scanning lateral faces with LEXT confocal microscope

The reason why one of the samples has three polished lateral faces is being able to scan them by LEXT before and after the test, which results in high-resolution images. As settings of scanning, brightness was set to 4980 and 4740 for top and bottom layer with 25 steps of imaging. Therefore, 80 sectional images were taken sequentially and then, they were stitched as .bmp image (with overlap 25%).

3.3.4. CNC machining of the compression pieces between machine anvils and the samples

Two compression pieces of MO40 alloy were designed in CAD and then, they were machined by CNC (Figure 3-5, Figure 3-6). They were used to locate the porous structures between machine anvils accurately. The two oblique planes on two sides of these two pieces were designed to place the extensometer on the porous structures freely.

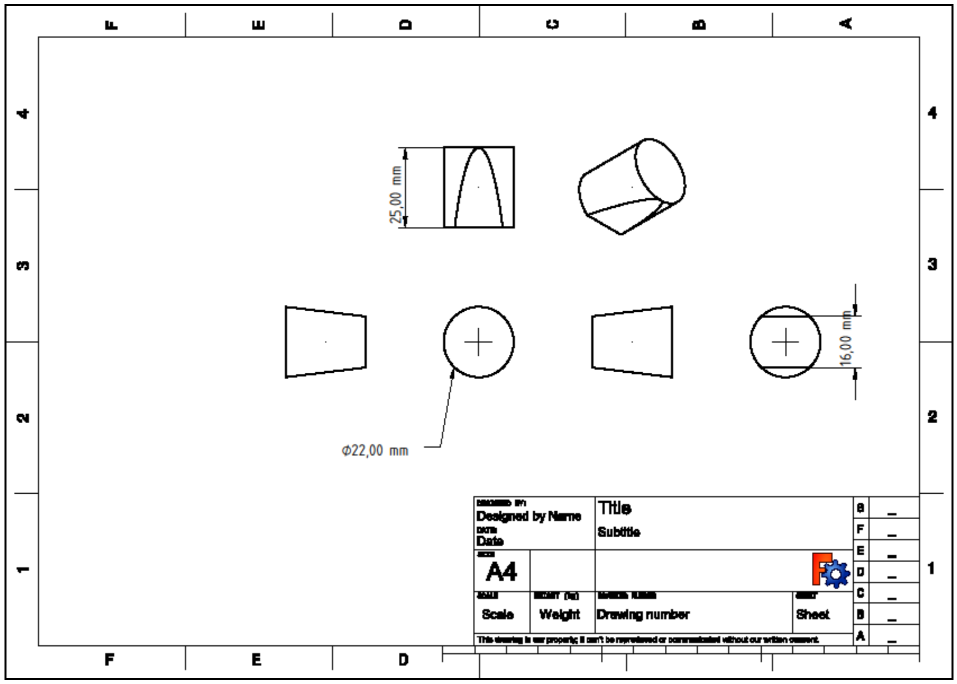

Figure 3-5 Technical drawing for CNC machining of support compression pieces

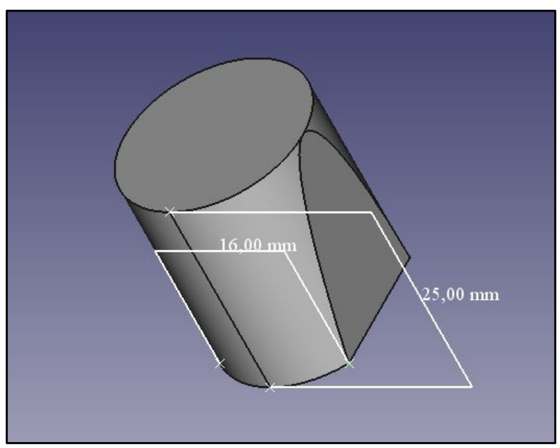

Figure 3-6 MO40 Support compression pieces

3.4. 2D-DIC and extensometer set-up

In all tests, one face of each sample was recorded using digital image correlation technique. Before each test, to optimize the gray scale of the images taken by the camera, the sample face (in front of the camera) was spray painted with mate white boron nitride. The images used for

DIC measurements were recorded by a Manta G504B monochrome camera using a telecentric lens manufactured by Allied Vision Technologies. This camera was mounted on a carbon fiber tripod with a high precision head (Figure 3-7). This setup helped to have a contactless actual time analysis of the one face heterogeneous deformation process by using a two-dimensional (2D) digital image correlation (DIC) technique (Chen et al. 2016; Chen et al. 2022). Additionally, it is noteworthy to remark that the reliability of the DIC setup was assessed using a protocol established by a recent study (Vanderesse, Richter, Nuno, et al. 2018).

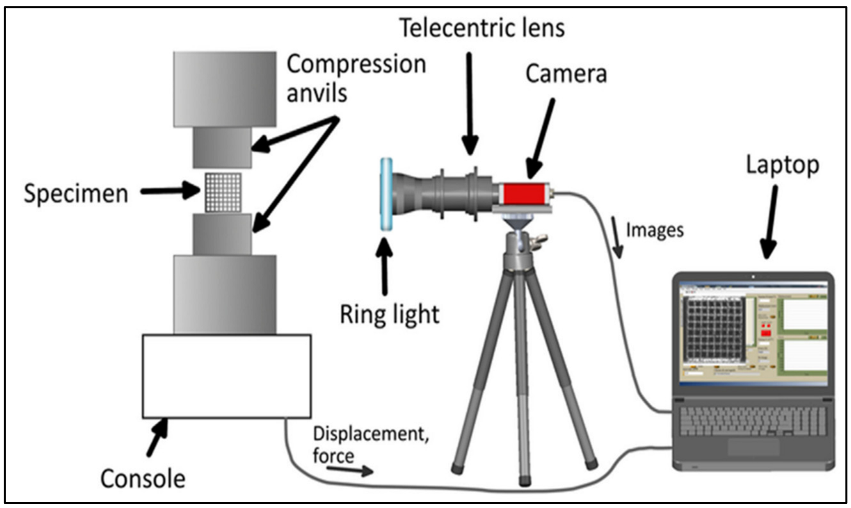

Figure 3-7 DIC setup to record images from cubic mesostructure
Taken from Vanderesse et al. (2018)

Regarding the lens of the camera, the optical aperture was set between f/5.6 and f/8 to prevent the optical distortion. The ring light installed on the camera was 144 blue LED to improve the quality of images. This test was recorded at 3-4 frames per second by means of a custom LabVIEW program synchronized with the testing machine. Each of these three tests was performed in 70 seconds with having 265-279 images. Each image had dimension of 2452×2056 pixels. After the tests, digital image correlation software, OpenDIC, was used to process the BMP images; this software was developed at LOPFA, École de Technologie Supérieure, Montréal (Vanderesse et al. 2013). In addition to BMP images as input files, post-processing parameters were needed to be able to process them. Post-processing parameters, especially the subset size and spacing, were set to 21 and 5 pixels, respectively. Then, Fiji software was used to analyze the output files from OpenDIC, Csv files and Log file. Finally, strain fields, displacement fields, and quality index files were obtained to investigate strain distribution through samples' faces by having strain maps.

In conjunction with machine and DIC data, the MTS contact extensometer was installed on one face of each sample to record the strain data. This extensometer with initial gauge length of 12.7 mm and the compression span of 2.52 mm was installed on the sample face behind the one in front of the camera (Figure 3-8).

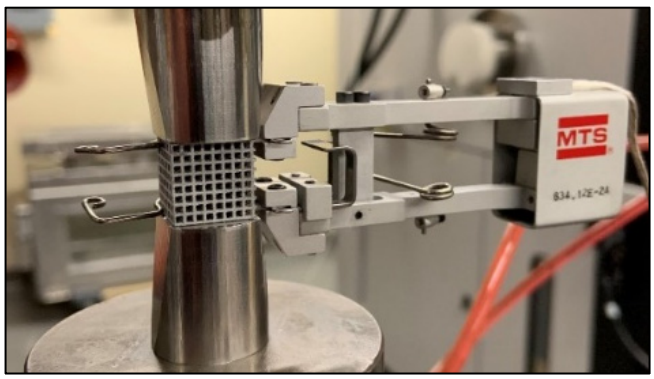

Figure 3-8 Installation of MTS contact extensometer on one sample

3.5. Quasi-static compression test

Uniaxial quasi-static compression tests were carried out at a strain rate of $10^{-3}\,s^{-1}$, in accordance with ISO 13314, using an MTS Alliance RF/200 machine (MTS, Eden Prairie, MN, USA) with a maximum load capacity of 200kN. To perform the tests, samples were placed between two machined pieces (Lincoln 718) and machine anvils. After applying a preload of 50 N, Samples were compressed with loading direction parallel to y direction (perpendicular to the compressive faces). All samples were loaded to reach a maximum 1 mm of anvil displacement. The stress-strain curves were computed using the load-displacement data recorded by the machine.

3.6. Calculation of the apparent young's modulus

In order to recognize the young's modulus value of these structures, the slope of stress-strain curve in the linear elastic region must be calculated. For this purpose, the stress-strain graphs were obtained by having the load, area (cross-section of sample), initial and final length. Then, the young's modulus and linear elastic region length were calculated. Since the curves start with concave region, and not with linear region, it is essential to find the inflection point of the curve instead of the slope of the curve at first. The inflection point is where the curvature sign of this S-curve is changed. At the early stage of the curve, the curvature sign is positive, while after the inflection point, the sign goes negative (Figure 3-9). The way to find the position of this inflection point is considering an approximate linear part of the stress-strain curve around the inflection point (10-50 MPa stress), and draw the trendline with a suitable order of polynomial over this curve. Then, different order values from 1 to 6 were tried to see which one fits better on the curve. R-squared value on the chart is a criterion, which shows the fitting accuracy of the trendline on the curve. In addition, there is an option in the trendline format where it is possible to display the equation of the trendline. The R-squared value shows the best fit condition when it is closer to 1. By checking this value in each time of changing order value from 1 to 6, it was found that the best polynomial order value is 4 with R-squared value 0.99996. The order values of 5 and 6 were not selected since not only did not they give better fit (only 0.00001), but also they made the equation more complicated than order value 4. On the other hand, order values 2 and 3 were not selected since they were not accurate enough to mimic the curvature of the curve. Next, the equation was derived once and twice to obtain the first derivative (Y') and second derivative equations (Y''). By finding the root of the second derivative equation, the x value (strain value) where inflection point is placed, was obtained. By placing this x value in the main equation, the stress value of this point was calculated. Then, this x value was placed in first derivative equation to gain the slope of the curve in this point, which is young's modulus value. This procedure was performed for all three samples and three methods.

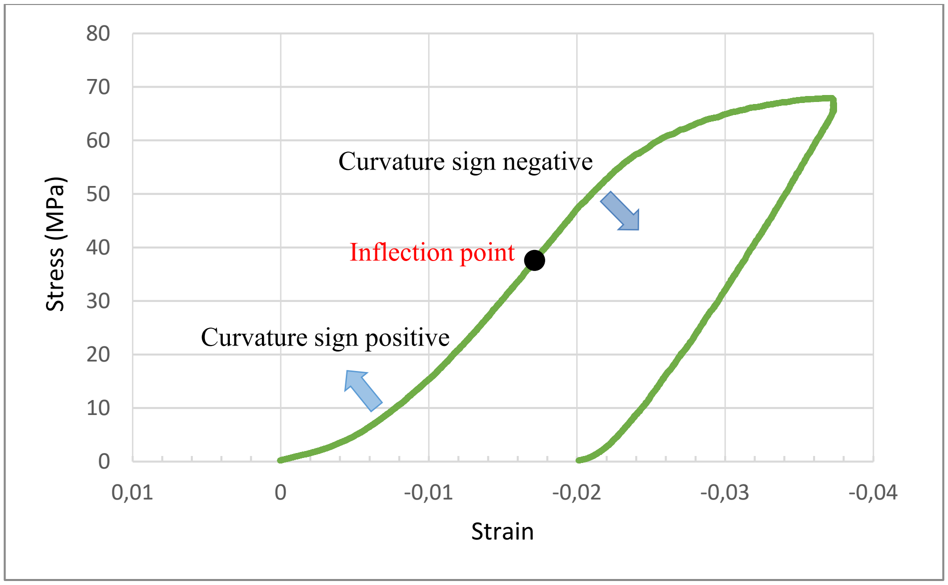

Figure 3-9 Stress-strain curve for sample 2 from machine data

3.7. Calculation of the apparent yield stress ($\sigma_{y,ap}$)

In order to find the apparent yield stress point, a line parallel to the linear elastic region of the stress-strain curve was sketched from 0.2% strain. The coincidence point of this parallel line with the stress-strain curve determines the apparent yield stress location. Therefore, this process is performed for all stress-strain curves of three samples.

3.7.1. Calculation of the apparent yield stress for stress-strain curves obtained from machine

To calculate the apparent yield stress, a line parallel to the linear elastic region of the stress-strain curve must be drawn. Since the stress-strain curves derived from the machine have a concave (non-linear) region at first, it must be removed to be able to draw a parallel line to the linear region from 0.2% strain, and then, calculate the apparent yield stress. Therefore, all stress-strain curves for three samples were started from 11 MPa stress and after drawing the parallel line, $\sigma_{y,ap}$ was calculated (Figure 3-10).

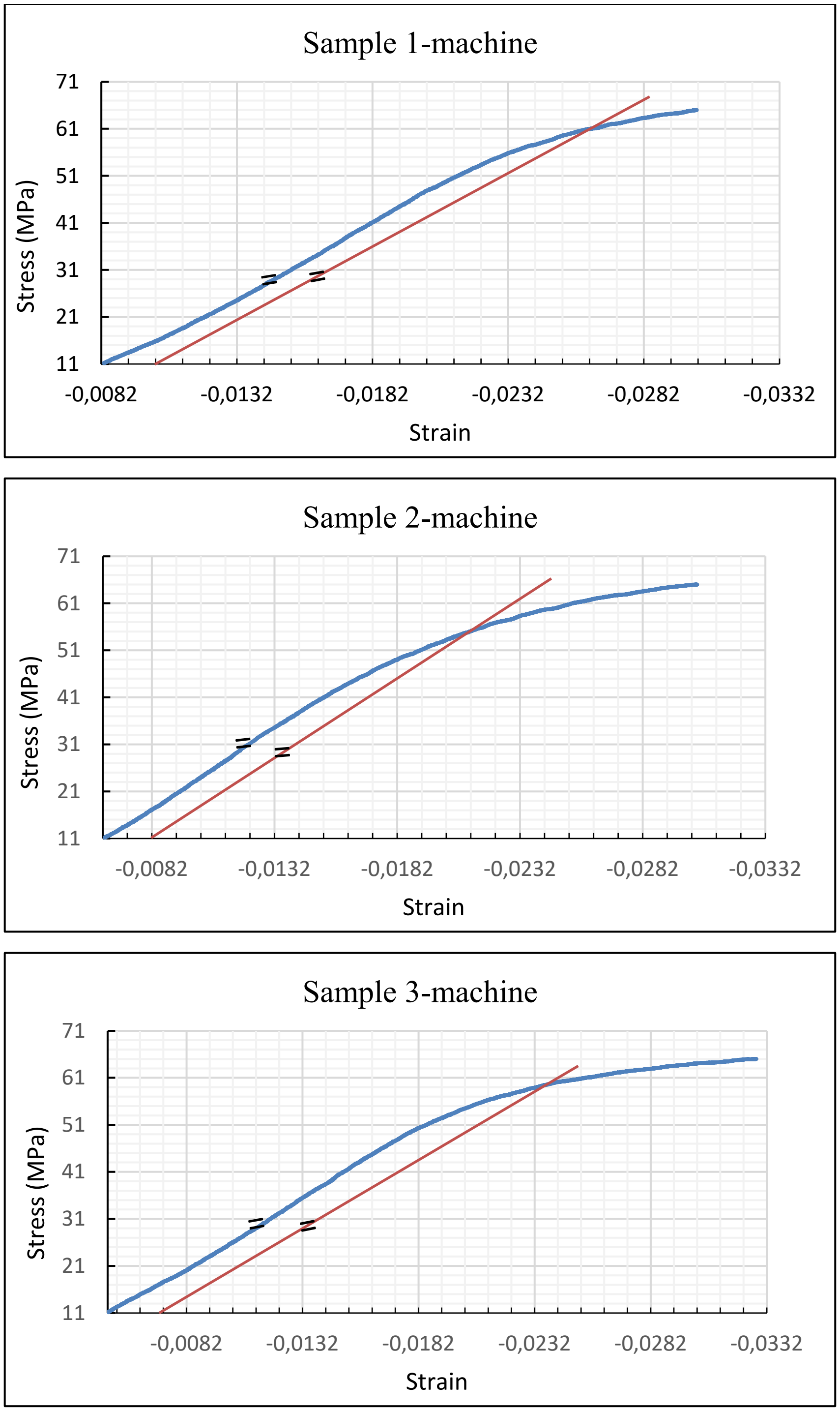

Figure 3-10 Calculation of the apparent yield stress based on stress-strain curves obtained from the machine for three samples

Unlike the stress-strain curves from the machine, those derived from the extensometer and DIC start with linear region at first. Therefore, a line parallel to the linear region from 0.2% strain was drawn, and then, the apparent yield stress was calculated (Figure 3-11, Figure 3-12). Finally, the stress and strain values related to apparent yield points for all samples and methods are displayed in Table 3-3.

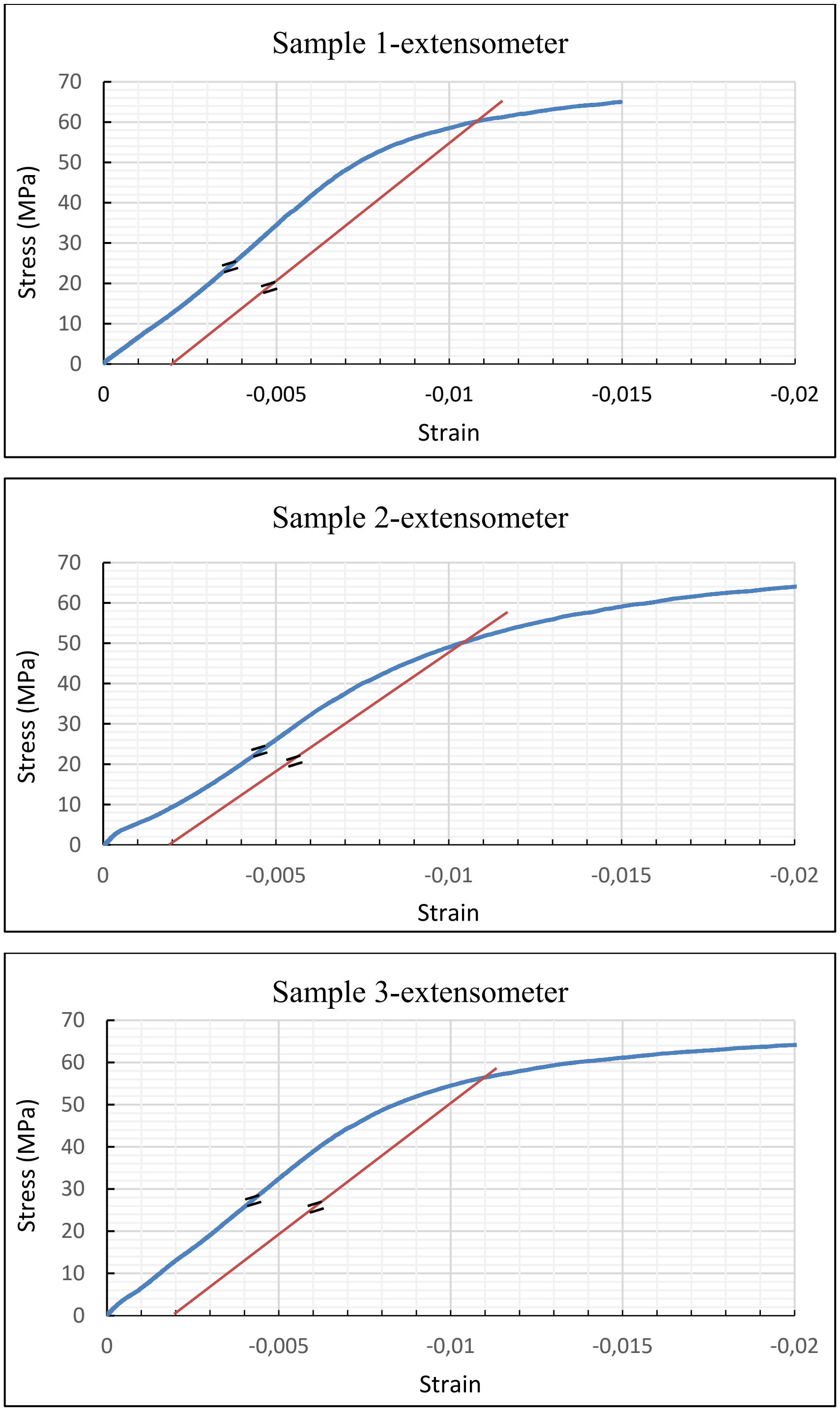

Figure 3-11 Calculation of the apparent yield stress based on stress-strain curves obtained from the extensometer for three samples

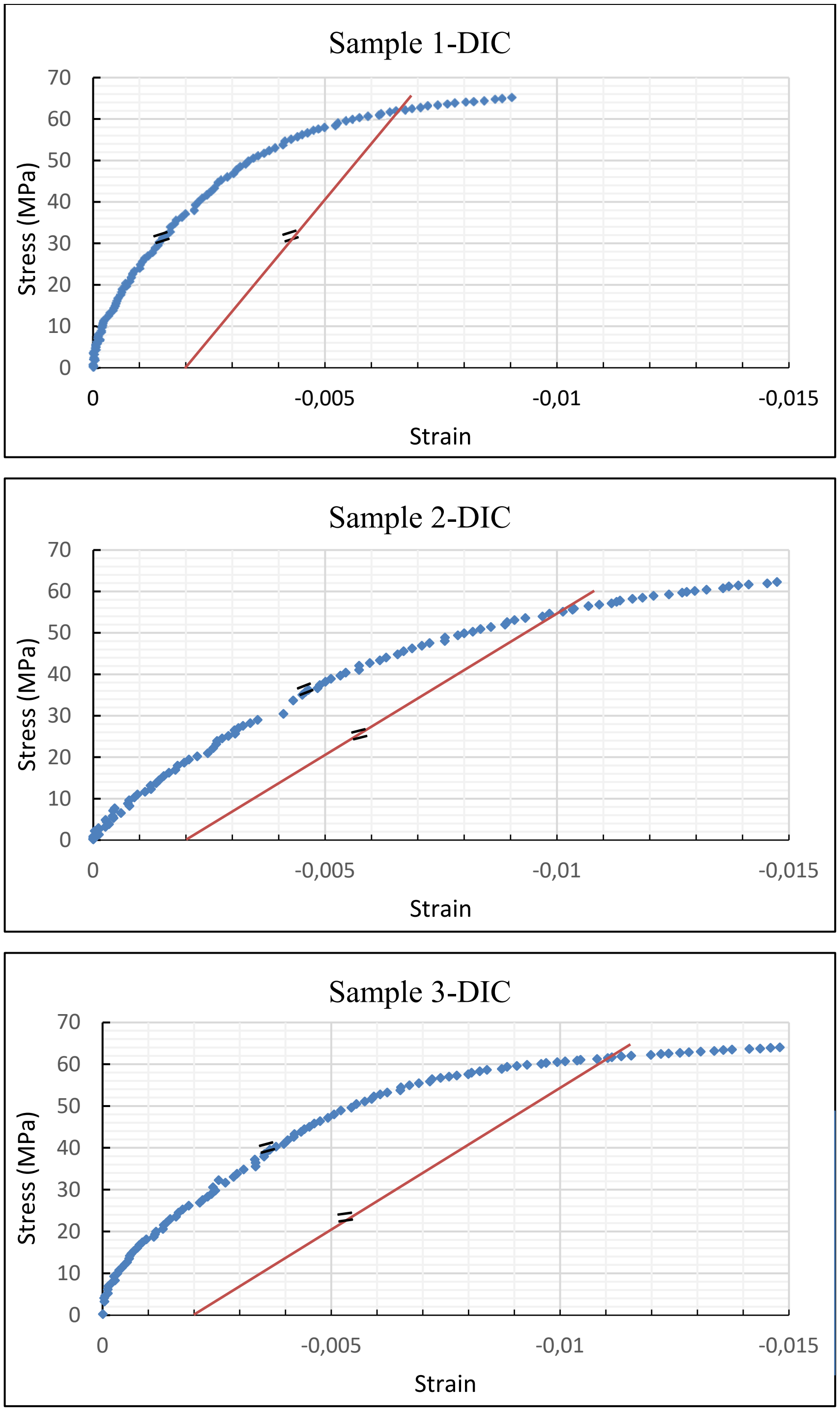

Figure 3-12 Calculation of the apparent yield stress based on stress-strain curves obtained from the DIC for three samples

Table 3-3 Apparent yield point for all samples and methods

Methods	Samples	Stress (MPa)	Strain (MPa)
Machine	Sample 1	61	-0.0262
	Sample 2	55	-0.0212
	Sample 3	59	-0.0237
Extensometer	Sample 1	60	-0.0108
	Sample 2	51	-0.0105
	Sample 3	55	-0.0110
DIC	Sample 1	62	-0.0066
	Sample 2	55	-0.010
	Sample 3	60	-0.011

3.8. Calculation of the linear elastic region length

For assessing the length of linear elastic region around the inflection point in each curve, we assumed 10% of apparent young's modulus value. Meaning that, 10% of the apparent young's modulus value was calculated, and then subtracted from this value. Two points have 10% lower Y' values (slope of the curve) than that of inflection point, one point with lower strain and another one with higher strain value. The stress and strain values of these points are obtained. Then, by subtracting the strain values of these points, the length of the linear elastic region is gained.

3.9. Analysis of the DIC images with OpenDIC and ImageJ applications

In order to analyze the batch of the images taken by 2D-DIC, the OpenDIC application was used to obtain .csv files. Then, the ImageJ application was used to perform the post-processing. In this step, all .csv files were transformed to the displacement fields, the strain fields, and the quality of the measurements.

3.9.1. Processing of DIC images with OpenDIC software

For measuring the strain fields at the surface of the samples, the raw data as the images taken by the DIC were used in OpenDIC application. The principle of this software is relied on comparing images at successive deformed stages to the initial image (Pan et al. 2009b).

In images tab of this software, the initial image (the reference image) and deformed images were chosen. Then, the mask as the measurement zone was calculated and selected. The mask must be a BMP image with zone(s) of interest in white (Vanderesse et al. 2013)(Figure 3-13).

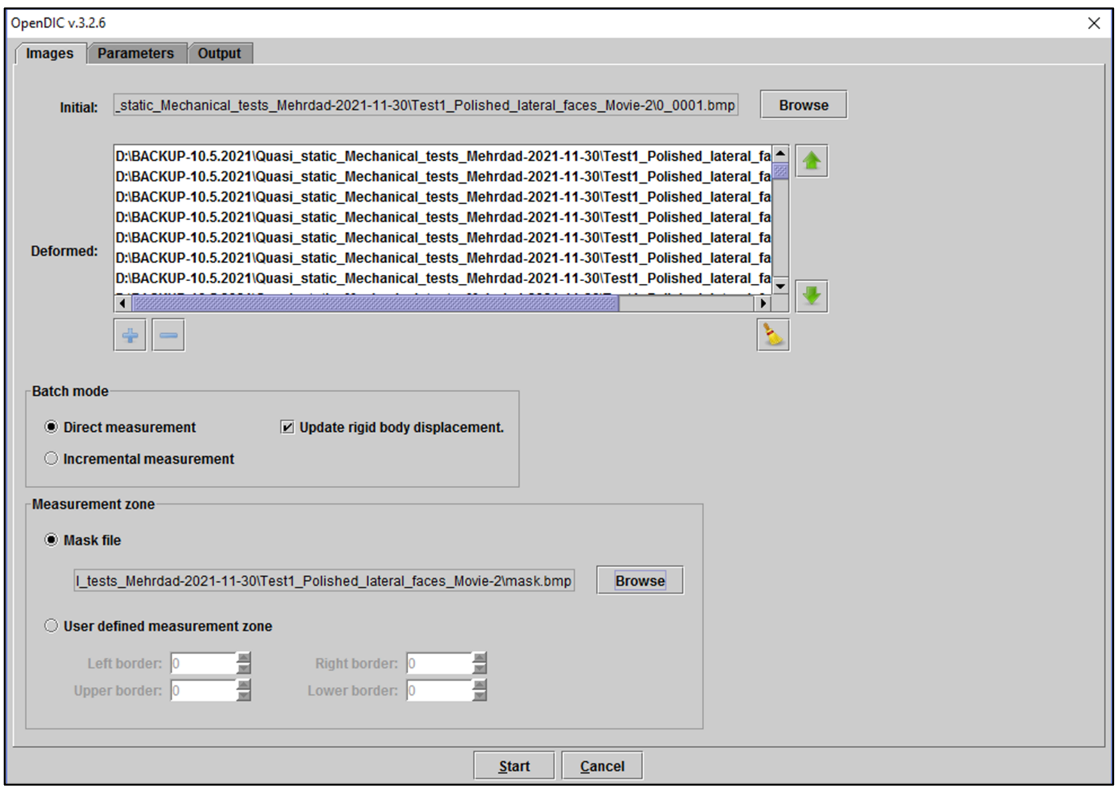

Figure 3-13 Screenshot of the images tab of the OpenDIC software for measuring displacement fields

In the parameters tab of the OpenDIC, the estimation and measurement grids are defined (Figure 3-14). The purpose of the estimation grid is providing a coarse evaluation of the displacement field.

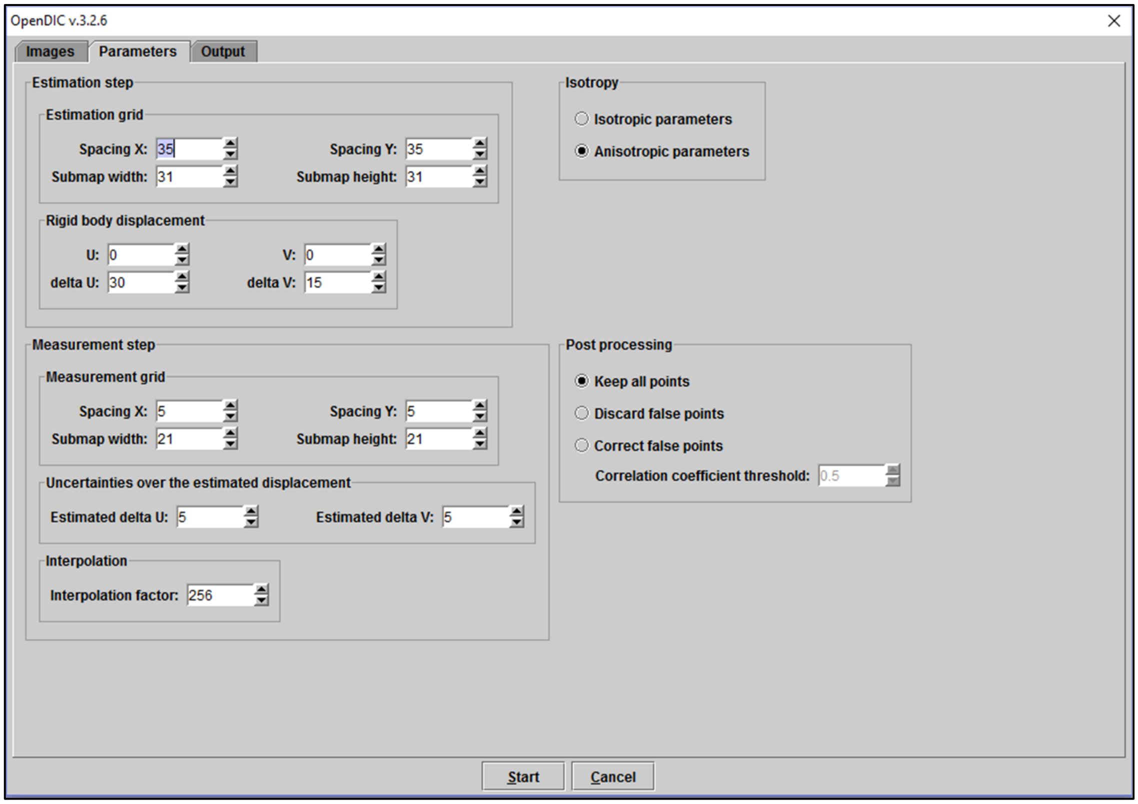

Figure 3-14 Screenshot of the parameters tab of the OpenDIC software for measuring displacement fields

In the output tab, the user chooses what is needed to be saved or displayed. I chose the format of the output files to be as .csv, and checked the box of log file (Figure 3-15).

When the strain measurement was completed by OpenDIC application, a .log file and a serie of .csv files were created in the output folder. The log file presents all the parameters used for DIC calculation (i.e. grid spacing, submaps); meaning that if the program faces any problems, it is possible to resolve the issue by looking at the log file and change the related parameters and run the program again.

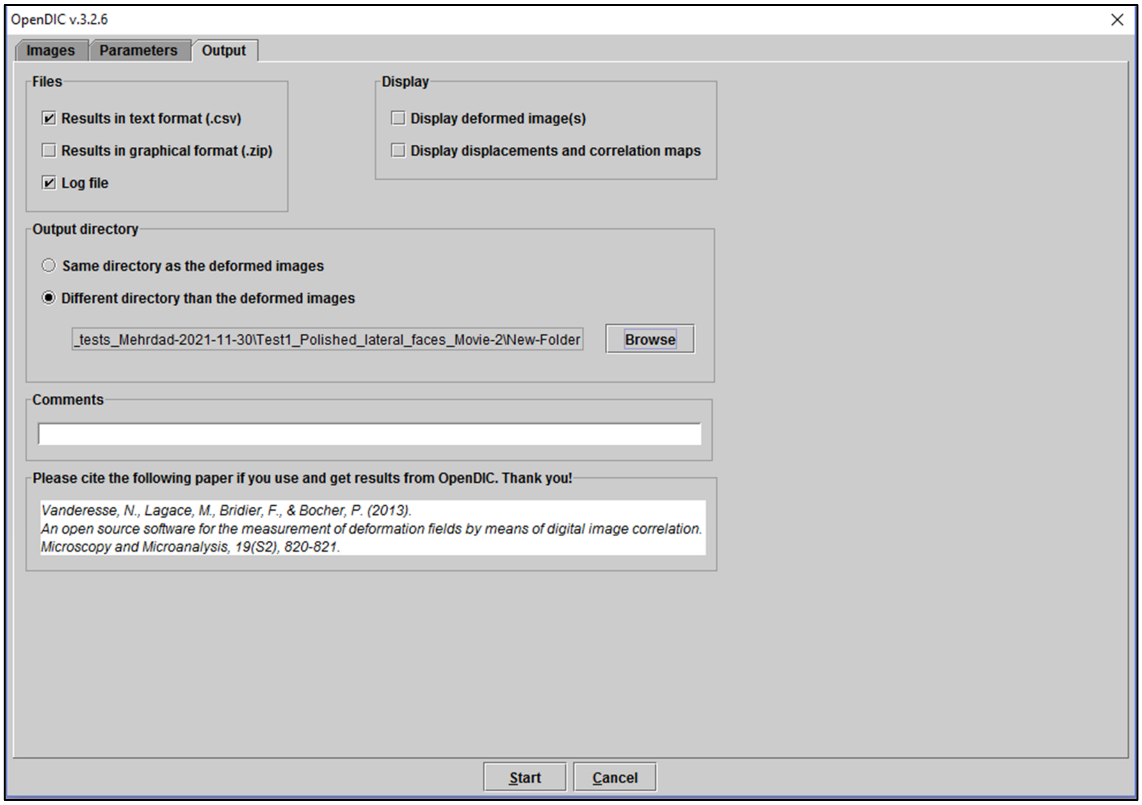

Figure 3-15 Screenshot of the output tab of the OpenDIC software for measuring displacement fields

3.9.2. Post-processing of DIC images with ImageJ application

For analyzing the .csv files, the ImageJ application was used. Two files, .log and .csv, were used in the OpenDICBatchPostProcessing section of the ImageJ to calculate the strain fields (epsxx.tif, epsxy.tif, and epsyy.tif), the displacement fields (u.tif and v.tif), and the quality measurement index (zncc.tif). The zncc.tif file is the zero-normalized correlation coefficient value, which quantifies the correlation quality between the two images. It is comprised between -1 and 1, but usually takes values over 0.8 if the match, hence the measurement, is correct.

3.9.3. Local strain vs. macro strain graphs

In sample's face, the strain value for each horizontal floor (perpendicular to the load direction) is different. Therefore, in order to analyze the strain level in each floor, the average strain value over vertical struts without considering the black empty holes was assessed. To do that the strain field file (epsxx.tif) was opened by the ImageJ application. The epsxx was used since in the images taken by DIC, the compression load is applied horizontally, and not vertically to consider epsyy. When the strain field file was opened, the brightness-contrast was set to -0.10-0.00. The minimum value was set to -0.10 since we had 1 mm compressive displacement over the average height of the samples, 14.70 mm. According to $\frac{-1}{14.7} = -0.068$, the rounded value -0.1 was considered. Then, one vertical rectangle was drawn over each vertical strut, and by selecting the zprofile tab and vertical y-axis=Mean, the Mean strain vs. slice graph was created. The is an option to obtain the list of values. This list is extracted and inserted into an excel sheet. This process was performed for all 56 vertical struts (except struts placed on the edge of the sample)(Figure 3-16, Figure 3-17).

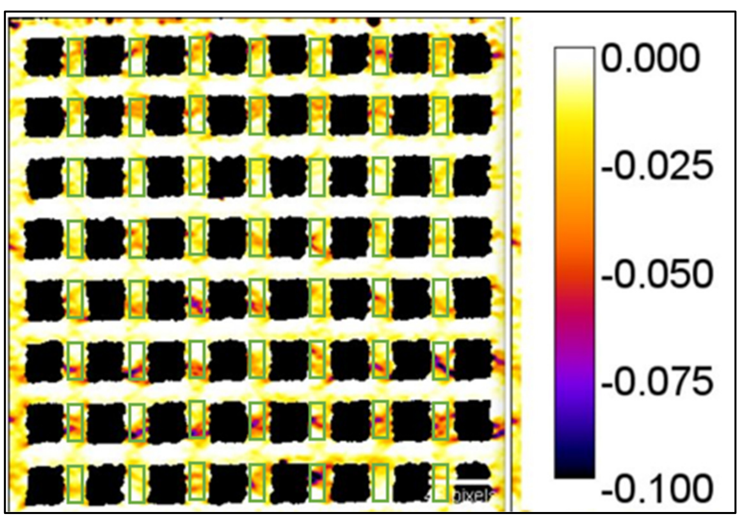

Figure 3-16 Selecting vertical struts to calculate the mean. Strain over them

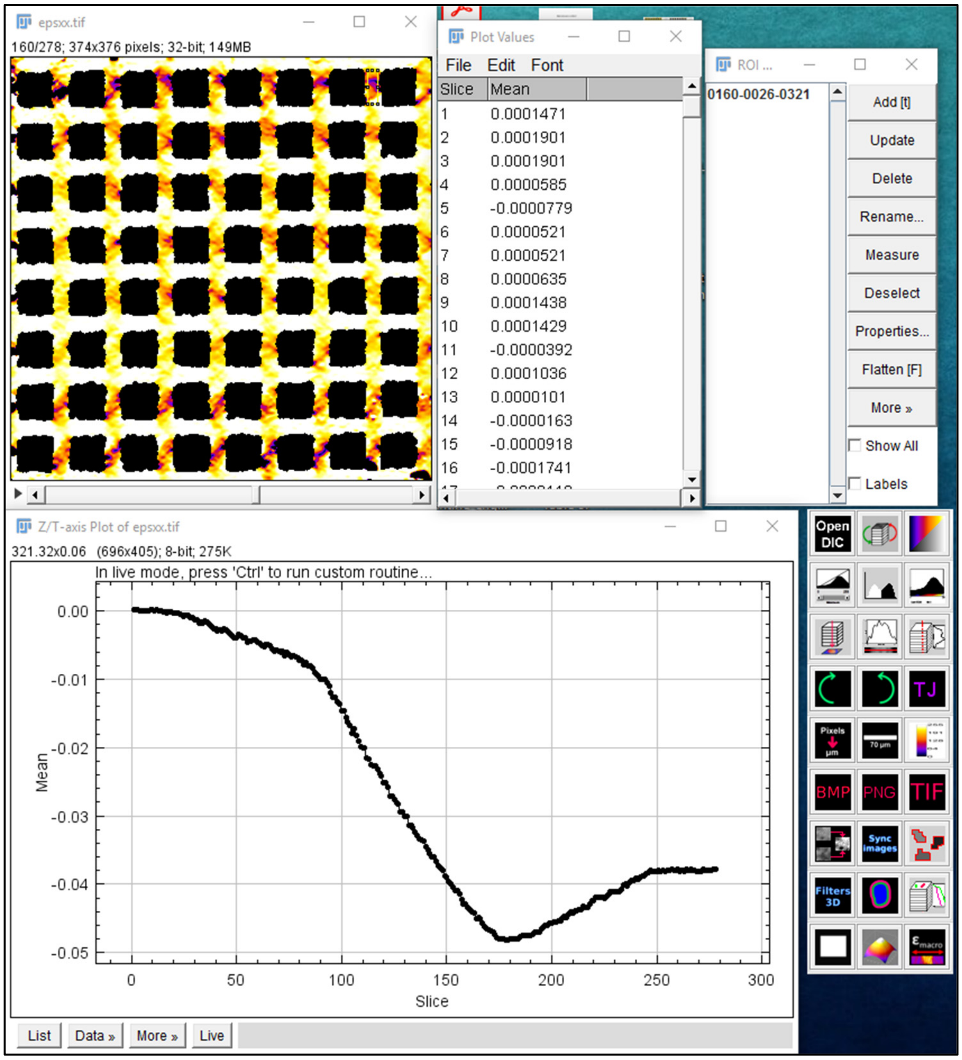

Figure 3-17 mean. Strain versus slice number for all selected vertical struts during the test

After inserting strain value for 7 struts of each floor in the Excel software, these values were averaged. Next, macroscopic strain was calculated.

3.10. Real strain zone vs. artefacts diagnosis

In the strain field file (epsxx.tif), the higher the strain of one point is, the darker it is. This file is created by comparing the first initial image as the reference with other deformed images to the end of the test to find the deformation fields.

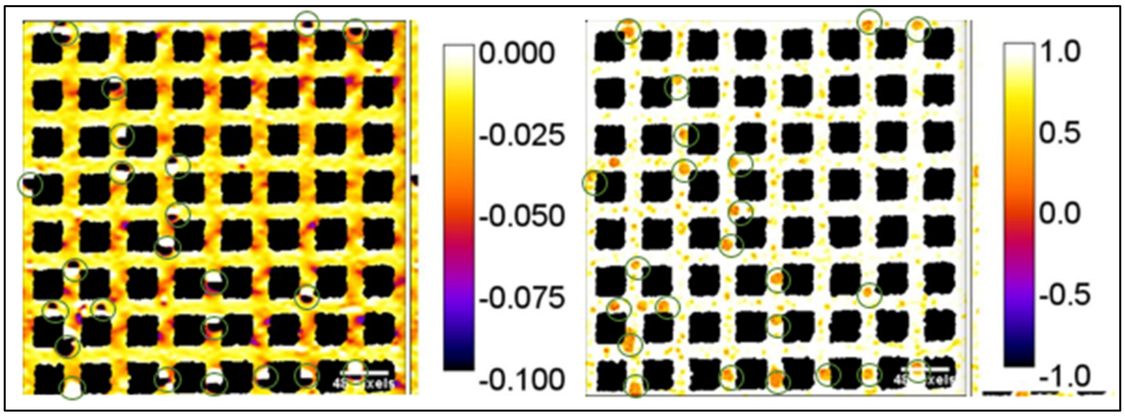

Figure 3-18 strain field (epsxx) and quality index (zncc) for face 2 of sample 1

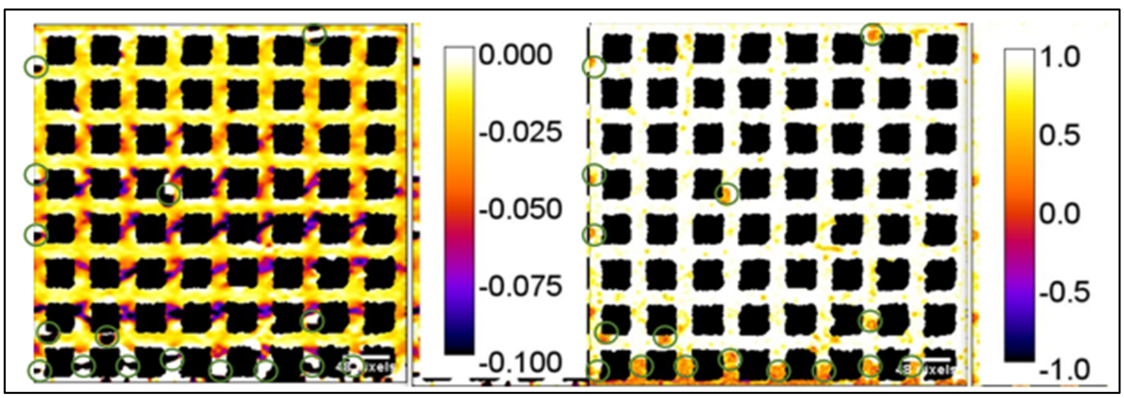

Figure 3-19 strain field (epsxx) and quality index (zncc) for face 2 of sample 2

By Looking at strain field, epsxx, it seems that some specific areas, encircled in green, are high strain areas while looking at epsxx with the consideration of zncc, it shows that these areas have low quality value, from -0.05 to 0, and they are the distortions rather than real strain zones (Figure 3-18, Figure 3-19). The probable reason for this phenomenon is a bad correlation between images and the presence of artefacts, which distort the results. By looking at epsxx image and considering these artefacts, they are characterized by a high and a low strain value joined together.

According to epsxx, these high strain spots can be explained by important uncertainties of measurements during the frame-matching which can be caused by the presence of artifacts. Different assumptions are considered to explain this phenomenon as the artefact:

1. Polished surface reflection or out-plane deformation (Figure 3-20)
2. Paint reflections making high light intensity points on the image (Figure 3-21)

2D-DIC can be used only for in-plane deformations or displacements and does not analyze out-plane deformations.

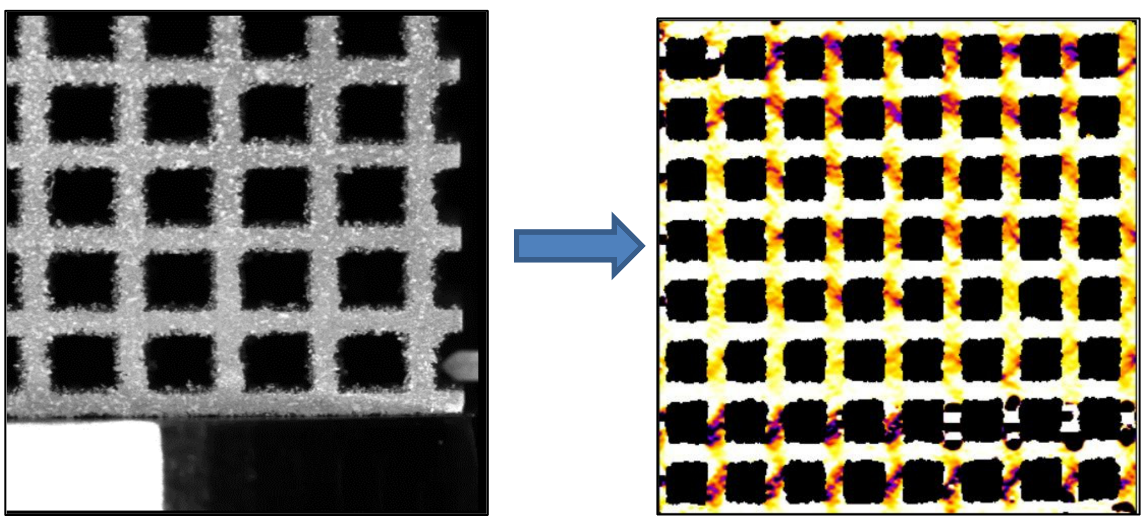

Figure 3-20 Some struts on 2nd floor of sample 3 are deformed. The digital image correlation is misleaded by surface reflection of these polished struts since they have shades with different grades during deformation

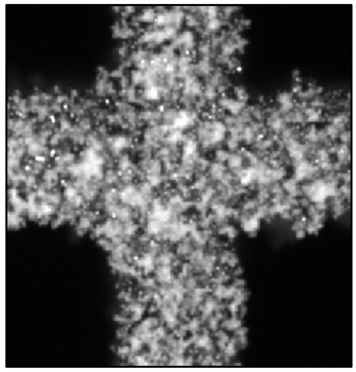

Figure 3-21 A section of sample 2 showing paint reflections

3.11. Analysis of out-plane deformation floor with confocal LEXT microscope

In order to prove that an out-plane deformation happens on lateral face of sample 3, this face was analyzed by confocal LEXT microscope (Figure 3-22). As can be seen in figure 3-23, this phenomenon is identified on the upper second floor of the lateral right-side face of this sample thanks to the topography mode.

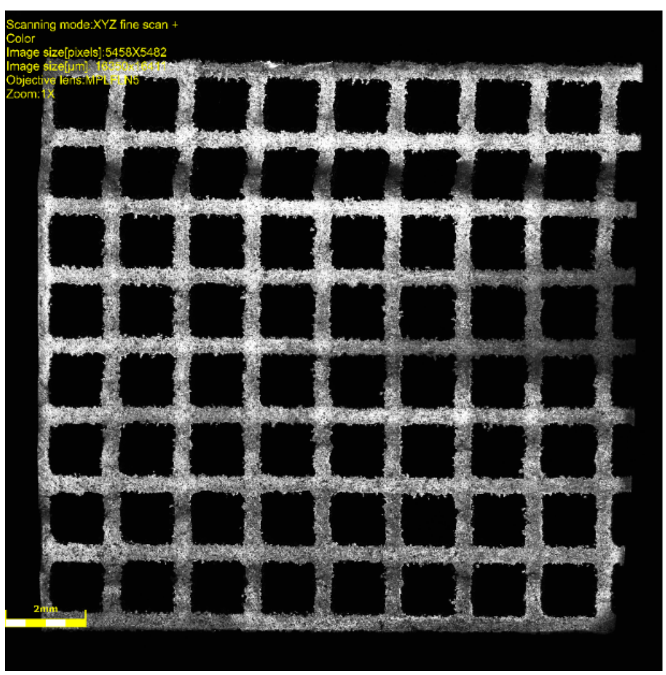

Figure 3-22 Right-side lateral face of sample 3 taken by confocal LEXT microscope

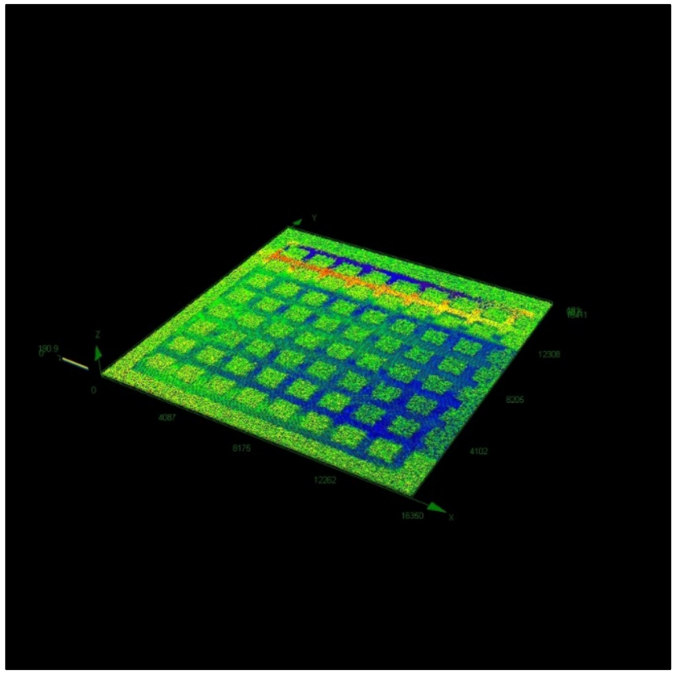

Figure 3-23 Analysis of out-plane deformation in second upper floor in sample 3 with topography mode by confocal LEXT microscope

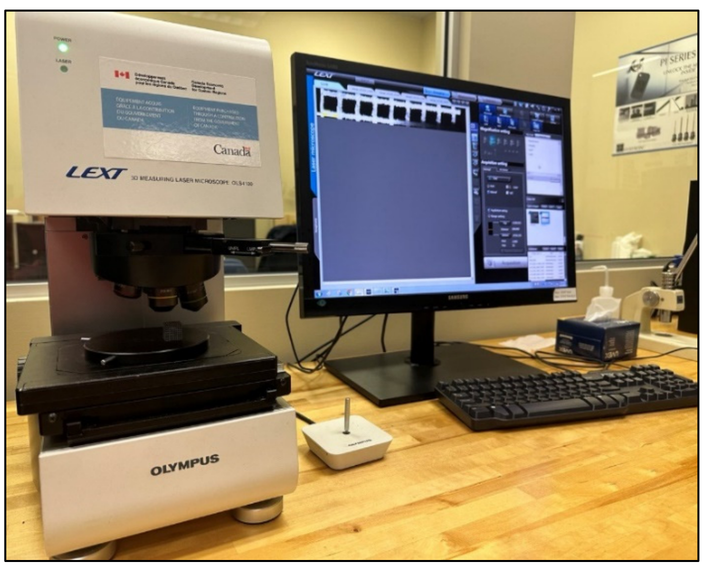

Figure 3-24 Illustration of laser confocal LEXT microscope for out-plane deformation analysis

3.12. Summary

In summary, all steps through which this study is performed are explained. Three specimens were additively manufactured and they got polished on their surfaces. After scanning their lateral polished surfaces by LEXT confocal microscope, the quasi-static compressive tests were performed to analyze their elastic behavior. By using machine and DIC data, the apparent elastic modulus and apparent yield stress were calculated. Then, the postprocessing of the raw data from DIC was done thanks to OpenDIC and ImageJ software.

CHAPTER 4

EXPERIMENTAL RESULTS AND DISCUSSIONS

4.1. Introduction

This chapter is dedicated to the investigation of how three different Ti-6Al-4V porous samples behave in compressive loading condition (1 mm displacement). The crucial parameters like the young's modulus and the elastic region length were analyzed based on stress-strain curves. Thanks to 2D-DIC, the strain map over the face of each sample was investigated to check the strain heterogeneity floor by floor. In addition, the strain maps over three lateral faces of each sample were analyzed.

4.2. Stress-strain curves as obtained by three methods

The stress-strain curves from each method (machine, extensometer and DIC) are obtained for each sample. Each sample shows different deformation behavior but all curves have a similar shape that can be described: a progressive increase of the flow stress with a concave shape, a linear region, a convex region and a linear region corresponding to the unloading of the structure.

The regions of the curve that can be described as linear are similar in the unloading region of the curves, but remarkably different during loading. Sample 1's graph has a concave transition from (0,0) to (-0.012,20), then, the linear region is started. The inflection point is at (-0.017,37) with apparent elastic modulus (E_{ap}) value of 3.4 GPa, and elastic region is finished at apparent yield point (-0.02,48). Regarding sample 2, the graph is started with a concave region (0,0- -0.006,10). Then, it seems that it almost starts its linear region. Inflection point happens around (-0.010,26) with E_{ap} value of 3.56 GPa, and elastic region is finished at (-0.015,40). In addition, sample 3 has a concave transition from (0,0) to (-0.003,6), then, its linear region starts, and inflection point is at (-0.013,36) with E_{ap} value of 3.2 GPa. The upper limit of this region is at (-0.015,42), $\sigma_{y,ap}$. Therefore, among all three sample, third one goes earlier to linear region, while first one has a late transition to this region. For the unloading section, sample 1 and 2 have the same E_{ap} value of 4.3 GPa, while it is lower for sample 3, 3.7 GPa (Figure 4-1). Considering the stress value at apparent yield point, sample 1 is deformed at 61.0 MPa, while this value is 55.0 MPa for sample 2, and 59.0 MPa for sample 3. As a result, Sample 2 has the stress value at apparent yield point with 9.8% lower than that for sample 1 (61.0 MPa).

It can be concluded also that eliminating the surface roughness on two compressed faces of sample 2 by polishing does not resolve the problem of the concave transition at first of the curve which most likely is due to parallelism of compressed faces which must be taken into account in future works.

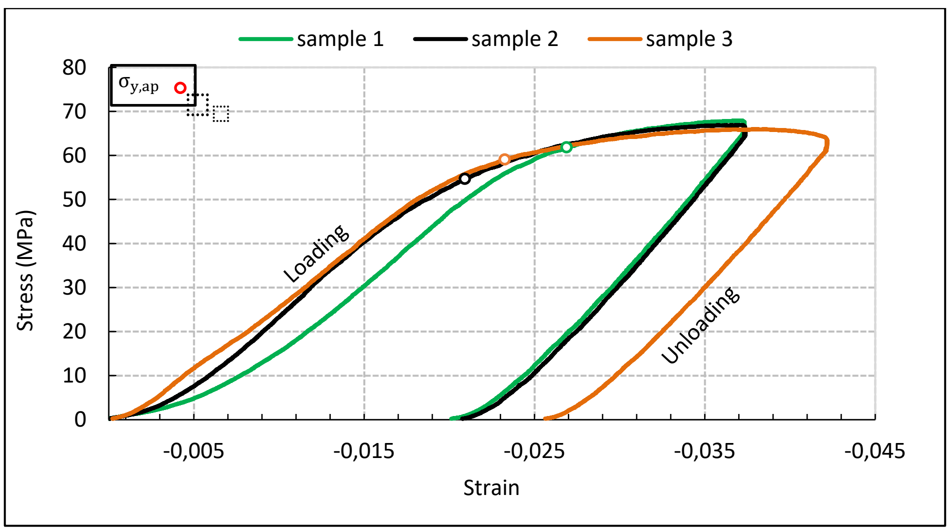

Figure 4-1 Stress-strain curves from machine for three samples

When measured directly on the sample using extensometer, the apparent elastic modulus is higher than the one obtained previously and the measured deformation range is smaller as seen in Figure 4-2. The E_{ap} in loading section varies from 7.6 GPa for sample 1 to 6.2 GPa (18% lower) for sample 2, while sample 3 has an intermediate value of 6.8 GPa. In unloading, this value is approximately the same for three samples, 7.5 GPa. Regarding the stress value for apparent yield point, sample 1 is deformed at 60.0 MPa, while this value is 50.9 MPa for sample 2, and 55.1 MPa for sample 3. Meaning that sample 2 not only has the lowest E_{ap}, but also it is deformed at an apparent yield point with stress value 15.2% lower than that for sample 1.

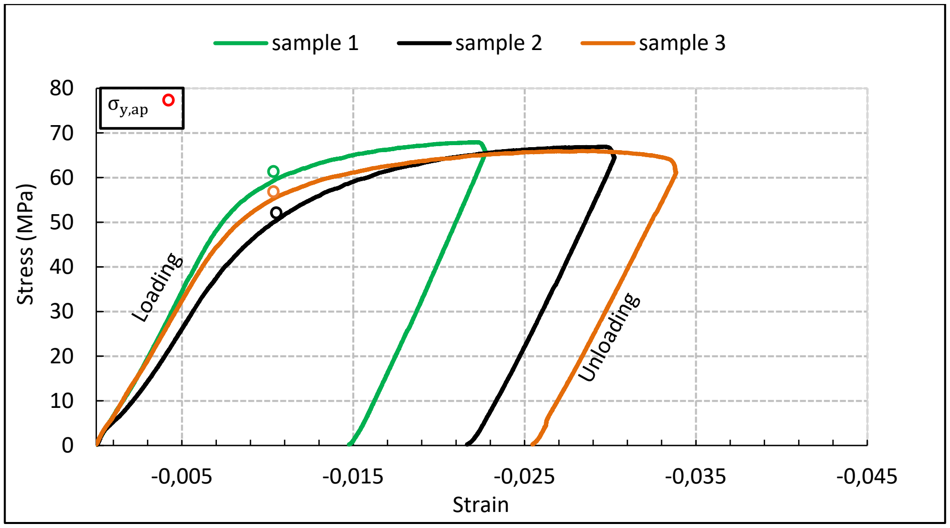

Figure 4-2 Stress-strain curves from extensometer for the three samples

The stress-strain curves obtaining from the digital image correlation (2D-DIC) are not as clean as the ones obtained previously due to not having as much data as those had before (95% less data) (Figure 4-3). The apparent elastic modulus measured follows the same trends as the ones measured with extensometer, but with a larger range of reported values. The E_{ap} value for sample 2 (5.7 GPa) is 22% lower than that for sample 3, 7.3 GPa, while sample 1 culminates at 11.3 GPa. For the unloading section, sample 1 has the E_{ap} value of 9.6 GPa, while it is lower for samples 2 and 3, 7.7 GPa. Last but not least, the stress value at apparent yield point for sample 1 is 61.3 MPa, while it is 55.1 MPa for sample 2, and 59.9 MPa for sample 3. To sum up, sample 2 has the lowest E_{ap}, and it is deformed at 10.1% less stress value for apparent yield point in comparison with this value for sample 1.

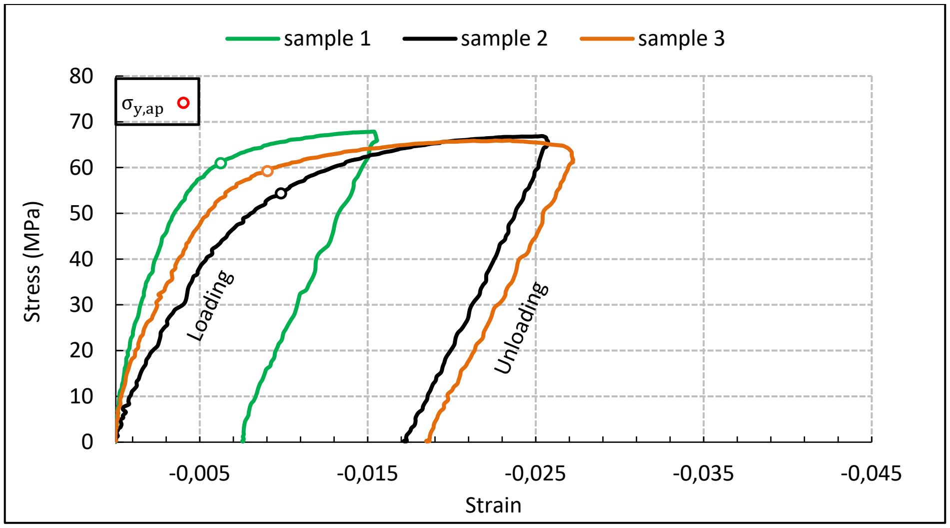

Figure 4-3 Stress-strain curves from DIC for three samples

4.2.1. Length of linear behavior upon loading

There are three different stress-strain curves as well as different linear behaviors for each sample. It should be noted that the length of linear region in all figures is shown as dashed-lines. Considering sample 1, machine presents long length for linear region, 0.0079, while the extensometer shows lower value of 0.0036 (Table 4-1). The DIC by having short linear region length, 0.001, has the lowest value among them (Figure 4-4).

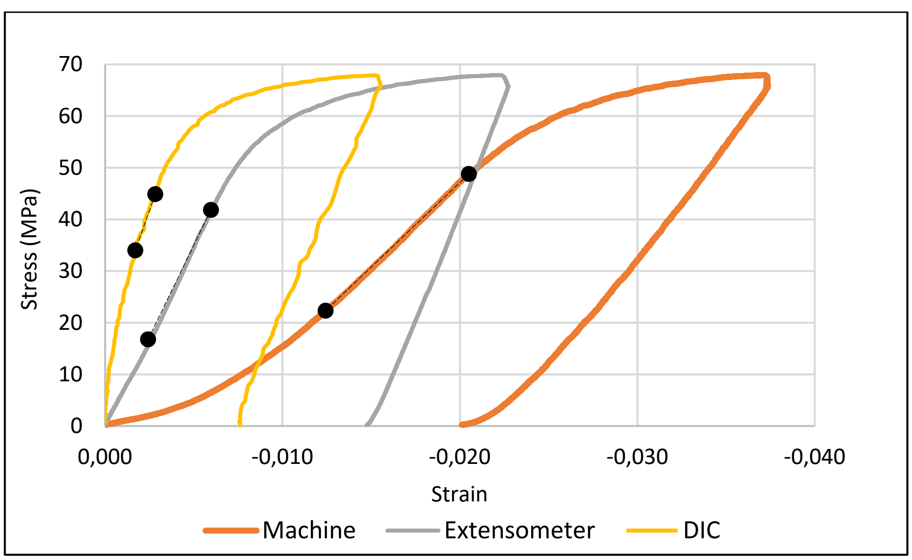

Figure 4-4 Comparing stress-strain curves for three methods on sample 1

For sample 2, machine has long linear region with value 0.0066, whereas this length is shorter for extensometer and DIC, 0.0029 and 0.0013 respectively (Figure 4-5).

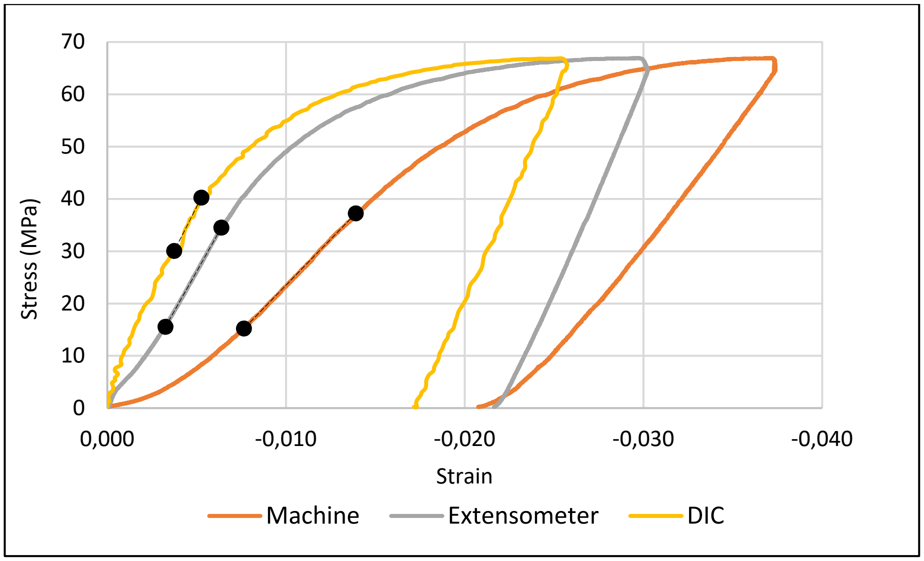

Figure 4-5 Comparing stress-strain curves for three methods on sample 2

For sample 3, the linear region from machine has value of 0.0079. This value for extensometer is 0.0035, and for DIC is 0.0022 (Figure 4-6).

To sum up, the linear region length from machine for three samples is longer than that from extensometer. This trend is the same for extensometer in comparison with DIC. In addition, the upper limit of stress range, where linear region is finished is almost the same for three methods in each sample, while the lower stress limit range is remarkably different. For example, in sample 1, the upper limit for stress range from machine, extensometer, and DIC is 49.3 MPa, 42.4 MPa, and 45.3 MPa respectively, whereas the lower limit is 23.5 MPa, 16.2 MPa, and 34.8 MPa.

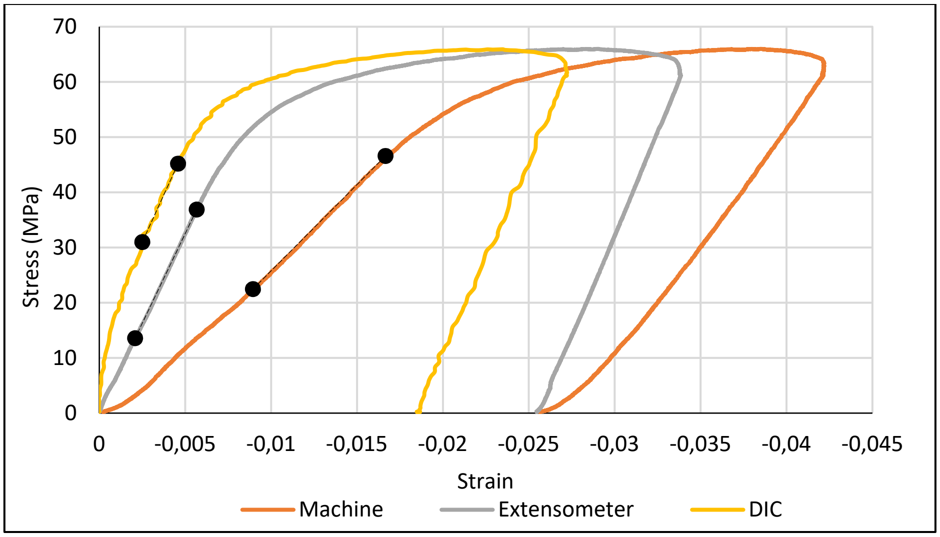

Figure 4-6 Comparing stress-strain curves for three methods on sample 3

Table 4-1 Range of strain for which an apparent elastic behavior is measured and their associated stress ranges for the three samples by three different methods

Samples	Methods	Strain range (linear region length)	Stress range (MPa)
Sample 1	Machine	0.0207-0.0128=0.0079	49.3-23.5=25.8
	Extensometer	0.0061-0.0025=0.0036	42.4-16.2=26.2
	DIC	0.0028-0.0017=0.0010	45.3-34.8=10.5
Sample 2	Machine	0.0143-0.0077=0.0066	38.1-15.4=22.7
	Extensometer	0.0062-0.0033=0.0029	33.8-15.9=17.9
	DIC	0.0054-0.0041=0.0013	40.4-30.5=9.9
Sample 3	Machine	0.0168-0.0089=0.0079	46.5-22.2=24.3
	Extensometer	0.0059-0.0024=0.0035	38.3-15.3=23
	DIC	0.0046-0.0025=0.0022	45.8-29.8=16

Depending on different methods, the strain range (linear region length) and the associated stress range for measured apparent elastic modulus is different. The length values of the stress and the strain ranges differ noticeably from method to method, while these values are approximately close to each other between three samples of each method. Samples 1 and 3 for machine have the same value (0.0079), which is 16% more than that of sample 2, 0.0066. In addition, these two samples for extensometer have almost the same value of 0.0035, which is 17% more than that of second one (0.0029). Furthermore, this value in these samples for DIC is more scattered resulting in 0.001, 0.0022, and 0.0013 respectively (Figure 4-7). It should be noted that these values in all samples for extensometer are approximately 50% less than those for machine. The strain range and it is length in linear region is importance since by considering these limits when designing a customized porous structure; it preserves its elasticity without getting deformed and causing problems for patients.

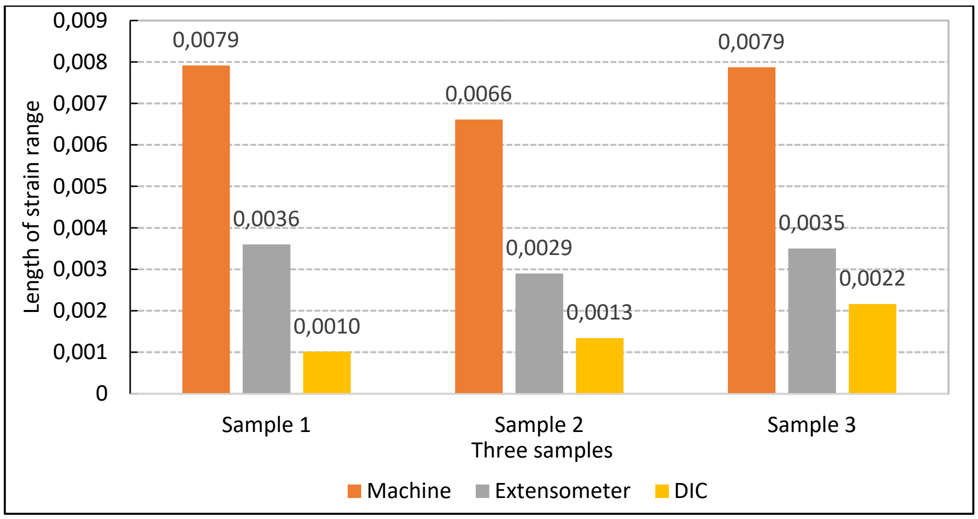

Figure 4-7 Range of strain associated with linear behavior for three samples and three methods

4.3. Local strain maps on three lateral faces of each sample

In order to analyze if the strain distribution and its intensity over each lateral vertical face of each sample is the same or not, they are compared with each other.

4.3.1. Strain maps for sample 1

The heterogeneous nature of the local deformation was documented on sample 1 using three of the lateral faces (the fourth one being used for extensometry). Each face exhibits different strain distribution pattern as displayed in Figure 4-8. In these maps, the vertical strain component (ε_{yy}), parallel to load direction, is used to show strain distribution and quantify it's intensity. The strain range is the same for images, from -0.1 to 0 , that darker spots have higher compressive strains (negative). On face a in sample 1, the lower floors are mostly deformed while strain is homogeneously distributed through vertical struts on face b. On face c, top floors struts undergo more strain than others.

Based on standard deviation (StdDev), faces b and c present almost the same value, 0.0131 and 0.0137, whereas it is lower for face a, 0.0108, which shows that the strain is distributed more heterogeneously on faces b and c. In addition, the average strain (mean) value of faces b and c (-0.019 and -0.020) is higher than that for face a, -0.017. This sheds the light on the fact that the deformation is not the same through three faces.

In Figure 4-8, some spots can be found that look like strain zones. They correspond to distortions rather than real strain zones. Some of them are encircled in orange to provide examples. These spots are characterized by a black and white region next to each other. The main reason of this phenomenon is a local error in the correlation between the frames or the presence of large artifact (e.g. surface reflection or out-plane deformation).

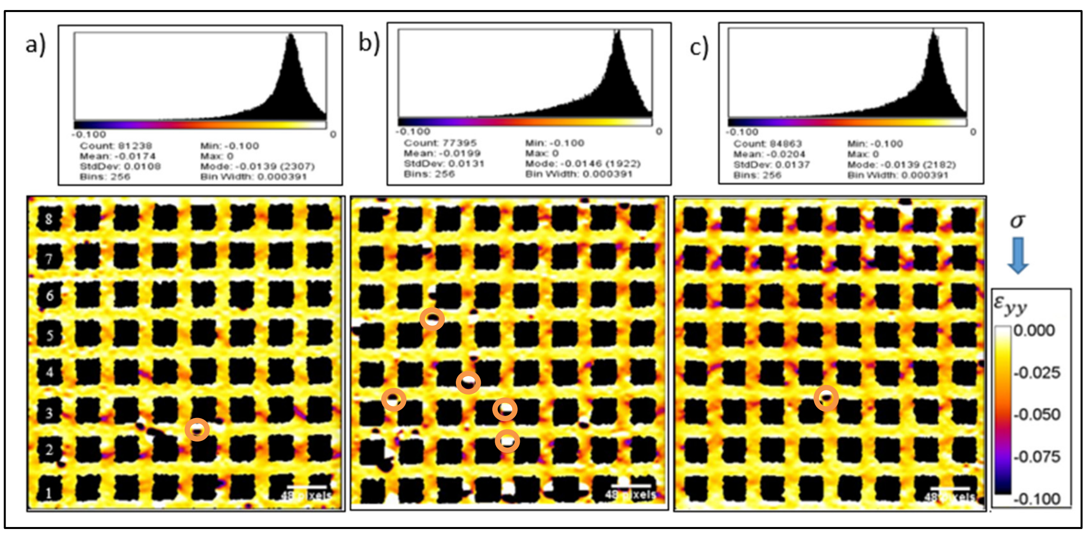

Figure 4-8 Strain maps and histograms of three lateral faces for sample 1. a): left-side face, b): middle face, and c): right-side face. Strain component ε_{yy} aligned with the vertical displacement. Same scale for all maps. Floors from bottom to top (1-8)

4.3.2. Strain maps for sample 2

In faces a and b of sample 2, the strain is mainly concentrated at the lower and middle floors; whereas, the strain is more scattered, and on the top floors through face c (Figure 4-9). Based on StdDev and Mean, unlike face c, faces a and b have high levels of heterogeneities and average strain (mean). Faces a and b have standard deviation values of 0.019 and 0.018, while it is 0.013 for face c. Also, faces a and b have average strain values around -0.022, whereas it is lower for face c, -0.019. It is noteworthy mentioning that it is mainly the vertical struts, parallel to loading direction, which endure the strain. The strain in the vertical struts of a given floor can differ greatly; meaning that few struts on a given floor can concentrate the strain localizations, while the others are not deformed plastically.

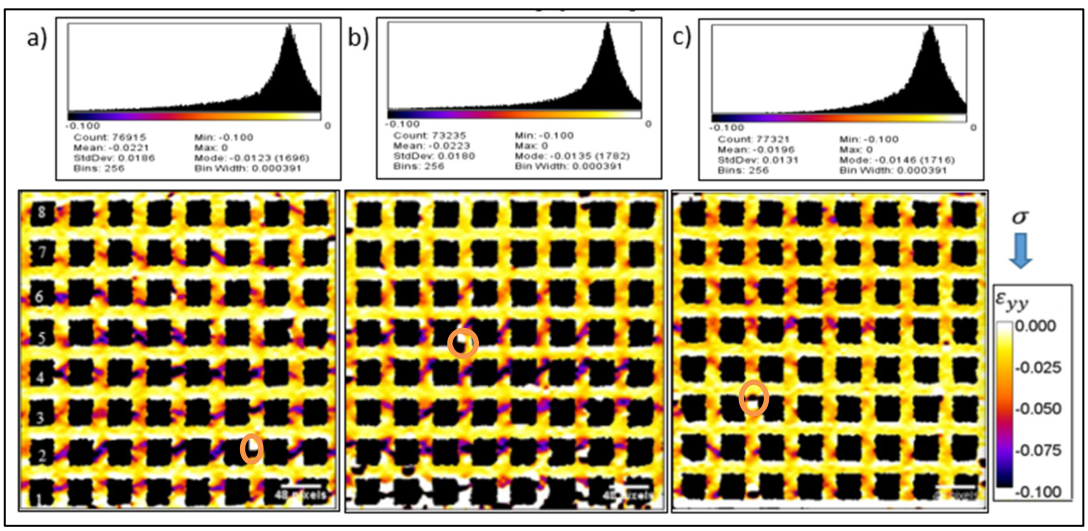

Figure 4-9 Strain maps and histograms of three lateral faces for sample 2. a): left-side face, b): middle face, and c): right-side face. Strain component ε_{yy} aligned with the vertical displacement. Same scale for all maps. Floors from bottom to top (1-8)

4.3.3. Strain maps for sample 3

For sample 3, faces a, b, and c behave differently in terms of strain distribution (Figure 4-10). On face a, not only the strain is noticeably scattered (StdDev of 0.018) but also, it has high average value (-0.024) at some localized spots. Conversely, faces b and c have almost the same values for average strain (0.020) and standard deviation, 0.016. Importantly, the strain is mostly concentrated on floors 2 and 8 in all three faces.

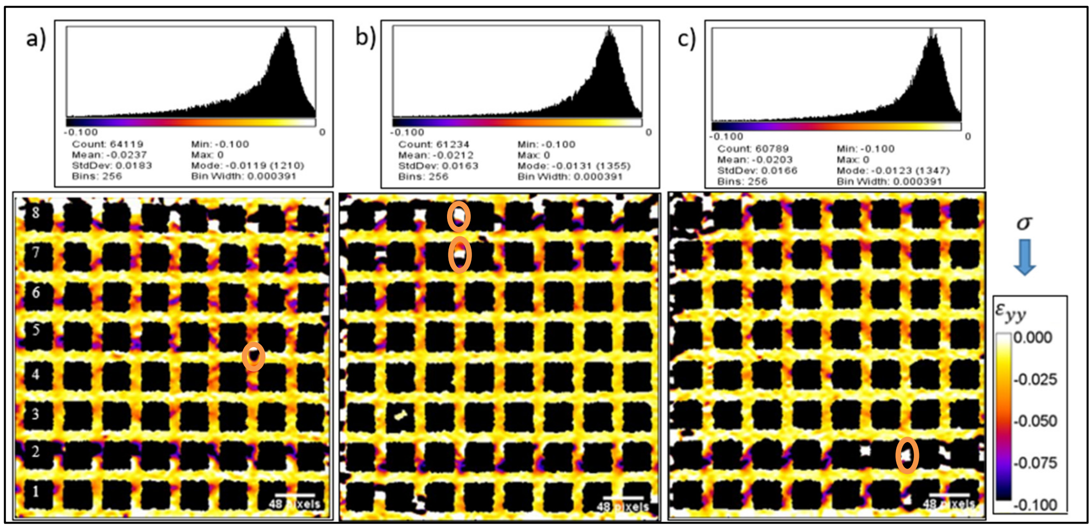

Figure 4-10 Strain maps and histograms of three lateral faces for sample 3. a): left-side face, b): middle face, and c): right-side face. Strain component ε_{yy} aligned with the vertical displacement. Same scale for all maps. Floors from bottom to top (1-8)

Overall, faces b and c in sample 1 present 15% higher average strain as well as standard deviation than those in face a. Differing from sample 1, faces a and b in sample 2 show 14% higher average strain and 28% higher standard deviation than those in face c. Contrary to sample 1 and 2, it is face a in sample 3 that has approximately 12.5% higher average strain and 11% higher standard deviation than those in faces b and c. As a conclusion, the average strain in face a of sample 3 is the highest value, -0.024, among all faces of three samples, while faces b and c in sample 1 declare the lowest value, -0.020. Besides, unlike three faces of sample 1 which show more homogeneous strain distribution with standard deviation 0.013, these faces in sample 2 and 3 have more heterogeneity where severe strain localizations happen in specific floors resulting in the highest standard deviation 0.018.

4.4. Analysis of the deformation distributions

The strain distributions associated with the previous deformation maps displayed in Figs. 9 to 11 are reported together in details (Fig. 12). The maximum intensity of distribution is found at about the same low strain value (-0.0133 $\pm$ 0.010) for all faces of all samples, but the intensities differ significantly: sample 1 presents the highest maximum intensity at 0.028, while sample 3 has the lowest value at 0.018. The faces of a given sample have similar values within a range of +/-0.002. The width of the distribution at half of the peak's maximum are also similar for a given sample, but they differ from one sample to the next: sample 1 still having the lowest value at 0.008 and sample 3 the highest at 0.012. Another interesting feature of the peak shape is how the distribution tends to cross each other at a specific strain value as represented by a blue arrow in fig 12. The transition happens at a low strain value close to -0.02 for sample 1, but it is sample 2 that presents the highest transition value twice larger at -0.04; sample 3 having an intermediate number at -0.03. Analyzing the distribution in the higher strain region by summing the distribution values in the strain range within -0.05 and -0.1 shows that only 2% of the distribution is in that range for sample 1, while it represents 10% for samples 2 and 3. All the above observations show that sample 1 has a more homogeneous deformation behavior than the other two. It also shows that the general behavior of one of the faces is not significantly different from the others, even if some local events on the face can affect the tail of the distribution and reduce the intensity of the maximum.

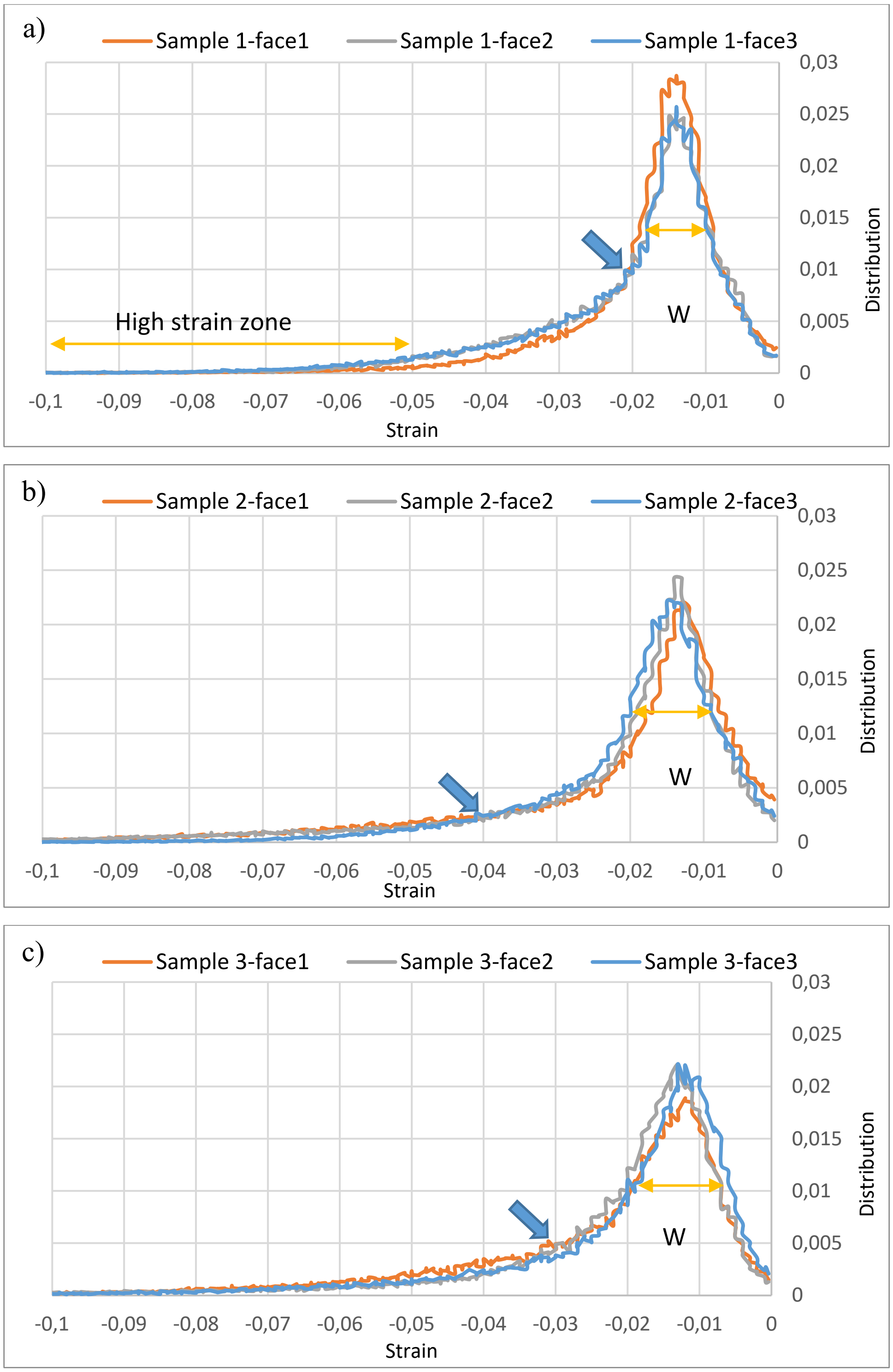

Figure 4-11 Strain distribution of three faces investigated for samples (a) 1, (b) 2, and (c) 3. The data set from 0 to -0.1 strain is divided in 2560 categories.

4.5. Evolution of the local strains for each floor in three samples

To document how the strain varies from one floor to the next during the deformation of the structure, the mean strain of the vertical struts belonging to a given floor were averaged and reported in figures 4-11 to 4-13 against the deformation rate calculated as the X-axis. The results show the complex repartition of the strain in the mesostructure during its deformation. For sample 1, floor 2 reaches the highest strain value at -0.029 for a deformation rate of -0.016 (Figure 4-11). Floor 3 also deform of the same order of magnitude (-0.025), while the other floors have strain values around -0.02 except for floor 6 which deforms less at -0.011. On this face and for this sample, all floors seem to deform similarly at the early stage except floors 1 and 8, which start deforming with delay of -0.012 but their extreme strain values reach rather high values later in the deformation process (higher than 5 and 7).

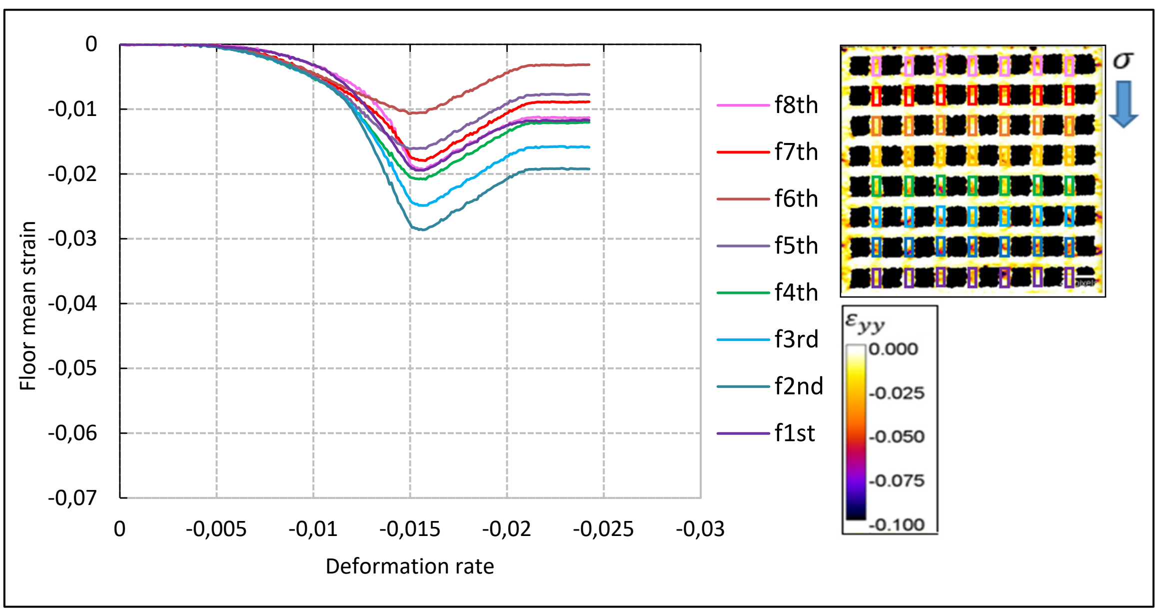

Figure 4-12 Mean strain of vertical struts in each floor vs. deformation rate (bottom: f1st to top: f8th) for sample 1. The position of each floor based on its color is shown on strain map

In the face observed on sample 2, the strain evolution is more scattered as illustrated in (Figure 4-12). Floors 2 and 4 are markedly deformed with extreme strain values of -0.052 and -0.050 respectively. Floor 4 is actually the one deforming more significantly at the early stage of deformation, but it reaches a constant deformation rate at a macro strain of 0.01 while floor 2 sees its deformation rate increase and reaches higher maximum strain value. The extreme value of the other floors is divided between -0.028 and -0.041 with the exception of floor 8, which displays a much lower extreme value at -0.018. Floor 1 is the last one to undergo plastic deformation, but it rapidly localizes deformation after a macro strain of -0.008.

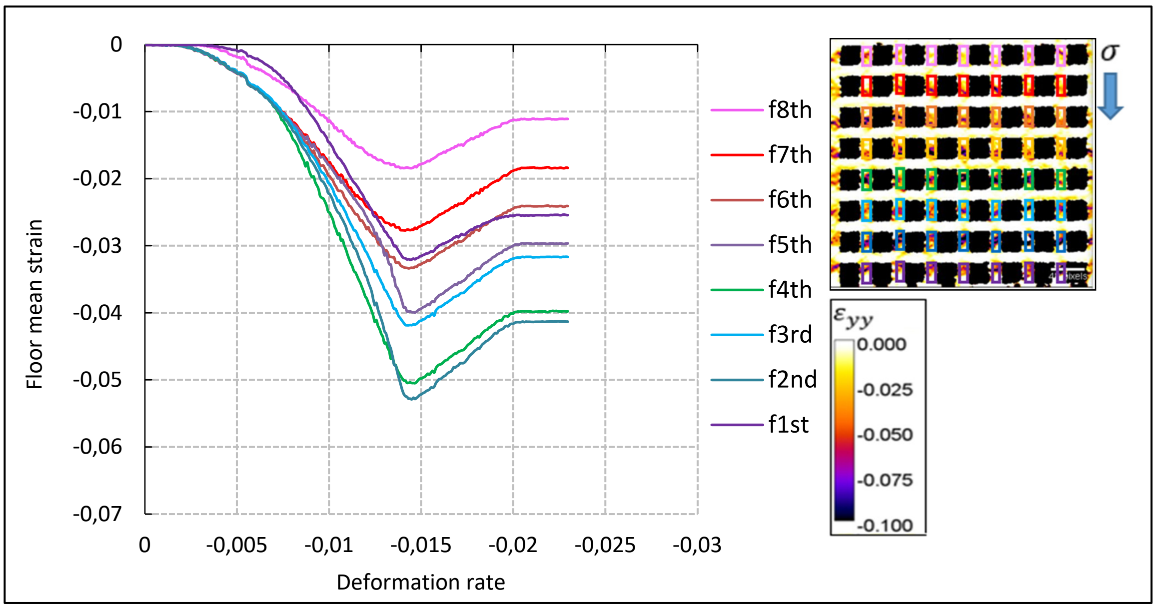

Figure 4-13 Mean strain of vertical struts in each floor vs. deformation rate (bottom: f1st to top: f8th) for sample 2

The strain history is distributed more heterogeneously among the floors on the face documented in sample 3 (Figure 4-13). Floor 2 notably presents the highest strain value at -0.06 for macro strain of -0.019. Floors 1 and 8 are deformed with strain values of -0.047 and -0.044 respectively. Although floor 8 has a significant deformation at early stages of deformation, it deforms with a steady rate at a macro strain of around -0.01. Unlike floor 8, floor 1 reaches a higher extreme strain value after a slow progressive deformation rate increase. The other floors have the strain values diving between -0.018 and -0.03.

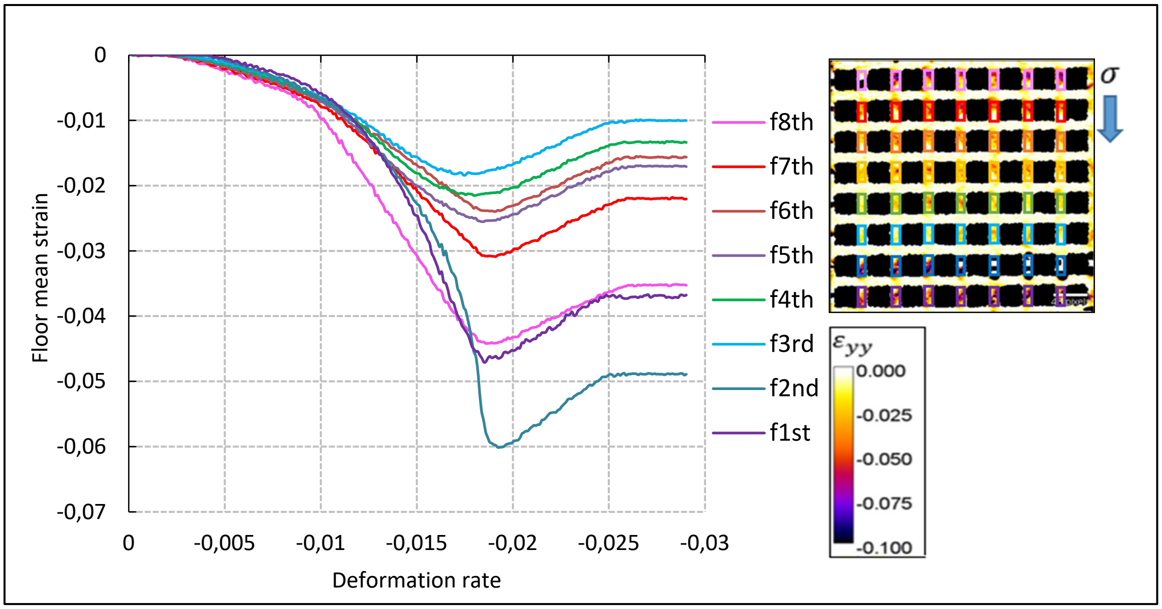

Figure 4-14 Mean strain of vertical struts in each floor vs. deformation rate (bottom: f1st to top: f8th) for sample 3

Overall, for the three samples, floor 2 has the highest strain value among floors. and floor 8 the one undergoing the least localization. Some floors start their deformation earlier than other ones, but their early behavior can not predict the future of the mesostructure.

4.6. Summary

In summary, the local strain condition in each face as well as each floor of these mesostructures is analyzed. The analysis of strain localization in three faces of each sample is performed by using strain maps and histograms. To clarify where local strain happens in floors of each sample, floor mean strain-macro strain curves are used. Sample 1 presents the most uniform strain distribution with the lowest average strain (-0.019), and the lowest value for standard deviation (0.013). Sample 2 has average strain -0.021 and average standard deviation 0.0166. Last but not least, Sample 3 has the highest average strain value, -0.022, and the highest standard deviation of 0.017; meaning that sample 3 has the most heterogeneous strain distribution on it's face.

CHAPTER 5

NUMERICAL MODELING

5.1. Introduction

The purpose of the numerical model is analyzing and estimating the mechanical properties of a real structure or reproducing the experimental data. In my study, an ideal cubic porous structure was created and simulated using ANSYS 2020 R2 and APDL (ANSYS parametric design language), based on the real one. After applying the boundary conditions, the mechanical properties of this model were analyzed and compared to those from experimental tests. It was found that there is a big difference between the results, and the numerical result overestimated the mechanical properties. This is because of the fact that the manufactured porous structures have some inherent geometrical irregularities which results in lowering the mechanical properties of the structure (e.g. elastic modulus, reaction force, and yield stress). These geometrical irregularities consisting of strut diameter variation in cross-section through strut length, inclination in struts, pores in struts, and not completely fused struts. Therefore, beside the ideal model (numerical model 1), three models with considering three types of irregularities separately, and one model with the combination of two irregularities were implemented in the ideal model; Numerical model 2 was considered as the model including random values for outer diameter of each strut. Numerical model 3 had random displacement values in the joint positions of struts, where four struts meet, considering as strut inclination. Numerical model 4 was considered to have random values for young's modulus for each strut, and in numerical model 5, the combination of random outer diameter and random joint position was considered. Finally, the stress-strain curves and apparent young's modulus were compared with experimental data.

5.2. Ideal numerical model and its effect on apparent young's modulus

The ideal model was the model in which there was no manufacturing irregularities. This model had 8 pores in each X, Y, and Z direction. In addition, the dimension of this structure in each direction was 14.75 mm as that of the built porous structure. In this model, each strut had the diameter of 0.6 mm, and each square pore had the dimension of 1.17*1.17mm (Figure 5-1). The material was modeled as linear elastic since the criteria in this study was analyzing the apparent young's modulus. An elastic modulus of E=120GPa and a poisson's ratio of v=0.3 were used. Struts were modeled as in (Gonzalez and Nuno 2016), using straight lines and meshed with 3-node Timoshenko beam elements with circular cross-section and quadratic displacement behavior, PIPE288 element, which is suitable for slender to moderately thick pipe structures. Regarding the boundary condition, the bottom nodes were fixed in three directions and a vertical displacement within the range of 0.001 and 0.09 was applied on all upper nodes. For defining the displacement range, it was possible to consider 0 to 1mm based on the experiment, but since the purpose was analyzing the young's modulus in this study, it was essential to stay in the elastic region. Indeed, the strain range in the elastic region for sample 1 and extensometer based on table 4-1 was considered. Based on this table, the strain range is between 0.0025 and 0.0061. By knowing the strain formula (5.1), the initial length 14.75mm and the upper strain range limit, 0.0061, the upper limit for displacement (0.09mm) was calculated.

$$\varepsilon = \frac{displacement\ (final\ length - initial\ length)}{initial\ length} \tag{5.1}$$

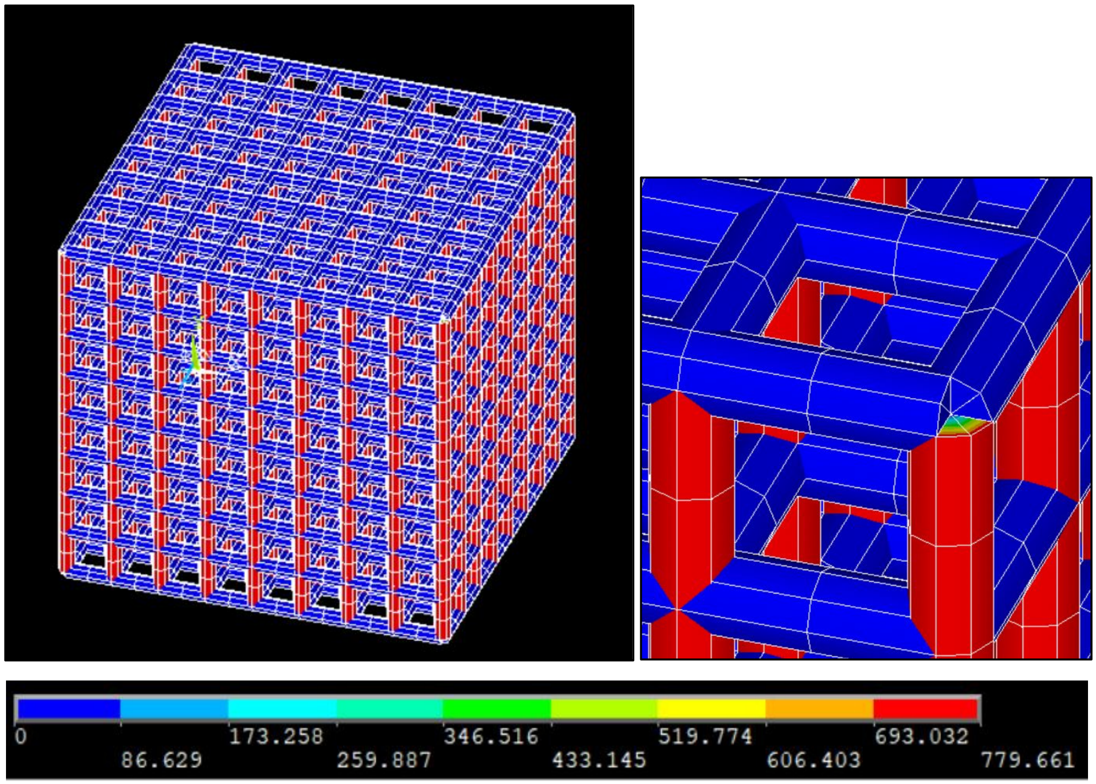

Figure 5-1 Stress distribution within struts for numerical model 1

After simulating the ideal model for each different displacement value from 0.001 mm to 0.09mm, the reaction force was obtained from the software. The stress, strain, and apparent young's modulus were calculated by having the reaction force, apparent area, and initial length of the structure (Table 5-1). Based on this table, the average young's modulus is 12.11GPa with standard deviation of 0.026.

$$\sigma = \frac{F}{A} \tag{5.2}$$

$$\sigma = Eap \times \varepsilon \tag{5.3}$$

Table 5-1 Calculated reaction force, stress, strain and apparent young's modulus for different displacements in linear region for numerical model 1

d (mm)	F (N)	A (mm2)	Stress (MPa)	Strain	Eap (GPa)
0.001	180	217.56	0.8274	0.0001	12.2035
0.003	535.68	217.56	2.4622	0.0002	12.1059
0.005	892.8	217.56	4.1037	0.0003	12.1059
0.007	1249	217.56	4.1037	0.0005	12.0970
0.009	1607	217.56	7.3865	0.0006	12.1056
0.01	1785.6	217.56	8.2074	0.0007	12.1059
0.03	5356.8	217.56	24.6222	0.0020	12.1059
0.05	8928	217.56	41.0370	0.0034	12.1059
0.07	12499	217.56	57.4508	0.0047	12.1057
0.09	16070	217.56	73.8647	0.0061	12.1056

5.3. Numerical model with implementing geometrical irregularities

Based on previous studies, especially the one by Fernando (Gonzalez and Nuno 2016), different strategies were considered to apply manufacturing irregularities in the numerical model to reach the mechanical properties (young's modulus) close to those of experimental tests.

5.3.1. Numerical model with random distribution of outer diameter for each strut and it's effect on apparent young's modulus

Since each strut has multiple cross sections due to the manufacturing irregularities, a code was developed to consider random outer diameter for each strut being able to mimic this shape of the strut. Based on this code, a random value between 0.45mm and 0.6mm was selected and associated with each strut. Based on the study performed by (Vanderesse et al. 2016), the thickness distribution over the strut length is more likely to be smaller than the normal value 500 µm (Figure 5-2). For the sample S500-P1000, which has as the same scale of strut to pore size as my structure (S600-P1170), the strut thickness distribution is localized mostly between

350 to 500 µm. This is why a distribution in the range of 0.45-0.6mm was considered (Figure 5-3).

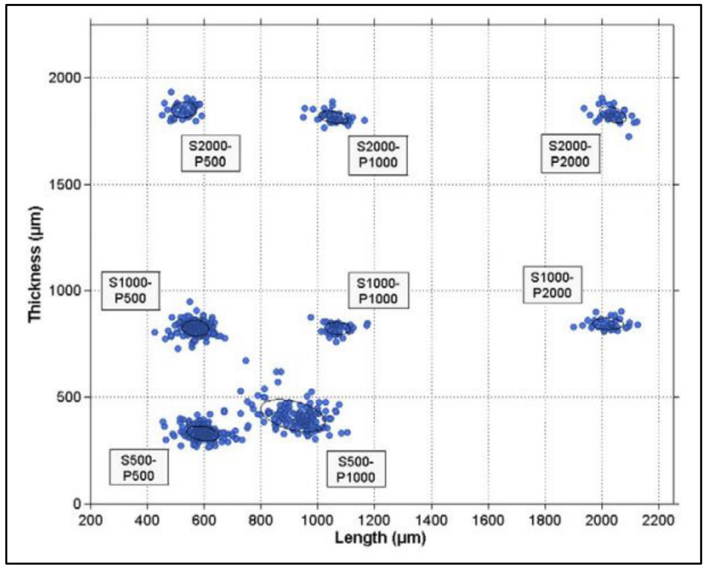

Figure 5-2 Thickness vs. length distribution in face 5 for all porous structures
Taken from Vanderesse et al. (2016)

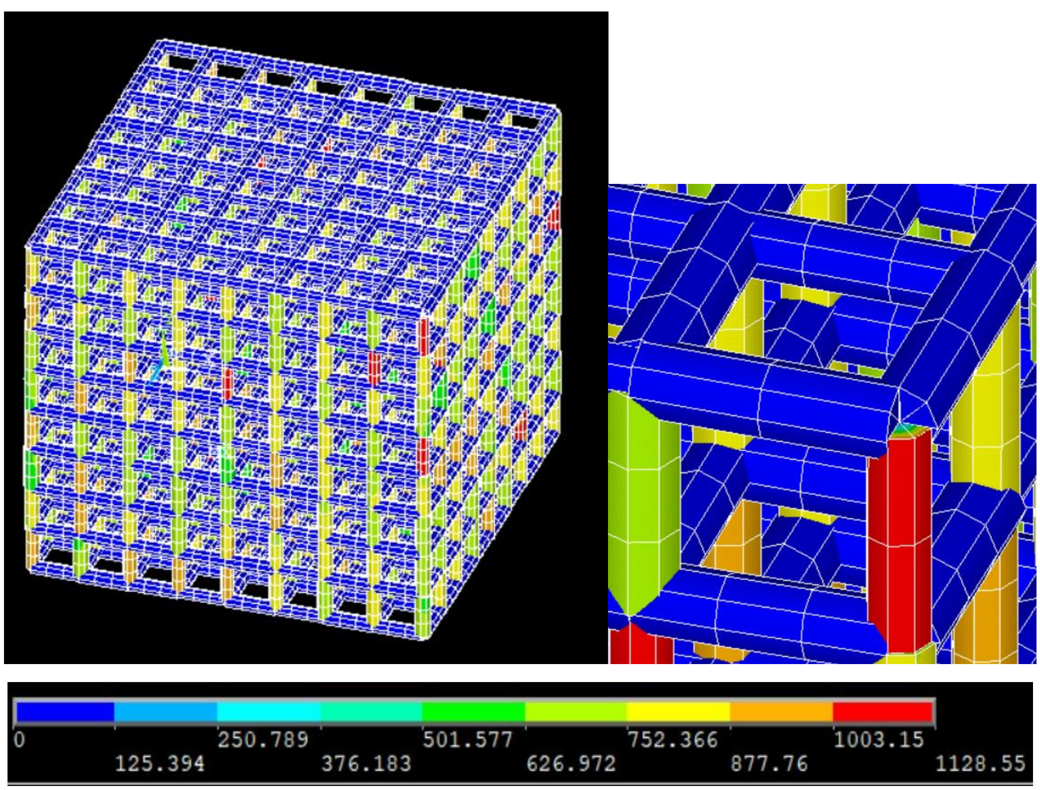

Figure 5-3 Stress distribution within struts for numerical model 2

Table 5-2 Calculated reaction force, stress, strain and apparent young's modulus for different displacements in linear region for numerical model 2

d (mm)	F (N)	A (mm2)	Stress (MPa)	Strain	Eap (Gpa)
0.001	134.58	217.56	0.6186	0.0001	9.1242
0.003	402.45	217.56	1.8498	0.0002	9.0950
0.005	670.22	217.56	3.0806	0.0003	9.0878
0.007	947.02	217.56	4.3529	0.0005	9.1722
0.009	1212.1	217.56	5.5713	0.0006	9.1308
0.01	1332.2	217.56	6.1234	0.0007	9.0320
0.03	4061.5	217.56	18.6684	0.0020	9.1786
0.05	6746.3	217.56	31.0089	0.0034	9.1476
0.07	9526.5	217.56	43.7879	0.0047	9.2267
0.09	12099	217.56	55.6122	0.0061	9.1142

Based on Tables 5-1 and 5-2, the young's modulus of the numerical model 2 is reduced by 25% in comparison to that of ideal model. The average young's modulus is 9.13GPa with standard deviation of 0.05.

5.3.2. Numerical model with random distribution of joint position and it's effect on apparent young's modulus

Since struts are not printed perpendicular to each other and they have inclinations, I considered having a displacement with minimal value, ±0.1, in the joint position of struts (Figure 5-4). It means the intersection of four struts can be displaced in the range of ±0.1 in three directions (X, Y, Z). By this strategy, some struts which have more inclination will face more stress and consequently, more deformation. Regarding the joint position ranges, different values from ±0.05 to ±0.3 were considered, but based on the manufactured structure, ±0.1 was the most realistic value to get selected.

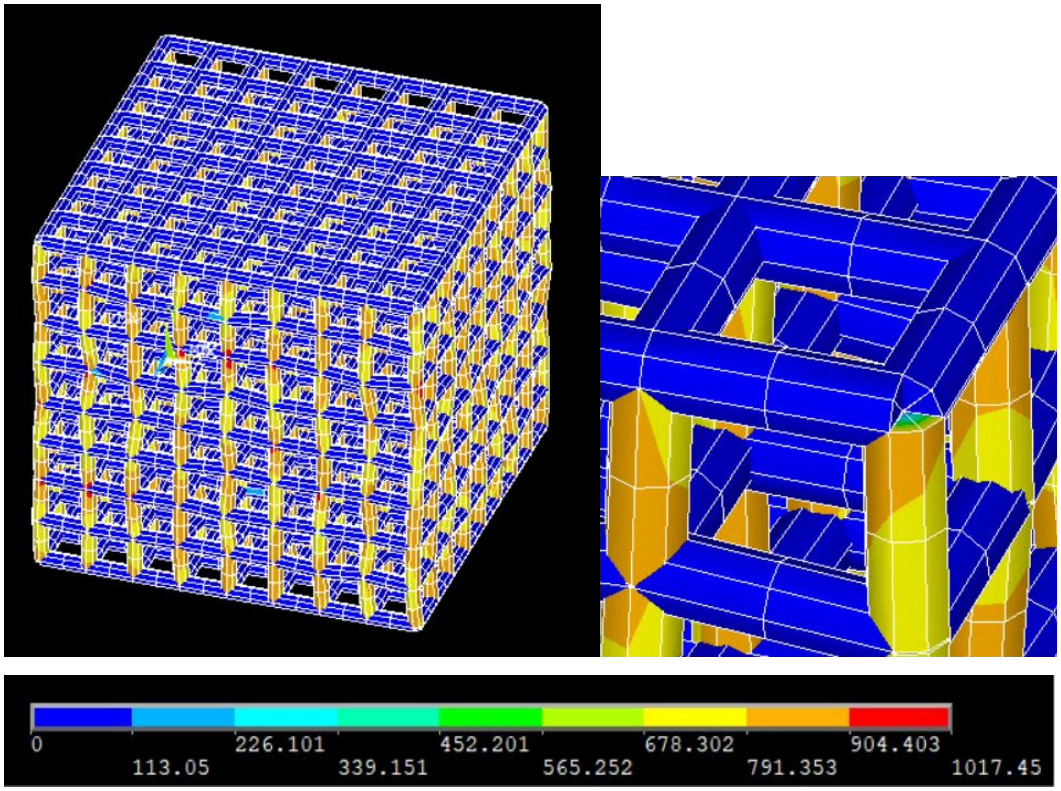

Figure 5-4 Stress distribution within struts for numerical model 3

Based on Table 5-3, the apparent young's modulus of this model is almost the same as the ideal model. Meaning that considering random joint position in model does not have a considerable effect on the elastic properties of the structure. The average young's modulus for this model is 11.99GPa with standard deviation of 0.003.

Table 5-3 Calculated reaction force, stress, strain and apparent young's modulus for different displacements in linear region for numerical model 3

d (mm)	F (N)	A (mm2)	Stress (MPa)	Strain	Eap (GPa)
0.001	176.91	217.56	0.8132	0.0001	11.9940
0.003	530.83	217.56	2.4399	0.0002	11.9963
0.005	884.4	217.56	4.0651	0.0003	11.9920
0.007	1238.2	217.56	5.6913	0.0005	11.9924
0.009	1592.7	217.56	7.3207	0.0006	11.9979
0.01	1769.2	217.56	8.1320	0.0007	11.9947
0.03	5308.7	217.56	24.4011	0.0020	11.9972
0.05	8846.3	217.56	40.6614	0.0034	11.9951
0.07	12385	217.56	56.9268	0.0047	11.9953
0.09	15933	217.56	73.2350	0.0061	12.0024

5.3.3. Numerical model with random distribution of young's modulus for each strut and it's effect on apparent young's modulus

Another strategy to consider manufacturing irregularities in the numerical model was choosing random value of young's modulus for each strut (Figure 5-5). Therefore, a code was developed to consider a random distribution for this value between 100GPa and 120GPa.

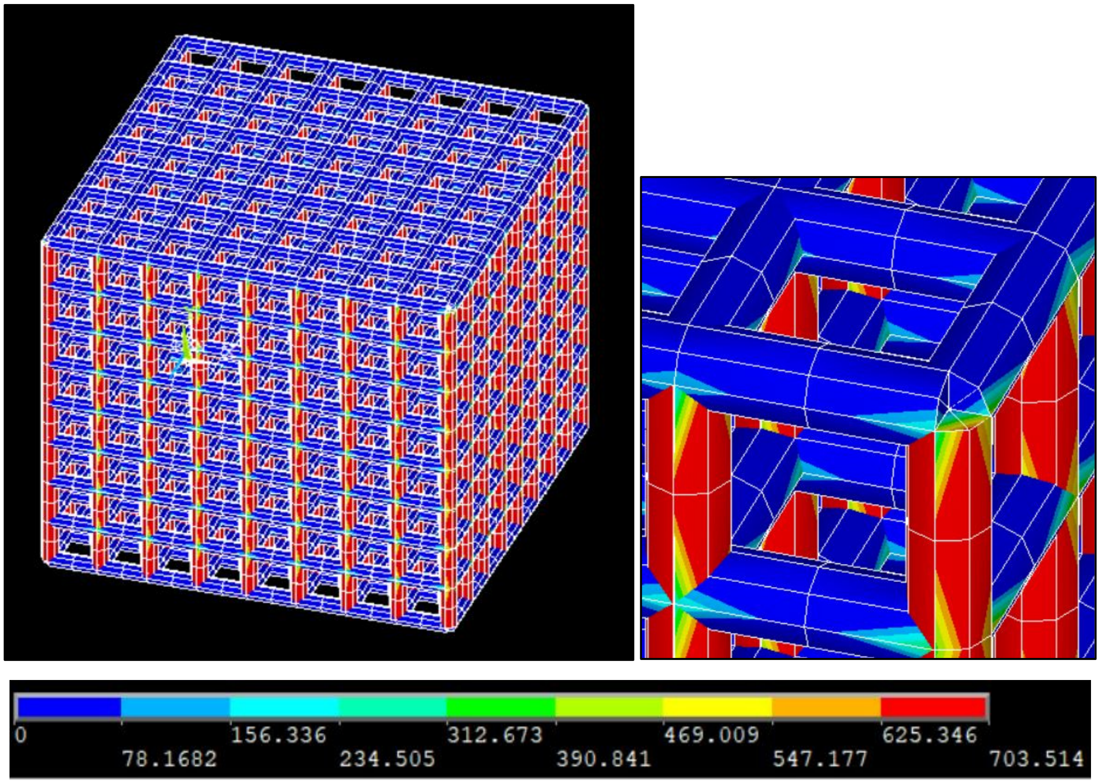

Figure 5-5 Stress distribution within struts for numerical model 4

Based on Table 5-4, young's modulus has more variation (from displacement 0.001mm to 0.09mm) in comparison with those in three previous models. The average young's modulus for this model is 11.76GPa with standard deviation of 0.53.

Table 5-4 Calculated reaction force, stress, strain and apparent young's modulus for different displacements in linear region for numerical model 4

d (mm)	F (N)	A (mm2)	Stress (MPa)	Strain	Eap (GPa)
0.001	174.46	217.56	0.8019	0.0001	11.8279
0.003	509.51	217.56	2.3419	0.0002	11.5145
0.005	866.73	217.56	3.9839	0.0003	11.7524
0.007	1162.4	217.56	5.3429	0.0005	11.2582
0.009	1674	217.56	7.6944	0.0006	12.6103
0.01	1792.4	217.56	8.2386	0.0007	12.1520
0.03	5407.3	217.56	24.8543	0.0020	12.2200
0.05	8941.8	217.56	41.1004	0.0034	12.1246
0.07	11007	217.56	50.5929	0.0047	10.6607
0.09	15241	217.56	70.0542	0.0061	11.4811

5.3.4. Combination of random joint position and random outer diameter and it's effect on apparent young's modulus

This model included both random outer diameter (0.45-0.6mm) and random joint position (+/-0.1mm) to check if their combination can show an apparent young's modulus closer to that from experiment (Figure 5-6).

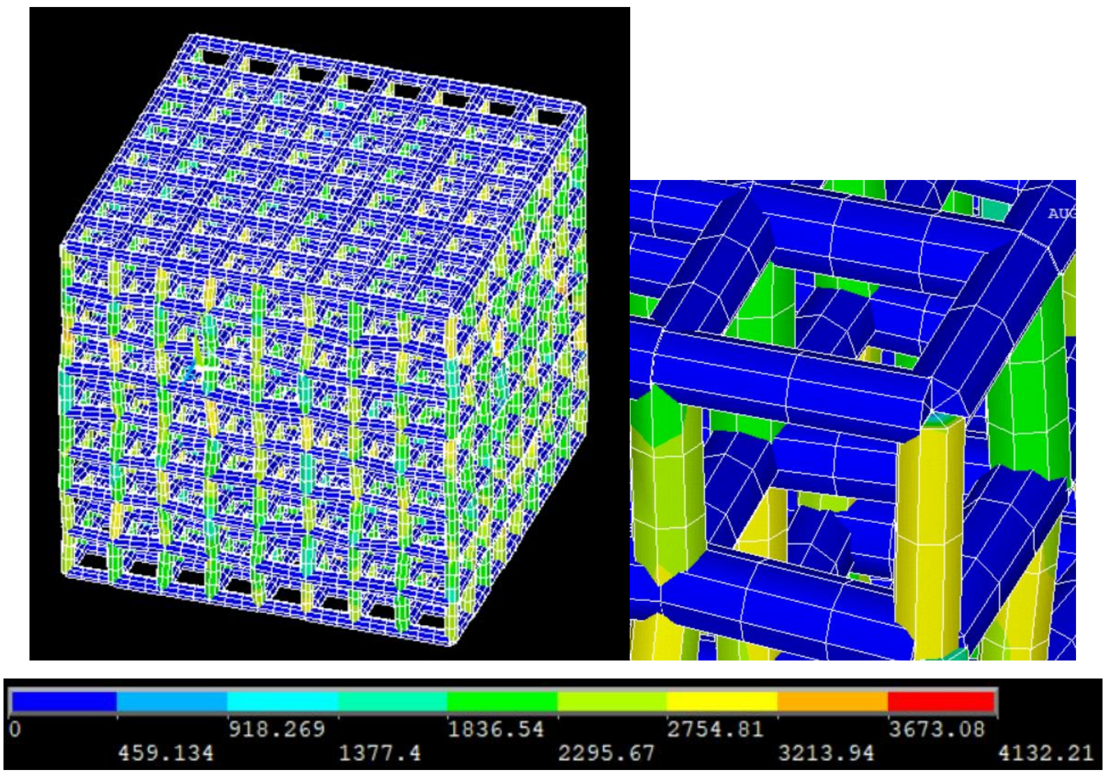

Figure 5-6 Stress distribution within struts for numerical model 5

Based on Table 5-5, the average young's modulus is 9GPa with standard deviation of 0.071.

Table 5-5 Calculated reaction force, stress, strain and apparent young's modulus for different displacements in linear region for numerical model 5

d (mm)	F (N)	A (mm2)	Stress (MPa)	Strain	Eap (GPa)
0.001	131.5	217.56	0.6044	0.0001	8.9154
0.003	399.57	217.56	1.8366	0.0002	9.0299
0.005	668.05	217.56	3.0706	0.0003	9.0584
0.007	921.12	217.56	4.2339	0.0005	8.9214
0.009	1214.4	217.56	5.5819	0.0006	9.1481
0.01	1330.2	217.56	6.1142	0.0007	9.0184
0.03	4007.3	217.56	18.4193	0.0020	9.0561
0.05	6625.7	217.56	30.4546	0.0034	8.9841
0.07	9215.7	217.56	42.3593	0.0047	8.9257
0.09	11904	217.56	54.7159	0.0061	8.9673

5.4. Comparing the results from five numerical models with experimental data based on stress-strain curves

Based on the stress-strain curves and their slope (E_{ap}) in Figure 5-7, the calculated apparent young's modulus (E_{ap}) from ideal model (12.1GPa) is nearly 2 times larger than the experimental one (6.8GPa). Considering random joint position irregularity alone reduces the E_{ap} minimally to 12GPa with less than 1% reduction. When random E_{ap} for each strut is considered, there is no significant impact on E_{ap} except having few variations after stress value 40 MPa which results in having a minor reduction 6% in general slope of this curve. In contrast to the models with random joint position and random E_{ap}, considering random outer diameter for each strut lowers the E_{ap} drastically by 23% (9.2GPa) in comparison to the ideal model. In addition, when random outer diameter is combined with random joint position, there is a slight reduction in E_{ap} (3%) in comparison to considering random outer diameter alone. Therefore, random outer diameter has the greatest impact on E_{ap} among all the assumed irregularities.

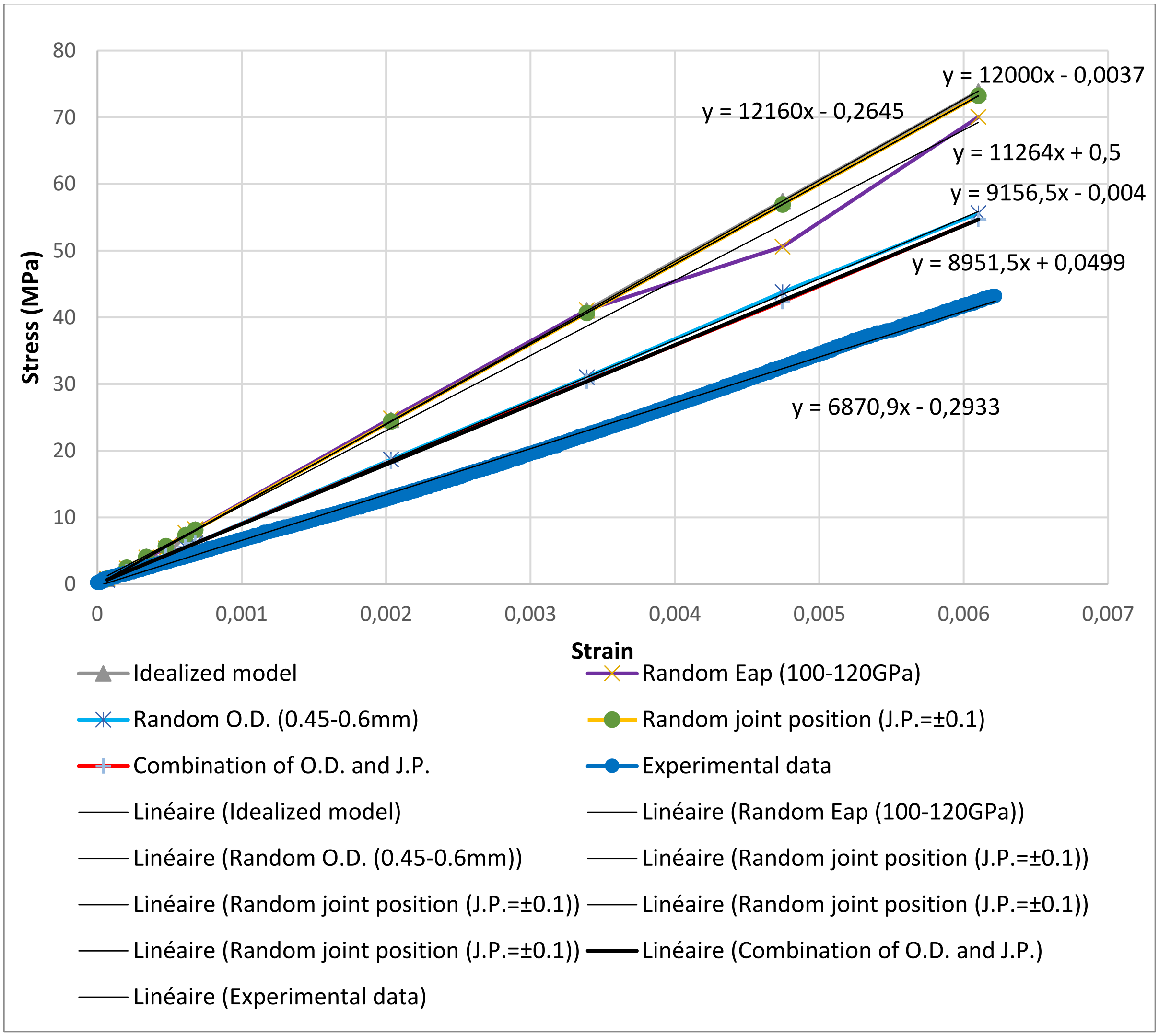

Figure 5-7 Stress-strain curves of numerical models vs. experiment

CONCLUSIONS

In this study, Ti-6Al-4V porous structures with cubic unit-cell topology were printed by AM using the SLM method. The mechanical properties and especially in-plane strain heterogeneities of these biomaterials were investigated. The following results can be drawn:

1. Apparent stress-strain curves from DIC method for three samples show highest E_{ap} value while shortest linear region length in comparison with those from extensometer and machine frame.
2. Interestingly, linear region length values from machine for three samples are so close to each other (i.e. 0.0079, 0.0066, and 0.0079 respectively); this is the same conclusion for other methods.
3. All three samples were fabricated by SLM method with the same process parameters, but nonetheless each sample has different E_{ap} value in loading mode for each method.
4. Strain maps and histograms of three faces for each sample indicate that strain value (mean), strain distribution value (StdDev), and even strain distribution pattern is not the same among all samples.
5. The most uniform strain distribution can be observed in sample 1. On the other hand, the strain is distributed still uniformly, but more heterogeneously in sample 2, and in sample 3, severe strain localisations happen in only few floors.
6. Regarding peak strain values, floors do not have the same order in three samples. However, floor 2 has the highest strain value among floors in three samples. In addition, it is found that macroscopic strain of peak strain point for each floor differs sample by sample (i.e. -0.016, -0.014, and -0.018 respectively).
7. Earlier deformation of one floor at first does not guarantee failure of that floor at the end since strain localization is a more crucial factor to be taken into consideration when analyzing deformation behavior of floors (e.g. floor 8 in sample 3).
8. Among all geometrical irregularities considered in the numerical model, random outer diameter has the greatest impact (23%) on the reduction of E_{ap} while random joint

position plays a minimal role in lowering E_{ap} and as a result having closer results to experimental data.

RECOMMENDATIONS

1. It would be a good idea to check the parallelism of the compressive surfaces of the specimens more accurately with the interferometer-assisted optical method instead of doing that manually.
2. It is advised to try other manufacturing irregularities with different ranges.
3. It is recommended to perform some fatigue tests on these structures to check how tolerable they are under real load condition like being applied in the body. In addition, by modeling the same structure and condition in APDL, it is possible to compare the results and make a conclusion.

APPENDIX 1

APDL code for creating the ideal 8*8*8 cubic porous structure

```
FINISH
/CLEAR

! parameters
eps=1e-3                        ! small number for selection
! geometry
ax=14.75 $ nx=8  $ dx=ax/nx   ! span and division along x axis
ay=14.75 $ ny=8  $ dy=ay/ny
az=14.75 $ nz=8  $ dz=az/nz
nn=(nx+1)*(ny+1)*(nz+1)       ! number of keypoints
dex=0.6                         ! beam outer diameter
wtx=dex/2                       ! beam wall thickness
dey=0.6
wty=dey/2
dez=0.6
wtz=dez/2

! material
mex=115E3                       ! beams parallel to x axis
nux=0.31
mey=115E3
nuy=0.31
mez=115E3
nuz=0.31
nex=2                           ! number of elements along x lines
ney=2
nez=2

! loads
dispy=0.1                       ! imposed displacement in y direction (mm)

! model
/PREP7

! element type, material and cross section
```

```
ET,1,PIPE288,,,,2                ! 3D 2-node pipe element
MP,EX,1,mex                      !Defines a linear material property
MP,NUXY,1,nux
SECTYPE, 1, PIPE                  ! Associates section type information with a section ID number
SECDATA, dex, wtx                 ! Describes the geometry of a section

ET,2,PIPE288,,,,2
MP,EX,2,mey
MP,NUXY,2,nuy
SECTYPE, 2, PIPE
SECDATA, dey, wty

ET,3,PIPE288,,,,2
MP,EX,3,mez
MP,NUXY,3,nuz
SECTYPE, 3, PIPE
SECDATA, dez, wtz

ET,4,SHELL181                      ! 4-Node Structural Shell
MP,EX,4,mep
MP,NUXY,4,nup
SECTYPE, 4, SHELL
SECDATA, pt, 4

 cc=0                              !counter starts from 0
! keypoints
*DO,k,1,nz+1
   *DO,j,1,ny+1
      *DO,i,1,nx+1
         cc=cc+1
         K,cc,dx*(i-1),dy*(j-1),dz*(k-1)
      *ENDDO
   *ENDDO
*ENDDO
KPLOT                              !Display keypoints from NP1 to NP2
/PNUM,KP,1                         !controls entity numbering/1=turn on numbers
/VIEW,1,1,1,1                      !defines the viewing direction for the display

! x lines
*DO,k,1,nz+1
   *DO,j,1,ny+1
      *DO,i,1,nx
         ni=i+(j-1)*(nx+1)+(k-1)*(nx+1)*(ny+1)
         nj=ni+1
         L,ni,nj
```

```
         LATT,   1,     ,   1,   ,   ,   ,   1       !Associates element attributes with the selected,
unmeshed lines
      *ENDDO
   *ENDDO
*ENDDO
LESIZE,ALL,,,nex                  !Specifies the divisions and spacing ratio on unmeshed lines
LPLOT

! y lines
LSEL,U,LINE,,ALL                  !Selects a subset of lines-unselects a set from the current set-
*DO,k,1,nz+1
   *DO,j,1,ny
      *DO,i,1,nx+1
         ni=i+(j-1)*(nx+1)+(k-1)*(nx+1)*(ny+1)
         nj=i+j*(nx+1)+(k-1)*(nx+1)*(ny+1)
         L,ni,nj
               LATT,   2,     ,   2,   ,   ,   ,    2
      *ENDDO
   *ENDDO
*ENDDO
LESIZE,ALL,,,ney

! z lines
LSEL,U,LINE,,ALL
*DO,k,1,nz
   *DO,j,1,ny+1
      *DO,i,1,nx+1
         ni=i+(j-1)*(nx+1)+(k-1)*(nx+1)*(ny+1)
         nj=i+(j-1)*(nx+1)+k*(nx+1)*(ny+1)
         L,ni,nj
         LATT,   3,     ,   3,   ,   ,   ,    3
      *ENDDO
   *ENDDO
*ENDDO
LESIZE,ALL,,,nez
ALLS

! meshing lines
LMESH,ALL

/ESHAPE,1
EPLOT
/VIEW,1,1,2,3
/REP
```

```
! BC, loads and solution
/SOLU

! BC
NSEL,S,LOC,Y,0
D,ALL,UY,0
NSEL,R,LOC,Z,0
D,ALL,UZ,0
NSEL,S,LOC,Y,0
NSEL,R,LOC,Z,0
NSEL,R,LOC,X,0
D,ALL,UX,0
press=0

! y displacement or pressure
NSEL,S,LOC,Y,ay
D,ALL,UY,-dispy

ALLS
EPLOT

! solution
ALLS
SOLVE

! results
/POST1
SET,LAST
PLNS,S,EQV

! compute applied force on top
NSEL,S,LOC,Y,ay
PRRS
```

APPENDIX ll

APDL code for creating 8*8*8 cubic porous structure with random outer diameter (0.45-0.6mm) for struts as a manufacturing geometrical irregularity

```
FINISH
/CLEAR

! parameters
eps=1e-3  ! small number for selection
! geometry
ax=14.75 $ nx=8  $ dx=ax/nx ! span and division along x axis
ay=14.75 $ ny=8  $ dy=ay/ny
az=14.75 $ nz=8  $ dz=az/nz
odb=0.45
odt=0.6
odx=rand(odb,odt)               ! beam outer diameter
wtx=odx/2                       ! beam wall thickness
ody=rand(odb,odt)
wty=ody/2
odz=rand(odb,odt)
wtz=odz/2
dex=1
! material
mex=115E3                        ! beams parallel to x axis
nux=0.31
mey=115E3
nuy=0.31
mez=115E3
nuz=0.31
! mesh
nex=2                           ! number of elements along x lines
ney=2
nez=2
!ae=4                           ! number of elements along area lines
! loads
dispy=-0.3                      ! imposed displacement in y direction (mm)
! model
/PREP7

! element type, material and cross section
```

```
ET,1,PIPE288,,,,2              ! 3D 2-node pipe element
MP,EX,1,mex                    !Defines a linear material property
MP,NUXY,1,nux

ET,2,PIPE288,,,,2
MP,EX,2,mey
MP,NUXY,2,nuy

ET,3,PIPE288,,,,2
MP,EX,3,mez
MP,NUXY,3,nuz

  cc=0                              !counter starts from 0
! keypoints
*DO,k,1,nz+1
   *DO,j,1,ny+1
      *DO,i,1,nx+1
         cc=cc+1
         K,cc,dx*(i-1),dy*(j-1),dz*(k-1)
      *ENDDO
   *ENDDO
*ENDDO
KPLOT
/PNUM,KP,1                          !controls entity numbering/1=turn on numbers
/VIEW,1,1,1,1             !defines the viewing direction for the display,number of window, , , ,
/REP

!/EOF

! x lines
countx=0
*DO,k,1,nz+1
   *DO,j,1,ny+1
      *DO,i,1,nx
         LSEL,U,LINE,,ALL
         odx=rand(odb,odt)
         wtx=odx/2
         ni=i+(j-1)*(nx+1)+(k-1)*(nx+1)*(ny+1)
         nj=ni+1
         L,ni,nj
         countx=countx+1
         SECTYPE,countx,PIPE
         SECDATA,odx,wtx
        LATT,   1,    ,  1,  ,  ,  ,  countx      !Associates element attributes with the selected,
unmeshed lines
```

```
      *ENDDO
   *ENDDO
*ENDDO
LESIZE,ALL,,,nex     !Specifies the divisions and spacing ratio on unmeshed lines.
LPLOT

!*IF,0,GT,1,THEN
! y lines
county=countx+0
*DO,k,1,nz+1
   *DO,j,1,ny
      *DO,i,1,nx+1
         LSEL,U,LINE,,ALL
         ni=i+(j-1)*(nx+1)+(k-1)*(nx+1)*(ny+1)
         nj=i+j*(nx+1)+(k-1)*(nx+1)*(ny+1)
         L,ni,nj
         ody=rand(odb,odt)
         wty=ody/2
         county=county+1
         SECTYPE,county,PIPE
         SECDATA,ody,wty
               LATT,   2,     ,    2,   ,   ,   ,      county
      *ENDDO
   *ENDDO
*ENDDO
LESIZE,ALL,,,ney

!/EOF

! z lines
countz=countx+county+0
*DO,k,1,nz
   *DO,j,1,ny+1
      *DO,i,1,nx+1
         LSEL,U,LINE,,ALL
         ni=i+(j-1)*(nx+1)+(k-1)*(nx+1)*(ny+1)
         nj=i+(j-1)*(nx+1)+k*(nx+1)*(ny+1)
         L,ni,nj
         odz=rand(odb,odt)
         wtz=odz/2
         countz=countz+1
         SECTYPE,countz,PIPE
         SECDATA,odz,wtz
         LATT,   3,     ,    3,   ,   ,   ,      countz
      *ENDDO
```

```
  *ENDDO
*ENDDO
LESIZE,ALL,,,nez
LPLOT
!/EOF

! meshing lines
ALLS
LMESH,ALL

EPLOT
/ESHAPE,1
/PNUM,SEC,1
/NUM,1
/REP

!/EOF

! BC, loads and solution
/SOLU
NSEL,S,LOC,Y,0
D,ALL,UY,0
NSEL,R,LOC,Z,0
D,ALL,UZ,0
NSEL,S,LOC,Y,0
NSEL,R,LOC,Z,0
NSEL,R,LOC,X,0
D,ALL,UX,0

! y displacement or pressure
NSEL,S,LOC,Y,ay
D,ALL,UY,dispy

ALLS
/PBC,U,,1
/PSF,PRES,NORM,2
EPLOT
!/EOF
! solution
ALLS
SOLVE

! results
/POST1
SET,LAST
```

```
PLNS,S,EQV

! compute applied force on top
NSEL,S,LOC,Y,ay
PRRS
```

APPENDIX lll

APDL code for creating 8*8*8 cubic porous structure with random joint position as a manufacturing geometrical irregularity

```
FINISH
/CLEAR

! parameters
eps=1e-3                          ! small number for selection
! geometry
ax=14.75 $ nx=8   $ dx=ax/nx ! span and division along x axis
ay=14.75 $ ny=8  $ dy=ay/ny
az=14.75 $ nz=8  $ dz=az/nz
odx=0.6                           ! beam outer diameter
wtx=odx/2                         ! beam wall thickness
ody=0.6
wty=ody/2
odz=0.6
wtz=odz/2

! material
mex=115E3                          ! beams parallel to x axis
nux=0.31
mey=115E3
nuy=0.31
mez=115E3
nuz=0.31
! mesh
nex=2                               ! number of elements along x lines
ney=2
nez=2
! loads
dispy=-0.3                         ! imposed displacement in y direction (mm)
! model
/PREP7

! element type, material and cross section
ET,1,PIPE288,,,,2                ! 3D 2-node pipe element
MP,EX,1,mex                       !Defines a linear material property
MP,NUXY,1,nux
```

```
SECTYPE, 1, PIPE              ! Associates section type information with a section ID number
SECDATA, odx, wtx            ! Describes the geometry of a section------

ET,2,PIPE288,,,,2
MP,EX,2,mey
MP,NUXY,2,nuy
SECTYPE, 2, PIPE
SECDATA, ody, wty

ET,3,PIPE288,,,,2
MP,EX,3,mez
MP,NUXY,3,nuz
SECTYPE, 3, PIPE
SECDATA, odz, wtz

cc=0                          !counter starts from 0
! keypoints
*DO,k,1,nz+1
  *DO,j,1,ny+1
    *DO,i,1,nx+1
      KSEL,S,KP,,ALL
       epsb=-0.3                !random position for each keypoint in each direction
       epst=0.3
      *IF,j,EQ,ny+1,THEN
        dxx=0
        dyy=0
        dzz=0
      *ELSEIF,j,EQ,1,THEN
        dxx=0
        dyy=0
        dzz=0
      *ELSE
        dxx=rand(epsb,epst)
        dyy=rand(epsb,epst)
        dzz=rand(epsb,epst)
      *ENDIF
      cc=cc+1
      K,cc,dx*(i-1)+dxx,dy*(j-1)+dyy,dz*(k-1)+dzz
    *ENDDO
  *ENDDO
*ENDDO
KPLOT                         !Display keypoints from NP1 to NP2
/PNUM,KP,1                    !controls entity numbering/1=turn on numbers
/VIEW,1,1,1,1                 !defines the viewing direction for the display,number of window, , , ,
/REP
```

```
! x lines
*DO,k,1,nz+1
   *DO,j,1,ny+1
      *DO,i,1,nx
         ni=i+(j-1)*(nx+1)+(k-1)*(nx+1)*(ny+1)
         nj=ni+1
         L,ni,nj
        LATT,  1,    ,  1,  ,  ,  ,  1    !Associates element attributes with the selected, unmeshed
lines
      *ENDDO
   *ENDDO
*ENDDO
LESIZE,ALL,,,nex                    !Specifies the divisions and spacing ratio on unmeshed lines.
LPLOT

!/EOF

! y lines
*DO,k,1,nz+1
   *DO,j,1,ny
      *DO,i,1,nx+1
         ni=i+(j-1)*(nx+1)+(k-1)*(nx+1)*(ny+1)
         nj=i+j*(nx+1)+(k-1)*(nx+1)*(ny+1)
         L,ni,nj
               LATT,  2,    ,  2,  ,  ,  ,    2
      *ENDDO
   *ENDDO
*ENDDO
LESIZE,ALL,,,ney

!/EOF

! z lines
!LSEL,U,LINE,,ALL
*DO,k,1,nz
   *DO,j,1,ny+1
      *DO,i,1,nx+1
         ni=i+(j-1)*(nx+1)+(k-1)*(nx+1)*(ny+1)
         nj=i+(j-1)*(nx+1)+k*(nx+1)*(ny+1)
         L,ni,nj
         LATT,  3,    ,  3,  ,  ,  ,    3
      *ENDDO
   *ENDDO
*ENDDO
LESIZE,ALL,,,nez
```

```
!ALLS
LPLOT
/PNUM,KP,0
/REP
!/EOF

! meshing lines
ALLS
LMESH,ALL

EPLOT
/ESHAPE,1
/PNUM,SEC,1
/NUM,1
/REP

!/EOF

! BC, loads and solution
/SOLU
NSEL,S,LOC,Y,0
D,ALL,UY,0
NSEL,R,LOC,Z,0
D,ALL,UZ,0
NSEL,S,LOC,Y,0
NSEL,R,LOC,Z,0
NSEL,R,LOC,X,0
D,ALL,UX,0

! y displacement or pressure
NSEL,S,LOC,Y,ay
  D,ALL,UY,dispy
!/EOF

ALLS
/PBC,U,,1
/PSF,PRES,NORM,2
EPLOT
! solution
ALLS
SOLVE

! results
/POST1
SET,LAST
```

```
PLNS,S,EQV

! compute applied force on top
NSEL,S,LOC,Y,ay
PRRS
```

APPENDIX lV

APDL code for creating 8*8*8 cubic porous structure with random distribution of young's modulus for each strut

```
FINISH
/CLEAR

! parameters
eps=1e-3  ! small number for selection
! geometry
ax=14.75 $ nx=8  $ dx=ax/nx ! span and division along x axis
ay=14.75 $ ny=8  $ dy=ay/ny
az=14.75 $ nz=8  $ dz=az/nz
dex=0.6                  ! beam outer diameter
wtx=dex/2                 ! beam wall thickness
dey=0.6
wty=dey/2
dez=0.6
wtz=dez/2
! material
me1=100E3
me2=120E3
mex=rand(me1,me2)       ! beams parallel to x axis
nux=0.31
mey=rand(me1,me2)
nuy=0.31
mez=rand(me1,me2)
nuz=0.31
```

```
! mesh
nex=2                  ! number of elements along x lines
ney=2
nez=2
! loads
dispy=0.1              ! imposed displacement in y direction (mm)
! model
/PREP7

! element type, material and cross section
ET,1,PIPE288,,,,2                          ! 3D 2-node pipe element
MP,EX,1,mex                                !Defines a linear material property
MP,NUXY,1,nux
SECTYPE, 1, PIPE          ! Associates section type information with a section ID number
SECDATA, dex, wtx         ! Describes the geometry of a section
ET,2,PIPE288,,,,2
MP,EX,2,mey
MP,NUXY,2,nuy
SECTYPE, 2, PIPE
SECDATA, dey, wty
ET,3,PIPE288,,,,2
MP,EX,3,mez
MP,NUXY,3,nuz
SECTYPE, 3, PIPE
SECDATA, dez, wtz
 cc=0                     !counter starts from 0
! keypoints
*DO,k,1,nz+1
   *DO,j,1,ny+1
      *DO,i,1,nx+1
```

```
      cc=cc+1
      K,cc,dx*(i-1),dy*(j-1),dz*(k-1)
    *ENDDO
  *ENDDO
*ENDDO
KPLOT           !Display keypoints from NP1 to NP2
/PNUM,KP,1      !controls entity numbering/1=turn on numbers
/VIEW,1,1,1,1   !defines the viewing direction for the display,number of window, , , ,
/REP
! x lines
*DO,k,1,nz+1
  *DO,j,1,ny+1
    *DO,i,1,nx
      ni=i+(j-1)*(nx+1)+(k-1)*(nx+1)*(ny+1)
      nj=ni+1
      L,ni,nj
      LATT, 1, , 1, , , , 1     !Associates element attributes with the selected,
unmeshed lines
    *ENDDO
  *ENDDO
*ENDDO
LESIZE,ALL,,,nex    !Specifies the divisions and spacing ratio on unmeshed lines.
LPLOT
! y lines
!LSEL,U,LINE,,ALL       !Selects a subset of lines-unselects a set from the current set-
*DO,k,1,nz+1
  *DO,j,1,ny
    *DO,i,1,nx+1
      ni=i+(j-1)*(nx+1)+(k-1)*(nx+1)*(ny+1)
      nj=i+j*(nx+1)+(k-1)*(nx+1)*(ny+1)
```

```
        L,ni,nj
            LATT,   2,     ,    2,   ,   ,   ,      2
      *ENDDO
   *ENDDO
*ENDDO
LESIZE,ALL,,,ney
! z lines
!LSEL,U,LINE,,ALL
*DO,k,1,nz
   *DO,j,1,ny+1
      *DO,i,1,nx+1
        ni=i+(j-1)*(nx+1)+(k-1)*(nx+1)*(ny+1)
        nj=i+(j-1)*(nx+1)+k*(nx+1)*(ny+1)
        L,ni,nj
        LATT,   3,     ,    3,   ,   ,   ,      3
      *ENDDO
   *ENDDO
*ENDDO
LESIZE,ALL,,,nez
! meshing lines
LMESH,ALL
! meshing areas
/ESHAPE,1
EPLOT
/VIEW,1,1,2,3
/REP
! BC, loads and solution
/SOLU
NSEL,S,LOC,Y,0
D,ALL,UY,0
```

```
NSEL,R,LOC,Z,0
D,ALL,UZ,0
NSEL,S,LOC,Y,0
NSEL,R,LOC,Z,0
NSEL,R,LOC,X,0
D,ALL,UX,0

! y displacement or pressure
NSEL,S,LOC,Y,ay
D,ALL,UY,-dispy

ALLS
/PBC,U,,1
/PSF,PRES,NORM,2
EPLOT

! solution
ALLS
SOLVE

! results
/POST1
SET,LAST
PLNS,S,EQV

! compute applied force on top
NSEL,S,LOC,Y,ay
PRRS
```

APPENDIX V

APDL code for creating 8*8*8 cubic porous structure with combination of random outer diameter and random joint position

```
FINISH
/CLEAR
!/UIS,MSGPOP,3

! parameters
eps=1e-3  ! small number for selection
! geometry
ax=14.75 $ nx=8   $ dx=ax/nx ! span and division along x axis
ay=14.75 $ ny=8  $ dy=ay/ny
az=14.75 $ nz=8  $ dz=az/nz
odb=0.45
odt=0.65
odx=rand(odb,odt)                ! beam outer diameter
wtx=odx/2                        ! beam wall thickness
ody=rand(odb,odt)
wty=ody/2
odz=rand(odb,odt)
wtz=odz/2

! material
mex=115E3                        ! beams parallel to x axis
nux=0.31
mey=115E3
nuy=0.31
mez=115E3
nuz=0.31

! mesh
nex=2                 ! number of elements along x lines
ney=2
nez=2
```

```
! loads
dispy=-0.3            ! imposed displacement in y direction (mm)
! model
/PREP7

                                          ! element type, material and cross section
ET,1,PIPE288,,,,2                         ! 3D 2-node pipe element
MP,EX,1,mex                               !Defines a linear material property
MP,NUXY,1,nux

ET,2,PIPE288,,,,2
MP,EX,2,mey
MP,NUXY,2,nuy

ET,3,PIPE288,,,,2
MP,EX,3,mez
MP,NUXY,3,nuz

  cc=0                    !counter starts from 0
! keypoints
*DO,k,1,nz+1
   *DO,j,1,ny+1
      *DO,i,1,nx+1
         KSEL,S,KP,,ALL
         epsb=-0.1            !random position for each keypoint in each direction
         epst=0.1
         *IF,j,EQ,ny+1,THEN
           dxx=0
           dyy=0
           dzz=0
         *ELSEIF,j,EQ,1,THEN
           dxx=0
           dyy=0
           dzz=0
         *ELSE
           dxx=rand(epsb,epst)
           dyy=rand(epsb,epst)
           dzz=rand(epsb,epst)
         *ENDIF
         cc=cc+1
         K,cc,dx*(i-1)+dxx,dy*(j-1)+dyy,dz*(k-1)+dzz
      *ENDDO
   *ENDDO
*ENDDO
KPLOT       !Display keypoints from NP1 to NP2
```

```
/PNUM,KP,1      !controls entity numbering/1=turn on numbers
/VIEW,1,1,1,1    !defines the viewing direction for the display,number of window, , , ,
/REP

!/EOF
countx=0
! x lines
*DO,k,1,nz+1
   *DO,j,1,ny+1
      *DO,i,1,nx
         LSEL,U,LINE,,ALL
         odx=rand(odb,odt)
         wtx=odx/2
         ni=i+(j-1)*(nx+1)+(k-1)*(nx+1)*(ny+1)
         nj=ni+1
         L,ni,nj
         countx=countx+1
         SECTYPE,countx,PIPE
         SECDATA,odx,wtx
        LATT,   1,     ,   1,   ,   ,   ,  countx      !Associates element attributes with the selected,
unmeshed lines
      *ENDDO
   *ENDDO
*ENDDO
LESIZE,ALL,,,nex     !Specifies the divisions and spacing ratio on unmeshed lines.
LPLOT



! y lines
county=countx+0
!LSEL,U,LINE,,ALL        !Selects a subset of lines-unselects a set from the current set-
*DO,k,1,nz+1
   *DO,j,1,ny
      *DO,i,1,nx+1
         LSEL,U,LINE,,ALL
         ni=i+(j-1)*(nx+1)+(k-1)*(nx+1)*(ny+1)
         nj=i+j*(nx+1)+(k-1)*(nx+1)*(ny+1)
         L,ni,nj
         ody=rand(odb,odt)
         wty=ody/2
         county=county+1
         SECTYPE,county,PIPE
         SECDATA,ody,wty
               LATT,   2,     ,    2,   ,   ,   ,    county
```

```
      *ENDDO
   *ENDDO
*ENDDO
LESIZE,ALL,,,ney

!/EOF

! z lines
countz=countx+county+0
!LSEL,U,LINE,,ALL
*DO,k,1,nz
   *DO,j,1,ny+1
      *DO,i,1,nx+1
         LSEL,U,LINE,,ALL
         ni=i+(j-1)*(nx+1)+(k-1)*(nx+1)*(ny+1)
         nj=i+(j-1)*(nx+1)+k*(nx+1)*(ny+1)
         L,ni,nj
         odz=rand(odb,odt)
         wtz=odz/2
         countz=countz+1
         SECTYPE,countz,PIPE
         SECDATA,odz,wtz
         LATT,   3,     ,    3,   ,   ,   ,    countz
      *ENDDO
   *ENDDO
*ENDDO
LESIZE,ALL,,,nez
LPLOT
/PNUM,KP,0
/REP

!/EOF

! meshing lines
ALLS
LMESH,ALL

EPLOT
/ESHAPE,1
/PNUM,SEC,1
/NUM,1
/REP

!/EOF
```

```
! BC, loads and solution
/SOLU
NSEL,S,LOC,Y,0
D,ALL,UY,0
NSEL,R,LOC,Z,0
D,ALL,UZ,0
NSEL,S,LOC,Y,0
NSEL,R,LOC,Z,0
NSEL,R,LOC,X,0
D,ALL,UX,0

! y displacement or pressure
NSEL,S,LOC,Y,ay
  D,ALL,UY,dispy

ALLS
/PBC,U,,1
/PSF,PRES,NORM,2
EPLOT

! solution
ALLS
SOLVE

! results
/POST1
SET,LAST
PLNS,S,EQV

! compute applied force on top
NSEL,S,LOC,Y,ay
PRRS
```

LIST OF REFERENCES

Abueidda, Diab W, Mohamed Elhebeary, Cheng-Shen Andrew Shiang, Siyuan Pang, Rashid K Abu Al-Rub, and Iwona M Jasiuk. 2019. 'Mechanical properties of 3D printed polymeric Gyroid cellular structures: Experimental and finite element study', *Materials & Design*, 165: 107597.

Ahmadi, S. M., G. Campoli, S. Amin Yavari, B. Sajadi, R. Wauthle, J. Schrooten, H. Weinans, and A. A. Zadpoor. 2014a. 'Mechanical behavior of regular open-cell porous biomaterials made of diamond lattice unit cells', *Journal of the mechanical behavior of biomedical materials*, 34: 106-15.

———. 2014b. 'Mechanical behavior of regular open-cell porous biomaterials made of diamond lattice unit cells', *J Mech Behav Biomed Mater*, 34: 106-15.

Al-Ketan, Oraib, Reza Rowshan, and Rashid K Abu Al-Rub. 2018. 'Topology-mechanical property relationship of 3D printed strut, skeletal, and sheet based periodic metallic cellular materials', *Additive Manufacturing*, 19: 167-83.

Alexander, Amy E., Nicole Wake, Leonid Chepelev, Philipp Brantner, Justin Ryan, and Kenneth C. Wang. 2021. 'A guideline for 3D printing terminology in biomedical research utilizing ISO/ASTM standards', *3D Printing in Medicine*, 7: 8.

Ali, Davar, and Sadri Sen. 2017. 'Finite element analysis of mechanical behavior, permeability and fluid induced wall shear stress of high porosity scaffolds with gyroid and lattice-based architectures', *Journal of the mechanical behavior of biomedical materials*, 75: 262-70.

Arabnejad, Sajad, R. Burnett Johnston, Jenny Ann Pura, Baljinder Singh, Michael Tanzer, and Damiano Pasini. 2016. 'High-strength porous biomaterials for bone replacement: A strategy to assess the interplay between cell morphology, mechanical properties, bone ingrowth and manufacturing constraints', *Acta Biomaterialia*, 30: 345-56.

Ataee, Arash, Yuncang Li, Darren Fraser, Guangsheng Song, and Cuie Wen. 2018. 'Anisotropic Ti-6Al-4V gyroid scaffolds manufactured by electron beam melting (EBM) for bone implant applications', *Materials & Design*, 137: 345-54.

Attar, Hooyar, L Löber, A Funk, M Calin, LC Zhang, KG Prashanth, S Scudino, YS Zhang, and J Eckert. 2015. 'Mechanical behavior of porous commercially pure Ti and Ti–TiB composite materials manufactured by selective laser melting', *Materials Science and Engineering: A*, 625: 350-56.

Balachandramurthi, Arun Ramanathan, Johan Moverare, Nikhil Dixit, and Robert Pederson. 2018. 'Influence of defects and as-built surface roughness on fatigue properties of additively manufactured Alloy 718', *Materials Science and Engineering: A*, 735: 463-74.

Bayley, Christopher, and Michael Kopac. 2018. 'The Implications of Additive Manufacturing on Canadian Armed Forces Operational Functions'.

Bourell, David L. 2016. 'Perspectives on additive manufacturing', *Annual Review of Materials Research*, 46: 1-18.

Buj-Corral, Irene, Aitor Tejo-Otero, and Felip Fenollosa-Artés. 2020. 'Development of am technologies for metals in the sector of medical implants', *Metals*, 10: 686.

Campoli, Gianni, MS Borleffs, S Amin Yavari, R Wauthle, Harrie Weinans, and Amir Abbas Zadpoor. 2013. 'Mechanical properties of open-cell metallic biomaterials manufactured using additive manufacturing', *Materials & Design*, 49: 957-65.

Cao, Xiaofei, Shengyu Duan, Jun Liang, Weibin Wen, and Daining Fang. 2018. 'Mechanical properties of an improved 3D-printed rhombic dodecahedron stainless steel lattice structure of variable cross section', *International Journal of Mechanical Sciences*, 145: 53-63.

Chen, Qizhi, and George A. Thouas. 2015. 'Metallic implant biomaterials', *Materials Science and Engineering: R: Reports*, 87: 1-57.

Chen, Wen-Ming, Yi Min Xie, Gabriele Imbalzano, Jianhu Shen, Shanqing Xu, Sung-Jae Lee, and Peter Vee Sin Lee. 2016. 'Lattice Ti structures with low rigidity but compatible mechanical strength: Design of implant materials for trabecular bone', *International Journal of Precision Engineering and Manufacturing*, 17: 793-99.

Chen, Zhiwen, Guoliang Xu, Qiang Cao, Meng Ruan, Sheng Liu, Huiming Pan, and Li Liu. 2022. 'Deformation measurement in Al thin films at elevated temperatures by digital image correlation with speckles prepared by femtosecond laser', *Optics & Laser Technology*, 155: 108339.

Choy, Sing Ying, Chen-Nan Sun, Kah Fai Leong, and Jun Wei. 2017. 'Compressive properties of functionally graded lattice structures manufactured by selective laser melting', *Materials & Design*, 131: 112-20.

Cuadrado, A., A. Yánez, O. Martel, S. Deviaene, and D. Monopoli. 2017. 'Influence of load orientation and of types of loads on the mechanical properties of porous Ti6Al4V biomaterials', *Materials & Design*, 135: 309-18.

Dallago, M., V. Fontanari, E. Torresani, M. Leoni, C. Pederzolli, C. Potrich, and M. Benedetti. 2018. 'Fatigue and biological properties of Ti-6Al-4V ELI cellular structures with variously arranged cubic cells made by selective laser melting', *Journal of the mechanical behavior of biomedical materials*, 78: 381-94.

Dong, Guoying, and Yaoyao Fiona Zhao. 2018. 'Numerical and experimental investigation of the joint stiffness in lattice structures fabricated by additive manufacturing', *International Journal of Mechanical Sciences*, 148: 475-85.

Esfahani, Sajedeh Nasr, Mohsen Taheri Andani, Narges Shayesteh Moghaddam, Reza Mirzaeifar, and Mohammad Elahinia. 2016. 'Independent tuning of stiffness and toughness of additively manufactured titanium-polymer composites: Simulation, fabrication, and experimental studies', *Journal of Materials Processing Technology*, 238: 22-29.

Feng, Qixiang, Qian Tang, Ying Liu, Rossi Setchi, Shwe Soe, Shuai Ma, and Long Bai. 2018. 'Quasi-static analysis of mechanical properties of Ti6Al4V lattice structures manufactured using selective laser melting', *The International Journal of Advanced Manufacturing Technology*, 94: 2301-13.

Fukuda, A, M Takemoto, T Saito, S Fujibayashi, M Neo, Deepak K Pattanayak, T Matsushita, K Sasaki, N Nishida, and T Kokubo. 2011. 'Osteoinduction of porous Ti implants with a channel structure fabricated by selective laser melting', *Acta Biomaterialia*, 7: 2327-36.

Geetha, M., A. K. Singh, R. Asokamani, and A. K. Gogia. 2009. 'Ti based biomaterials, the ultimate choice for orthopaedic implants – A review', *Progress in Materials Science*, 54: 397-425.

Gibson, Lorna J, and Michael F Ashby. 1999. *Cellular solids: structure and properties* (Cambridge university press).

Gong, Haijun, Khalid Rafi, Hengfeng Gu, GD Janaki Ram, Thomas Starr, and Brent Stucker. 2015. 'Influence of defects on mechanical properties of Ti–6Al–4 V components produced by selective laser melting and electron beam melting', *Materials & Design*, 86: 545-54.

Gong, He, Wei Wu, Juan Fang, Xin Dong, Meisheng Zhao, and Tongtong Guo. 2012. 'Effects of Materials of Cementless Femoral Stem on the Functional Adaptation of Bone', *Journal of Bionic Engineering*, 9: 66-74.

Gong, X. H., Z. D. Feng, D. Fan, L. Lu, and S. N. Luo. 2022. 'Strain localization in titanium investigated via in situ digital image correlation with multiscale speckles', *Materials Characterization*, 189: 111940.

Gonzalez, Fernando J Quevedo, and Natalia Nuno. 2016. 'Finite element modeling of manufacturing irregularities of porous materials', *Biomaterials and Biomechanics in Bioengineering*, 3: 1-14.

Han, Changjun, Yan Li, Qian Wang, Shifeng Wen, Qingsong Wei, Chunze Yan, Liang Hao, Jie Liu, and Yusheng Shi. 2018. 'Continuous functionally graded porous titanium scaffolds manufactured by selective laser melting for bone implants', *Journal of the mechanical behavior of biomedical materials*, 80: 119-27.

Hedayati, R, H Hosseini-Toudeshky, M Sadighi, M Mohammadi-Aghdam, and AA Zadpoor. 2016. 'Computational prediction of the fatigue behavior of additively manufactured porous metallic biomaterials', *International Journal of Fatigue*, 84: 67-79.

Impens, Saartje, Yantian Chen, Steven Mullens, Frank Luyten, and Jan Schrooten. 2010. 'Controlled cell-seeding methodologies: a first step toward clinically relevant bone tissue engineering strategies', *Tissue Engineering Part C: Methods*, 16: 1575-83.

Jamshidinia, M., L. Wang, W. Tong, and R. Kovacevic. 2014. 'The bio-compatible dental implant designed by using non-stochastic porosity produced by Electron Beam Melting® (EBM)', *Journal of Materials Processing Technology*, 214: 1728-39.

Jardini, André Luiz, Maria Aparecida Larosa, Cecília Amélia de Carvalho Zavaglia, Luis Fernando Bernardes, Carlos Salles Lambert, Paulo Kharmandayan, Davi Calderoni, and Rubens Maciel Filho. 2014. 'Customised titanium implant fabricated in additive manufacturing for craniomaxillofacial surgery: This paper discusses the design and fabrication of a metallic implant for the reconstruction of a large cranial defect', *Virtual and physical prototyping*, 9: 115-25.

Juarez, Gregorio Arcos. 2017. 'Manufactura aditiva para prototipado rápido'.

Kadkhodapour, J., H. Montazerian, A. Ch Darabi, A. P. Anaraki, S. M. Ahmadi, A. A. Zadpoor, and S. Schmauder. 2015. 'Failure mechanisms of additively manufactured porous biomaterials: Effects of porosity and type of unit cell', *Journal of the mechanical behavior of biomedical materials*, 50: 180-91.

Karageorgiou, Vassilis, and David Kaplan. 2005. 'Porosity of 3D biomaterial scaffolds and osteogenesis', *Biomaterials*, 26: 5474-91.

Khan, Sabah. 2015. 'Analysis of tribological applications of functionally graded materials in mobility engineering', *Int. J. Sci. Eng. Res*, 6: 1150-60.

Klahn, Christoph, Bastian Leutenecker, and Mirko Meboldt. 2015. 'Design strategies for the process of additive manufacturing', *Procedia CIRP*, 36: 230-35.

Köhnen, Patrick, Christian Haase, Jan Bültmann, Stephan Ziegler, Johannes Henrich Schleifenbaum, and Wolfgang Bleck. 2018. 'Mechanical properties and deformation behavior of additively manufactured lattice structures of stainless steel', *Materials & Design*, 145: 205-17.

Kumar, A, KC Nune, LE Murr, and RDK Misra. 2016. 'Biocompatibility and mechanical behaviour of three-dimensional scaffolds for biomedical devices: process–structure–property paradigm', *International Materials Reviews*, 61: 20-45.

Labeas, GN, and MM Sunaric. 2010. 'Investigation on the static response and failure process of metallic open lattice cellular structures', *Strain*, 46: 195-204.

Lafarga, Xavier Aguilo, Pedro Gálvez Hernández, Nicolas Vanderesse, Fernando Quevedo González, Philippe Bocher, and Natalia Nuño. 2017. 'Effect of the building orientation on mechanical properties of porous structures made by additive manufacturing'.

Lautenschlager, Eugene P, and Peter Monaghan. 1993. 'Titanium and titanium alloys as dental materials', *International dental journal*, 43: 245-53.

Li, Fuping, Jinshan Li, Tingting Huang, Hongchao Kou, and Lian Zhou. 2017. 'Compression fatigue behavior and failure mechanism of porous titanium for biomedical applications', *Journal of the mechanical behavior of biomedical materials*, 65: 814-23.

Li, S. J., Q. S. Xu, Z. Wang, W. T. Hou, Y. L. Hao, R. Yang, and L. E. Murr. 2014. 'Influence of cell shape on mechanical properties of Ti–6Al–4V meshes fabricated by electron beam melting method', *Acta Biomaterialia*, 10: 4537-47.

Li, Yuncang, Jianyu Xiong, Peter D Hodgson, and Cui'e Wen. 2010. 'Effects of structural property and surface modification of Ti6Ta4Sn scaffolds on the response of SaOS2 cells for bone tissue engineering', *Journal of alloys and compounds*, 494: 323-29.

Liu, J. H., N. Vanderesse, J. C. Stinville, T. M. Pollock, P. Bocher, and D. Texier. 2019. 'In-plane and out-of-plane deformation at the sub-grain scale in polycrystalline materials assessed by confocal microscopy', *Acta Materialia*, 169: 260-74.

Liu, YJ, HL Wang, SJ Li, SG Wang, WJ Wang, WT Hou, YL Hao, R Yang, and LC Zhang. 2017. 'Compressive and fatigue behavior of beta-type titanium porous structures fabricated by electron beam melting', *Acta Materialia*, 126: 58-66.

Luxner, Mathias H., Juergen Stampfl, and Heinz E. Pettermann. 2005. 'Finite element modeling concepts and linear analyses of 3D regular open cell structures', *Journal of Materials Science*, 40: 5859-66.

Ma, Shuai, Qian Tang, Qixiang Feng, Jun Song, Xiaoxiao Han, and Fuyu Guo. 2019. 'Mechanical behaviours and mass transport properties of bone-mimicking scaffolds consisted of gyroid structures manufactured using selective laser melting', *Journal of the mechanical behavior of biomedical materials*, 93: 158-69.

Mertens, Christian, Hubert Löwenheim, and Jürgen Hoffmann. 2013. 'Image data based reconstruction of the midface using a patient-specific implant in combination with a vascularized osteomyocutaneous scapular flap', *Journal of Cranio-Maxillofacial Surgery*, 41: 219-25.

Miyamoto, Yoshinari, WA Kaysser, BH Rabin, Akira Kawasaki, and Reneé G Ford. 2013. *Functionally graded materials: design, processing and applications* (Springer Science & Business Media).

Murr, Lawrence E., Sara M. Gaytan, Diana A. Ramirez, Edwin Martinez, Jennifer Hernandez, Krista N. Amato, Patrick W. Shindo, Francisco R. Medina, and Ryan B. Wicker. 2012. 'Metal Fabrication by Additive Manufacturing Using Laser and Electron Beam Melting Technologies', *Journal of Materials Science & Technology*, 28: 1-14.

Nguyen, Hung Dang, A. Pramanik, A. K. Basak, Y. Dong, C. Prakash, S. Debnath, S. Shankar, I. S. Jawahir, Saurav Dixit, and Dharam Buddhi. 2022. 'A critical review on additive manufacturing of Ti-6Al-4V alloy: microstructure and mechanical properties', *Journal of Materials Research and Technology*, 18: 4641-61.

Ozdemir, Zuhal, Everth Hernandez-Nava, Andrew Tyas, James A Warren, Stephen D Fay, Russell Goodall, Iain Todd, and Harm Askes. 2016. 'Energy absorption in lattice structures in dynamics: Experiments', *International Journal of Impact Engineering*, 89: 49-61.

Pan, Bing, Kemao Qian, Huimin Xie, and Anand Asundi. 2009a. 'Two-dimensional digital image correlation for in-plane displacement and strain measurement: a review', *Measurement science and technology*, 20: 062001.

———. 2009b. 'Two-dimensional digital image correlation for in-plane displacement and strain measurement: a review', *Measurement Science and Technology*, 20.

Parthasarathy, Jayanthi, Binil Starly, and Shivakumar Raman. 2011. 'A design for the additive manufacture of functionally graded porous structures with tailored mechanical properties for biomedical applications', *Journal of Manufacturing Processes*, 13: 160-70.

Parthasarathy, Jayanthi, Binil Starly, Shivakumar Raman, and Andy Christensen. 2010. 'Mechanical evaluation of porous titanium (Ti6Al4V) structures with electron beam melting (EBM)', *Journal of the Mechanical Behavior of Biomedical Materials*, 3: 249-59.

Pérez-Sánchez, A., A. Yánez, A. Cuadrado, O. Martel, and N. Nuño. 2018. 'Fatigue behaviour and equivalent diameter of single Ti-6Al-4V struts fabricated by Electron Bean Melting orientated to porous lattice structures', *Materials & Design*, 155: 106-15.

Poumarat, Georges, and Patrick Squire. 1993. 'Comparison of mechanical properties of human, bovine bone and a new processed bone xenograft', *Biomaterials*, 14: 337-40.

Quevedo Gonzalez, F. J., and N. Nuno. 2016. 'Finite element modelling approaches for well-ordered porous metallic materials for orthopaedic applications: cost effectiveness and geometrical considerations', *Comput Methods Biomech Biomed Engin*, 19: 845-54.

Quevedo González, Fernando José, and Natalia Nuño. 2016. 'Finite element modelling approaches for well-ordered porous metallic materials for orthopaedic applications: cost effectiveness and geometrical considerations', *Computer methods in biomechanics and biomedical engineering*, 19: 845-54.

Radlof, W., H. Panwitt, C. Benz, and M. Sander. 2022. 'Image-based and in-situ measurement techniques for the characterization of the damage behavior of additively manufactured lattice structures under fatigue loading', *Procedia Structural Integrity*, 38: 50-59.

Ryan, Garrett, Abhay Pandit, and Dimitrios Panagiotis Apatsidis. 2006. 'Fabrication methods of porous metals for use in orthopaedic applications', *Biomaterials*, 27: 2651-70.

Smith, M., Z. Guan, and W. J. Cantwell. 2013. 'Finite element modelling of the compressive response of lattice structures manufactured using the selective laser melting technique', *International Journal of Mechanical Sciences*, 67: 28-41.

Tan, XP, YJ Tan, CSL Chow, SB Tor, and WY Yeong. 2017. 'Metallic powder-bed based 3D printing of cellular scaffolds for orthopaedic implants: A state-of-the-art review on manufacturing, topological design, mechanical properties and biocompatibility', *Materials Science and Engineering: C*, 76: 1328-43.

Torres-Sanchez, Carmen, FRA Al Mushref, M Norrito, K Yendall, Yang Liu, and Paul P Conway. 2017. 'The effect of pore size and porosity on mechanical properties and biological response of porous titanium scaffolds', *Materials Science and Engineering: C*, 77: 219-28.

Ushijima, K, WJ Cantwell, RAW Mines, S Tsopanos, and M Smith. 2011. 'An investigation into the compressive properties of stainless steel micro-lattice structures', *Journal of Sandwich Structures & Materials*, 13: 303-29.

Vanderesse, N., P. Bocher, N. Nuno, A. Yanez, and L. A. Hof. 2022. 'On the characterization of roughness and geometrical irregularities of additively manufactured single titanium-alloy struts', *Additive Manufacturing*, 54.

Vanderesse, N., I. Ky, F. Quevedo González, N. Nuño, and P. Bocher. 2016. 'Image analysis characterization of periodic porous materials produced by additive manufacturing', *Materials & Design*, 92: 767-78.

Vanderesse, N., M. Lagacé, F. Bridier, and P. Bocher. 2013. 'An Open Source Software for the Measurement of Deformation Fields by Means of Digital Image Correlation', *Microscopy and Microanalysis*, 19: 820-21.

Vanderesse, N., A. Richter, N. Nuno, and P. Bocher. 2018. 'Measurement of deformation heterogeneities in additive manufactured lattice materials by Digital Image Correlation: Strain maps analysis and reliability assessment', *J Mech Behav Biomed Mater*, 86: 397-408.

Vanderesse, N., A. Richter, N. Nuño, and P. Bocher. 2018. 'Measurement of deformation heterogeneities in additive manufactured lattice materials by Digital Image Correlation: Strain maps analysis and reliability assessment', *Journal of the mechanical behavior of biomedical materials*, 86: 397-408.

Wang, Qian, Changjun Han, Tomasz Choma, Qingsong Wei, Chunze Yan, Bo Song, and Yusheng Shi. 2017. 'Effect of Nb content on microstructure, property and in vitro apatite-forming capability of Ti-Nb alloys fabricated via selective laser melting', *Materials & Design*, 126: 268-77.

Wang, Xiaojian, Shanqing Xu, Shiwei Zhou, Wei Xu, Martin Leary, Peter Choong, M. Qian, Milan Brandt, and Yi Min Xie. 2016. 'Topological design and additive manufacturing of porous metals for bone scaffolds and orthopaedic implants: A review', *Biomaterials*, 83: 127-41.

Wauthle, Ruben, Seyed Mohammad Ahmadi, Saber Amin Yavari, Michiel Mulier, Amir Abbas Zadpoor, Harrie Weinans, Jan Van Humbeeck, Jean-Pierre Kruth, and Jan Schrooten. 2015. 'Revival of pure titanium for dynamically loaded porous implants using additive manufacturing', *Materials Science and Engineering: C*, 54: 94-100.

Wauthle, Ruben, Johan van der Stok, Saber Amin Yavari, Jan Van Humbeeck, Jean-Pierre Kruth, Amir Abbas Zadpoor, Harrie Weinans, Michiel Mulier, and Jan Schrooten.

2015. 'Additively manufactured porous tantalum implants', *Acta Biomaterialia*, 14: 217-25.

Wauthle, Ruben, Bey Vrancken, Britt Beynaerts, Karl Jorissen, Jan Schrooten, Jean-Pierre Kruth, and Jan Van Humbeeck. 2015. 'Effects of build orientation and heat treatment on the microstructure and mechanical properties of selective laser melted Ti6Al4V lattice structures', *Additive Manufacturing*, 5: 77-84.

Wieding, Jan, Robert Souffrant, Wolfram Mittelmeier, and Rainer Bader. 2013. 'Finite element analysis on the biomechanical stability of open porous titanium scaffolds for large segmental bone defects under physiological load conditions', *Medical Engineering & Physics*, 35: 422-32.

Wohlers, Terry T. 2014. *Wohlers Report...: 3D Printing and Additive Manufacturing, State of the Industry, Annual Worldwide Progress Report* (Wohlers Associates Incorporated).

Wu, M. W., J. K. Chen, M. K. Tsai, P. Wang, T. L. Cheng, B. H. Lin, P. H. Chiang, and A. Dhinakar. 2022. 'Uniaxial Compression Properties and Compression Fatigue Performance of Selective Laser Melted Ti-6Al-4V Cellular Structure', *Metals and Materials International*, 28: 132-44.

Xiao, Lijun, and Weidong Song. 2018. 'Additively-manufactured functionally graded Ti-6Al-4V lattice structures with high strength under static and dynamic loading: Experiments', *International Journal of Impact Engineering*, 111: 255-72.

Xiao, Lijun, Weidong Song, Cheng Wang, Haiyan Liu, Huiping Tang, and Jianzhong Wang. 2015. 'Mechanical behavior of open-cell rhombic dodecahedron Ti–6Al–4V lattice structure', *Materials Science and Engineering: A*, 640: 375-84.

Yan, Chunze, Liang Hao, Ahmed Hussein, and David Raymont. 2012. 'Evaluations of cellular lattice structures manufactured using selective laser melting', *International Journal of Machine Tools and Manufacture*, 62: 32-38.

Yang, Lei, Raya Mertens, Massimiliano Ferrucci, Chunze Yan, Yusheng Shi, and Shoufeng Yang. 2019. 'Continuous graded Gyroid cellular structures fabricated by selective laser melting: Design, manufacturing and mechanical properties', *Materials & Design*, 162: 394-404.

Yuan, Li, Songlin Ding, and Cuie Wen. 2019. 'Additive manufacturing technology for porous metal implant applications and triple minimal surface structures: A review', *Bioactive Materials*, 4: 56-70.

Zargarian, A., M. Esfahanian, J. Kadkhodapour, and S. Ziaei-Rad. 2016. 'Numerical simulation of the fatigue behavior of additive manufactured titanium porous lattice structures', *Materials Science and Engineering: C*, 60: 339-47.

Zhao, D., Y. Huang, Y. Ao, C. Han, Q. Wang, Y. Li, J. Liu, Q. Wei, and Z. Zhang. 2018a. 'Effect of pore geometry on the fatigue properties and cell affinity of porous titanium scaffolds fabricated by selective laser melting', *J Mech Behav Biomed Mater*, 88: 478-87.

Zhao, Danlei, Yutian Huang, Yong Ao, Changjun Han, Qian Wang, Yan Li, Jie Liu, Qingsong Wei, and Zhen Zhang. 2018b. 'Effect of pore geometry on the fatigue properties and cell affinity of porous titanium scaffolds fabricated by selective laser melting', *Journal of the mechanical behavior of biomedical materials*, 88: 478-87.

Zhao, Li, Xuan Pei, Lihua Jiang, Cheng Hu, Jianxun Sun, Fei Xing, Changchun Zhou, Yujiang Fan, and Xingdong Zhang. 2019. 'Bionic design and 3D printing of porous titanium alloy scaffolds for bone tissue repair', *Composites Part B: Engineering*, 162: 154-61.
Zhao, Xiaoli, Shujun Li, Man Zhang, Yandong Liu, Timothy B Sercombe, Shaogang Wang, Yulin Hao, Rui Yang, and Lawrence E Murr. 2016. 'Comparison of the microstructures and mechanical properties of Ti–6Al–4V fabricated by selective laser melting and electron beam melting', *Materials & Design*, 95: 21-31.